NEAR-INFRARED SPECTROSCOPY OF HIGH REDSHIFT QUASARS:

BRINGING DISTANT QUASARS INTO VIEW

Cooper Wilhelm Dix

Dissertation Prepared for the Degree of

DOCTOR OF PHILOSOPHY

UNIVERSITY OF NORTH TEXAS

May 2023

APPROVED:

Ohad Shemmer, Major Professor
Yuan Li, Committee Member
Chris L. Littler, Committee Member
Duncan Weathers, Committee Member
Jingbiao Cui, Chair of the Department of Physics
John Quintanilla, Dean of the College of Science
Victor Prybutok, Dean of the Toulouse Graduate School

Dix, Cooper Wilhelm. *Near-Infrared Spectroscopy of High Redshift Quasars: Bringing Distant Quasars into View*. Doctor of Philosophy (Physics), May 2023, 145 pp., 23 tables, 29 figures, 174 numbered references.

The Gemini Near Infrared Spectrograph - Distant Quasar Survey (GNIRS-DQS) is the largest uniform, homogeneous survey of its kind, covering 260 quasars at $1.5 \leq z \leq 3.5$. This unique survey, coupled with data from the Sloan Digital Sky Survey (SDSS), enables new investigations into redshifts, supermassive black hole masses (MBH), and accretion rates at high redshift through spectroscopic coverage of important rest-frame UV-optical emission lines. The importance of this survey is highlighted in the fact that the optical emission lines provide more reliable measurements of these quasar parameters than their UV counterpart. With such a unique sample compiled here, I construct prescriptions to calibrate these quasar parameters derived from rest-frame UV emission lines to those derived from rest-frame optical emission lines. These prescriptions provide important insight into how these parameters depend on redshift and are potentially biased as we look out further into the universe. Additionally, all the work completed with this sample will help shape our understanding of how these quasars and their host galaxies co-evolve over cosmic time.

ACKNOWLEDGEMENTS

I would like to thank my advisor, Dr. Ohad Shemmer, for his guidance, encouragement, and incredible ability to churn through many, many rounds of paper drafts. I would also like to thank the members on my defense committee: Drs. Yuan Li, Chris Littler, and Duncan Weathers, for their help in going through the process of proposal and defense of this dissertation. I would also like to thank my colleague, Brandon Matthews, for working alongside me during my time here at UNT. My work would be only half as complete if it wasn't for our collaborative efforts throughout the years. I would also like to thank my family, who supported me and pushed me through this journey. Without their support, I would not have been able to be where I am at today. Finally, I would like to thank my wife, Allison Dix, for keeping me right during all these long nights and stressful days.

TABLE OF CONTENTS

LIST OF TABLES

LIST OF FIGURES

CHAPTER 1

INTRODUCTION

The dissertation research presented in these chapters is reproduced verbatim from published papers or papers that are undergoing revision for publication. Each chapter includes an introduction of that particular research project that is necessary to understand each investigation, so I do not repeat that here. Instead, I provide a broad background and motivation for the entirety of this work in this section.

1.1. Background

The birth of the study of active galactic nuclei (AGN), or quasars, began in 1959 when Cambridge published the Third Cambridge Catalog of Radio Sources (3C) [11]. In 3C, little to their knowledge at the time, were a few peculiar objects that would later be studied and identified as "quasi-stellar radio sources" or "quasars." With optical spectroscopic followup of these objects, and in particular the object 3C 273, astronomers would open the door to the study of AGN and the embodiment of the work presented throughout this dissertation.

This particular object, 3C 273, was further studied in 1962 after obtaining a precise position by astronomers Cyril Hazard and John Bolton through use of lunar occultations. Maarten Schmidt, using this position, provided the optical spectroscopic followup for this object and was amazed by what he found. Schmidt had taken the optical spectra of a bright radio source and found Balmer emission lines. Not only that, but these emission lines were offset from there laboratory rest-frame wavelength positions by quite some margin. Based on the measurements of this Balmer emission, Schmidt found that if we were to try and describe this offset as the motion of a star, it would suggest that this object would be receding at 47,000 km s^{-1}. Therefore, he concludes that this shift must be a cosmological effect and places the first ever observed AGN at a redshift (z) of $z = 0.158$ [129]. While this groundbreaking discovery should have awarded Schmidt a Nobel Prize, he instead was honored his face on the front of Time Magazine in 1966.

AGN, as we know them today, are the fundamental difference in characterizing a galaxy as active or inactive (normal or regular). Namely, an AGN refers to the presence of a supermassive black hole (SMBH) accreting at the center of its galaxy, thereby making the galaxy "active." This key difference between active and inactive galaxies is represented by the fact that AGN emit substantial radiation over the entire electromagnetic spectrum that is too large to be accounted for by just stellar emission [112]. This emission, however, gives us key insights as to the nature of these "central engines" as well as the evolution of these active galaxies and sparks the motivation for a detailed study of these objects.

1.2. Motivation

In extragalactic astrophysics, we strive to understand the co-evolution of galaxies and their SMBHs. To date, we know there is a strong connection between the emission of the SMBH and the galaxy that hosts it. This fact has been shown in the relationships between the mass of the SMBH ($M_{\rm BH}$) and many properties of the host galaxies, such as bulge mass or stellar velocity dispersion [43, 49, 23]. Additionally, this connection is also represented by the physical properties of the outflowing material from the SMBH, which impacts the host galaxies star formation [61]. Therefore, in any study going forward, it is crucial that we measure the properties of AGN, to the best of our ability, in order to understand how these SMBH and their host galaxies co-evolve.

Measuring the emission from AGN is a daunting task, given the broad wavelength range it covers. The emission spectrum produced by an AGN has been exhaustively studied, but has generally been defined by a power-law continuum in the rest-frame ultraviolet (UV)-optical and X-ray wavelength ranges, and broad and narrow emission lines that are produced from the broad line region (BLR) and the narrow line region (NLR), respectively [74, 104]. In addition to this, many AGN spectra may differ from the "typical" AGN spectrum (see, [156]) in that they may exhibit features of absorption, boosted continua, and weak broad-line emission. While these differences introduce difficulties in studying the spectra of AGN in general, they also provide valuable insights into the overall structure of AGN.

For nearby AGN ($z < 0.8$), we determine their mass, accretion rate, and redshift through rest-frame optical emission lines, such as broad Hβ λ4861 and narrow [O III] $\lambda\lambda$4959, 5007. However, as we attempt to understand how these objects evolve over cosmic time, it is important to measure these parameters at higher redshifts. Unfortunately, at these higher redshifts, we begin to shift these optical diagnostic emission lines into near-infrared (NIR) wavelength ranges. This leaves the observed optical spectra of these higher redshift AGN to contain rest-frame UV emission lines, such as C IV λ1549 and Mg II λ2800. While these emission lines are broad and measurable, neither is an ideal proxy for the rest-frame optical emission lines. For example, [O III] is a narrow emission line that provides a redshift measurement that is, on average, 4 and 8 times less uncertain Mg II and C IV, respectively [138]. Additionally, mass and accretion rate measurements are much less reliable from C IV as it has a complicated emission profile, including non-virial components, that lead to significant uncertainties. Therefore, the work presented throughout this dissertation all leads to a single goal of providing the most reliable measurements of key AGN parameters by mapping the less reliable UV emission lines to the more reliable optical emission lines.

In this dissertation we used a large homogeneous NIR survey, the Gemini Near-Infrared Spectrograph - Distant Quasar Survey (GNIRS-DQS) [90], to investigate redshift, $M_{\rm BH}$, and accretion rate for high redshift quasars. In Chapter 2, we present the pilot project to this work with redshifts using a smaller compiled set of quasars at high redshift. This paper sets out the groundwork for the paper in Chapter 3, by establishing a linear relation that maps the redshift measurements of C IV to [O III]. In Chapter 3, we used the newly acquired GNIRS-DQS sample, extend upon it, and develop a new prescription for redshift measurements stemming from C IV. In Chapter 4, we used the GNIRS-DQS sample to map $M_{\rm BH}$ estimates determined from C IV and Mg II to those determined from Hβ. We also include a correction required for high accretion-rate objects at high redshift in these estimations. In Chapter 5, we used a combined sample of AGN to investigate the properties of weak line quasars and establish a relationship between accretion rate and

C IV "Distance." In Chapter 6, we summarize the work and results stemming from the previous chapters and discuss a few ways this work can be extended upon.

CHAPTER 2

PRESCRIPTIONS FOR CORRECTING ULTRAVIOLET-BASED REDSHIFTS FOR LUMINOUS QUASARS AT HIGH REDSHIFT

2.1. Introduction

The $\log F_{\lambda(SDSS)}/F_{\lambda(GNIRS)}$ best practical indicators for a quasar's systemic redshift (z_{sys}) lie in the rest-frame optical band, particularly the prominent [O III] λ5007, Mg II λ2800, and the Balmer emission lines [e.g., 18, 140]. However, at high-redshift ($z \gtrsim 0.8$), $\approx 10^5$ quasars typically have their z_{sys} values determined from rest-frame ultraviolet (UV) spectra since only 0.1% of these quasars have corresponding rest-frame optical information from near-infrared (NIR) spectra [e.g., 130, 108, 106]. Unfortunately, the UV-based z_{sys} estimates are highly inaccurate and imprecise given that the UV emission lines are usually blueshifted by up to ≈ 3000 km s^{-1} [e.g., 48, 154, 50, 140]. Mitigating these biases requires identifying robust corrections to UV-based redshifts.

Reliable redshift estimates are needed for multiple reasons. For example, accurate redshift estimates provide information on the kinematics of the outflowing material in the vicinity of the supermassive black hole, which likely impacts the star formation rate in the quasar's host galaxy [e.g., 61]. Additionally, various cosmological studies utilize conversions between redshift differences and distances [e.g., 59, 173]. In this context, a velocity offset of 500 km s^{-1} corresponds to a comoving distance of $\approx 5h^{-1}$ Mpc at $z = 2.5$, which can impact our understanding of, e.g., quasar clustering as velocity offsets can be misinterpreted to be distances in the redshift direction [e.g., 45, 117].

The Sloan Digital Sky Survey [SDSS; 169] provides observed-frame optical spectra and redshifts for hundreds of thousands of quasars. The redshifts for these quasars stem from a cross-correlation by a composite quasar template spectrum provided by [156].

[1]This entire chapter is reproduced from Cooper Dix, Ohad Shemmer, Michael S. Brotherton, Richard F. Green, Michelle Mason, and Adam D. Myers, *Prescriptions for correcting ultraviolet-based redshifts for luminous quasars at high redshift*, Astrophysical Journal 893 (2020), no. 1, 14, with permission from IOP Publishing.

Table 2.1. Intrinsic Uncertainty

Emission Line	Uncertainty (km s^{-1})
[O II] λ3727	46
[O III] λ5007	56
[Ne V] λ3426	119
Mg II	205
C III]	233
He II λ1640	242
broad Hβ	400
C IV	415
Si IV	477

However, these estimates become increasingly uncertain in high-redshift quasars because mostly rest-frame UV emission lines are present in the optical band. The first meaningful correction to these UV-based redshifts was achieved by [57, hereafter HW10]. They achieved this by introducing a two-part linear relation between the absolute magnitude and redshift of quasars. A more recent improvement to the HW10 method was achieved by [88, hereafter M17], by comparing [O III]-based z_{sys} values with the spectral properties of the C IV λ1549 emission line for 45 quasars with $z \gtrsim 2.2$.

In this work, we expand on the M17 method by adding high quality NIR spectra of 18 quasars at $2.15 < z < 3.70$. We perform multiple regression analyses and provide improved prescriptions for correcting a variety of UV-based redshifts when the C IV line is available in the spectrum. This paper is organized as follows. In Section 2.2, we describe our sample selection, observations, and data analysis. In Section 2.3, we present our spectroscopic measurements and in Section 2.4 we discuss our results. Our conclusions are presented in Section 2.5. Throughout this paper, we compute luminosity distances using $H_0 = 70$ km s^{-1} Mpc^{-1}, $\Omega_M = 0.3$, and $\Omega_\Lambda = 0.7$ [e.g., 148].

Table 2.2. Observation Log

Quasar	z	z_{ref}[a]	z_{sys}[b]	H[c] (mag)	K[c] (mag)	Obs. Date	Net Exp. (s)
SDSS J013435.67−093102.9	2.225	1	2.214	14.8	13.6	2016 Aug 25	2880
SDSS J014850.64−090712.8	3.303	1	3.329	16.7	15.5	2016 Sep 19	4800
SDSS J073607.63+220758.9[d]	3.464	2	3.445	16.1	14.9	2016 Sep 20	3840
...	...	...	...	...	...	2016 Sep 22	3840
SDSS J142243.02+441721.2	3.530	1	3.651[e]	15.2	14.4	2016 Sep 7	1920
SDSS J153750.10+201035.7	3.413	3	3.413	15.7	15.4	2016 Sep 22	3840
SDSS J153830.55+085517.0	3.563	1	3.550	15.6	14.6	2016 Sep 19	1920
SDSS J154359.43+535903.1[d]	2.379	1	2.364	15.0	14.2	2016 Sep 21	2880
SDSS J154446.33+412035.7[d]	3.551	1	3.567[e]	15.6	15.5	2016 Sep 20	3840
SDSS J154938.71+124509.1	2.377	4	2.369	14.5	13.5	2016 Sep 5	1920
SDSS J155013.64+200154.5	2.196	1	2.188	15.1	14.2	2016 Sep 19	2400
SDSS J160222.72+084538.4[d]	2.276	1	2.275	15.0	14.0	2016 Sep 6	2880
SDSS J163300.13+362904.8[d]	3.575	1	3.570	15.5	15.1	2016 Sep 22	2640
SDSS J165137.52+400218.9	2.342	1	2.338	15.0	13.7	2016 Sep 6	2880
SDSS J172237.85+385951.8	3.390	2	3.367	16.0	15.3	2016 Sep 19	3840
SDSS J210524.47+000407.3[d]	2.307	1	2.344[e]	14.7	13.8	2016 Aug 26	1920
SDSS J212329.46−005052.9	2.268	1	2.270[f]	14.6	13.9	2016 Sep 5	1920
SDSS J221506.02+151208.5	3.285	2	3.284	16.4	15.2	2016 Aug 26	3840
SDSS J235808.54+012507.2	3.401	2	3.389	14.7	13.8	2016 Aug 26	2880

[a](1) HW10; (2) [25]; (3) [123]; (4) [64].

[b]Unless otherwise noted, the systemic redshift was obtained from the peak of the [O III] λ5007 emission line, where available, as explained in the text. Uncertainties on these values, discussed in Section 2.2.1, average $\sim$ 150 km s^{-1}.

[c]Vega-based magnitudes were obtained from 2MASS.

[d]Indicates a BAL quasar.

[e]Systemic redshift was determined from λ_{peak} of the Hβ emission line.

[f]Systemic redshift was determined from λ_{peak} of the Mg II emission line from the SDSS spectrum of the source.

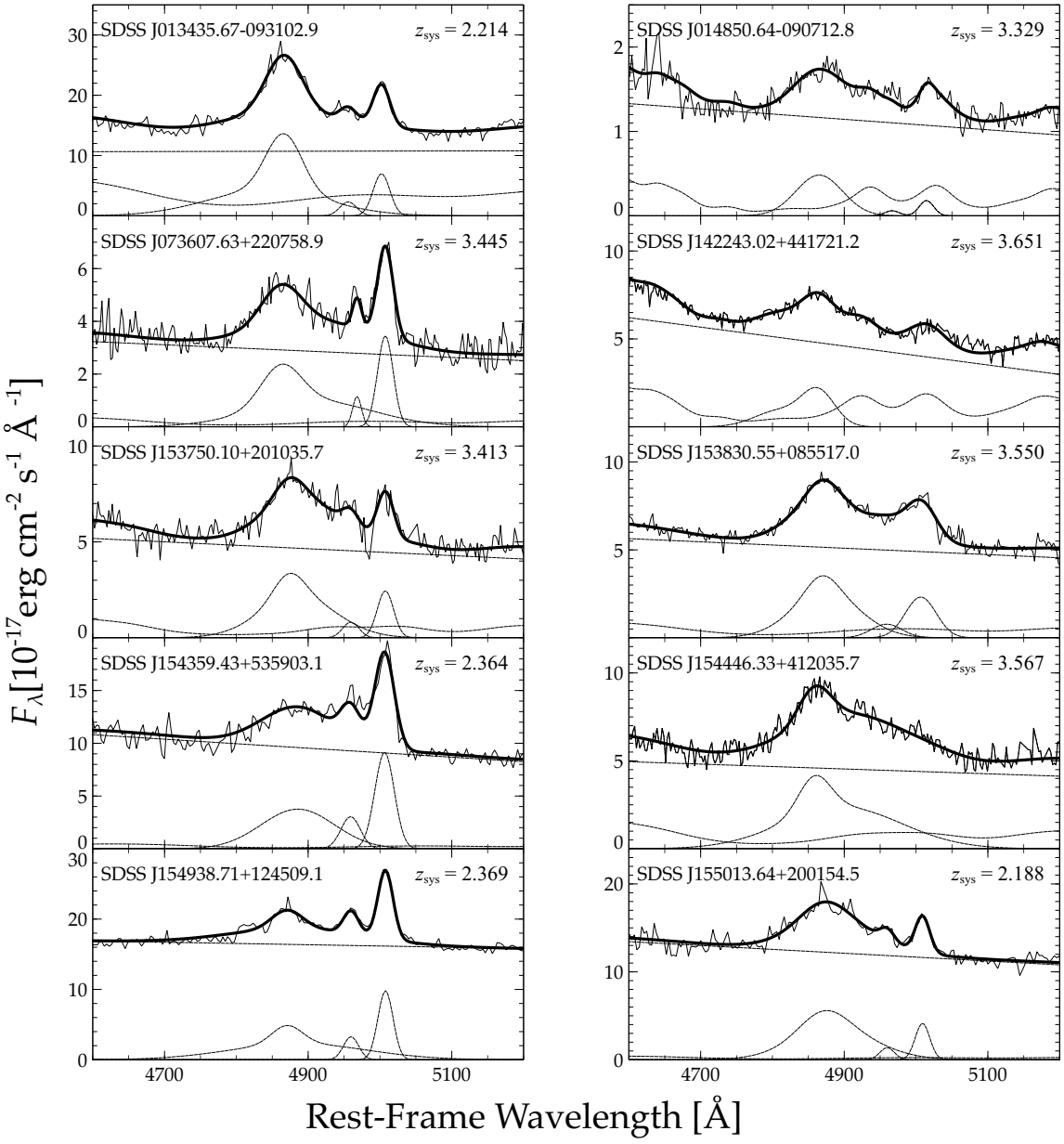

Figure 2.1 NIR spectra of $2.15 < z < 3.70$ quasars. The spectrum in each panel is given by a thin solid line. The fit to each individual feature, Fe II, Hβ, and [O III] where applicable, and the linear continuum are indicated by dashed lines. The overall fit to each spectrum is given by the bold solid line.

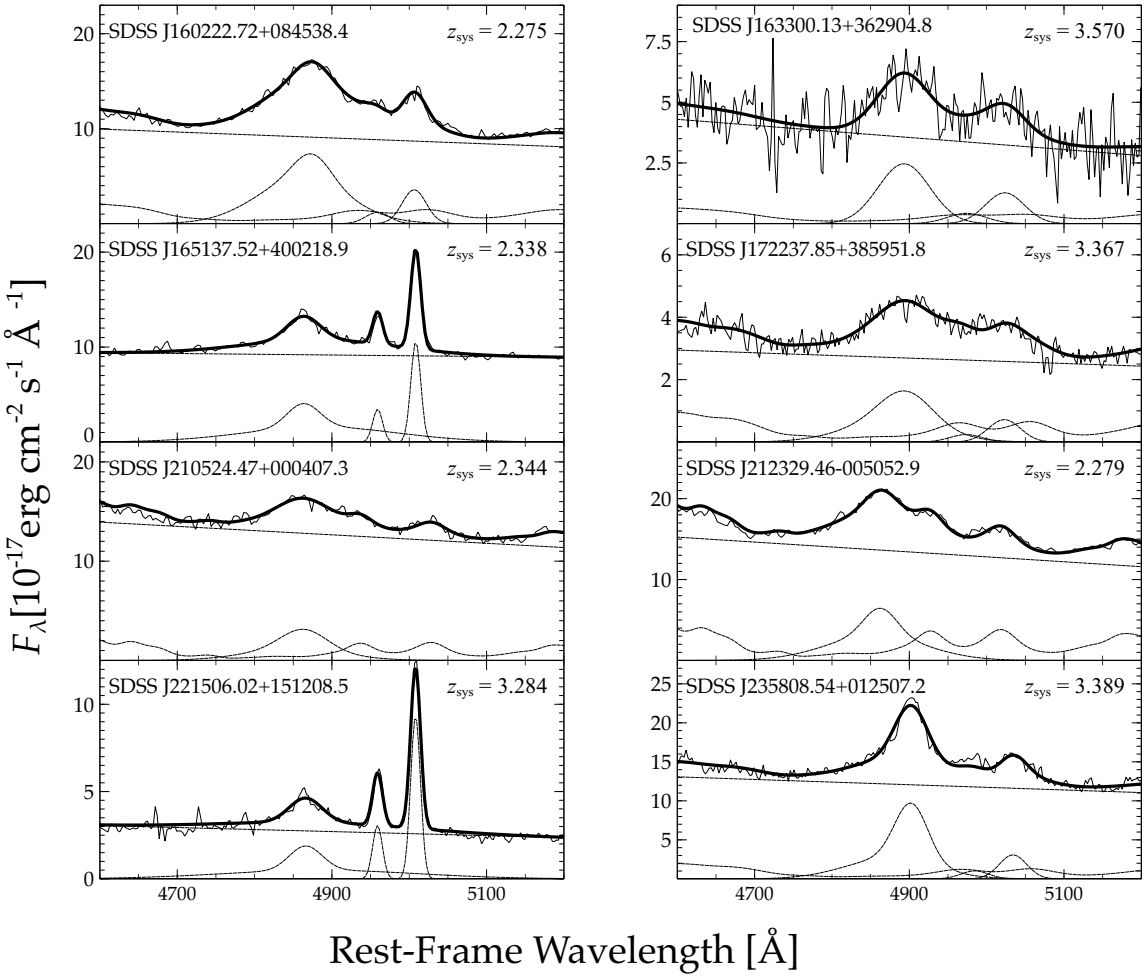

Figure 2.2 Same as Figure 2.1 for the remaining quasars.

2.2. Sample Selection, Observations, and Data Analysis

We have selected a sample of 18 quasars for our investigation based upon the following criteria:

(1) Availability of a flux-calibrated optical spectrum from the SDSS recorded in the Data Release 10 quasar catalog [107].

(2) Brightness in the range $m_i < 18.5$ in order to keep the signal-to-noise (S/N) ratio of the Hβ region of the respective NIR spectrum, obtained with a 3.8 m telescope, at ≈ 40.

(3) Redshift within one of the following intervals, $2.15 < z < 2.65$[2] and $3.20 < z < 3.70$, in which, at a minimum, the Hβ and [O III] lines can be modeled accurately within one of the near-infrared transmission windows in the H or K bands.

Spectroscopic observations of this sample were performed at the United Kingdom Infrared Telescope (UKIRT) on Mauna Kea, Hawaii. The observation log and quasar basic properties appear in Table 2.2.

We utilized the UKIRT Imager-Spectrometer (UIST) with a slit width of 0.24″ to maximize the resolution at the expense of potentially higher slit losses. During these observations, the telescope was nodded in an ABBA pattern in order to obtain primary background subtraction. The broad band B2 filter was used in order to obtain a wavelength range of approximately $1.395 - 2.506$ μm, spanning the H and K bands as necessary. The dispersion for these observations was 10.9 Å pixel^{-1} with a spectral resolution of $R \sim 448$. Standard stars of spectral type G and F were observed on each night alongside the quasar in order to remove the telluric features that are present in the quasars' spectra.

The two-dimensional spectra of the quasars and the standard stars were obtained using standard IRAF[3] routines. Each of the objects was initially pair subtracted in order to remove most of the background noise. Then, both the positive and negative residual peaks were analyzed and averaged together. During the analysis, wavelength calibration was achieved using Argon arc lamps. The hydrogen features in each standard star were removed prior to removing the telluric features from the quasars' spectra.

Removal of the telluric features and the instrumental response from the quasar spectra was done by dividing these spectra by their respective standard star spectra. Then, any remaining cosmic ray signatures on the quasar spectra were carefully removed. Final, flux calibrated quasar spectra were obtained by multiplying these data by blackbody curves with temperatures corresponding to the spectral types of the telluric standards and by a constant factor that was determined by comparing the H, for $2.15 < z < 2.65$, or K, for

[2]This redshift interval ensures spectral converage also of the Hα emission line in the K band.

[3]IRAF (Image Reduction and Analysis Facility) is distributed by the National Optical Astronomy Observatory, which is operated by AURA, Inc., under cooperative agreement with the National Science Foundation.

$3.20 < z < 3.70$, band magnitudes from the Two Micron All Sky Survey [2MASS; 147] to the integrated flux across the respective band using the flux conversion factors from Table A.2 of [15]. We do not rely on the telluric standards for the purpose of flux calibration given the relatively narrow slit and the differences in atmospheric conditions between the observations of the quasars and their respective standard stars. For each source, we utilized their SDSS spectrum to verify that the combined SDSS and UKIRT spectra are consistent with a typical quasar optical-UV continuum of the form $f_\nu \propto \nu^{-0.5}$ [156]. By comparing the flux densities at the rest-frame wavelength of 5100 Å to the flux densities at the rest-frame wavelength in the region of 2000 to 3500 Å, dependent on the redshift, in the SDSS spectrum of each source, we verified that the differences between the two values were within 30%, indicating, at most, only modest flux variations. Such variations, over a temporal baseline of ~ 6 years in the rest-frame are not atypical for such luminous quasars, even if most of these variations are intrinsic as opposed to measurement errors [see, e.g., 67].

2.2.1. Fitting of the UKIRT Spectra

In order to fit the Hβ and Hα spectral regions, we used a model consisting of a local, linear continuum, which is a good approximation to a power-law continuum given the relatively narrow spectral band, a broadened [19] Fe II emission template, and a multi-Gaussian fit to the emission lines. The Fe II template was broadened by a FWHM value that was free to vary between 2000 and 10000 km s^{-1} and, along with the linear continuum, was removed to more accurately fit the Hβ and [O III] emission lines. The chosen FWHM to broaden the Fe II template was determined with a least squares analysis.

We fit the Hβ line using two independent Gaussians, constrained by the width and height of the emission line, simultaneously with one Gaussian for each of the [O III] emission lines. The Gaussians assigned to the [O III] emission lines have identical widths and their intensity ratio was fixed to $I([\text{O III}]\ \lambda 5007)/I([\text{O III}]\ \lambda 4959) = 3$. The wavelengths of the two [O III] components were fixed to the ratio 5007/4959. For the available Hα features, two Gaussians were fit after a linear continuum was fit and subtracted around

the emission line. We do not detect any [N II] emission lines while fitting this region, mainly given our low spectral resolution. The Gaussians were constrained so that the line peak would lie within 1,500 km s^{-1} from the wavelength that corresponded to the maximum of the emission line region, the widths could range from 0 km s^{-1} to 15,000 km s^{-1}, and the flux density was restricted to lie within 0 and twice the maximum value of the emission line.

To estimate the uncertainties on the FWHM and rest-frame equivalent width (EW) of the emission lines, we performed the fitting by adjusting the placement of the continuum according to the noise level in the continuum [see, e.g., 135]. Namely, by adjusting the local linear continuum between extremes of the noise around each emission line, we were able to derive an estimate for uncertainties on the FWHM and EW values. For all but two of the sources, the uncertainties on the values of FWHM and EW in the Hβ region are on the order of $\sim$ 5-15%. For SDSS J014850.64−090712.8 and SDSS J163300.13+362904.8, these uncertainties are on the order of $\sim$ 40%. Similarly, the uncertainties on the FWHM and EW values for the Hα emission line are up to $\sim$ 5%.

The uncertainties on the wavelengths of the peaks of all the emission lines are up to $\sim$ 300 km s^{-1}. The majority of this uncertainty arises from the resolution of our spectrograph, however, our choice of a narrow slit was used to combat this. The uncertainty introduced from the pixel-wavelength calibration is minimal, averaging $\sim$ 5 km s^{-1}. The narrow [O III] λ5007 emission line provided our most accurate redshift estimates, having uncertainties on wavelength measurements averaging $\sim$ 150 km s^{-1}. The wavelength uncertainties were determined by evaluating our S/N ratio and repeated measurements of each of the emission lines.

Spectral properties from those fits are reported in Table 2.3. Columns (2), (3), and (4) provide the FWHM, EW, and the observed-frame wavelength of the peak (λ_{peak}) of the Hβ line, respectively. Columns (5–7) and (8–10) provide similar information for the [O III] λ5007 and Hα emission lines, respectively. The fits for the Hβ and [O III] emission lines appear in Figure 2.1, and the fits for the Hα emission line appear in Figure 2.3.

Table 2.3. Spectral Measurements of the Hβ Region and Hα

Quasar	FWHM$_{H\beta}$ (km s^{-1})	EW$_{H\beta}$ (Å)	$\lambda_{peak,H\beta}$ (Å)	FWHM$_{[O\,III]}$ (km s^{-1})	EW$_{[O\,III]}$ (Å)	$\lambda_{peak,[O\,III]}$[a] (Å)	FWHM$_{H\alpha}$ (km s^{-1})	EW$_{H\alpha}$ (Å)	$\lambda_{peak,H\alpha}$ (Å)
SDSS J013435.67−093102.9	4438	99.7	15656	1625	14.6	16091	2882	444	21125
SDSS J014850.64−090712.8	4716	33.7	21035	1513	4.3	21680	···	···	···
SDSS J073607.63+220758.9[b]	6876	94.3	21625	1640	31.6	22256	···	···	···
SDSS J142243.02+441721.2	4563	39.9	22607	···	···	···	···	···	···
SDSS J153750.10+201035.7	5107	69.5	21516	1613	14.6	22094	···	···	···
SDSS J153830.55+085517.0	5512	70.8	22161	3192	26.1	22782	···	···	···
SDSS J154359.43+535903.1	8301	54.3	16495	1835	28.6	16843	7495	543	22171
SDSS J154446.33+412035.7	7235	132.4	22202	···	···	···	···	···	···
SDSS J154938.71+124509.1	5495	42.4	16408	1544	15.4	16866	5550	374	22139
SDSS J155013.64+200154.5	6539	61.9	15544	1325	7.5	15960	5178	391	20962
SDSS J160222.72+084538.4	6676	122.3	15951	2387	19.5	16398	5629	586	21517
SDSS J163300.13+362904.8	4876	57.8	22297	3768	24.6	22884	···	···	···
SDSS J165137.52+400218.9	4405	65.6	16234	957.8	18.5	16713	4380	377	21920
SDSS J172237.85+385951.8	5938	67.9	21300	3028	13.9	21866	···	···	···
SDSS J210524.47+000407.3	5331	25.3	16256	···	···	···	4530	281	21975
SDSS J212329.46−005052.9	4500	48.1	15929	···	···	···	4084	319	21540
SDSS J221506.02+151208.5	4059	100.0	20840	956.9	61.7	21450	···	···	···
SDSS J235808.54+012507.2	3702	63.3	21397	2652	11.6	21974	···	···	···

[a]Corresponding to the [O III] λ5007 component.

[b]SDSS J073607.63+220758.9 was observed on two different nights, as denoted in Table 2.2, and, therefore, we present the values stemming from the stacked spectrum.

2.2.2. Spectral Fitting of the C IV Emission Lines

In order to provide corrections to the UV-based redshifts of our sources, we fit the C IV emission lines present in their SDSS spectra. These fits appear in Figure 2.6. As suggested in M17, the parameters needed for the correction of the UV-based redshifts are the FWHM and EW of the C IV line, as well as the monochromatic luminosity of the continuum at a rest-frame wavelength of 1350 Å.

The C IV emission line was fit with a local, linear continuum and two independent Gaussians under the same constraints as we report for the Hβ and Hα emission lines. The spectral properties resulting from this fitting procedure are reported in Table 4.1. The uncertainties in each of these measurements were determined by the same method used when evaluating the rest-frame optical emission line uncertainties. Along with this fit, the continuum luminosity, L_{1350}, has also been derived by measuring the continuum flux density at rest-frame λ1350 Å and employing our chosen cosmology. These values also appear in Table 4.1.

2.3. Results

Combined with the sources in M17, we have a total of 63 objects in our sample, of which, six of our UKIRT objects were excluded from further analysis due to broad absorption line (BAL)[4] identification: these are noted in Table 2.2. We then remove an additional BAL quasar, SDSS J014049.18−083942.5, from the sample in M17. Furthermore, we have excluded SDSS J013435.67−093102.9 from our sample given that it is a lensed quasar and its rest-frame UV spectrum is severely attenuated by the foreground lensing galaxy [see e.g., 102]. Measurements of the C IV emission line for 52 out of the 55 sources in our combined sample are available in [144]. The C IV FWHM and EW measurements we obtained for 40 of these sources agree to within $\sim$ 20% with those from [144]; similarly, 10 of these sources agree to within $\sim$ 65%. Generally, these discrepancies are inversely proportional to the S/N ratios of the SDSS spectra and are larger in the presence of narrow absorption lines.

[4]Five of these sources are based on BAL quasar identification from [144]; SDSS J073607.63+220758.9 was identified as a BAL quasar following our visual inspection of its SDSS spectrum.

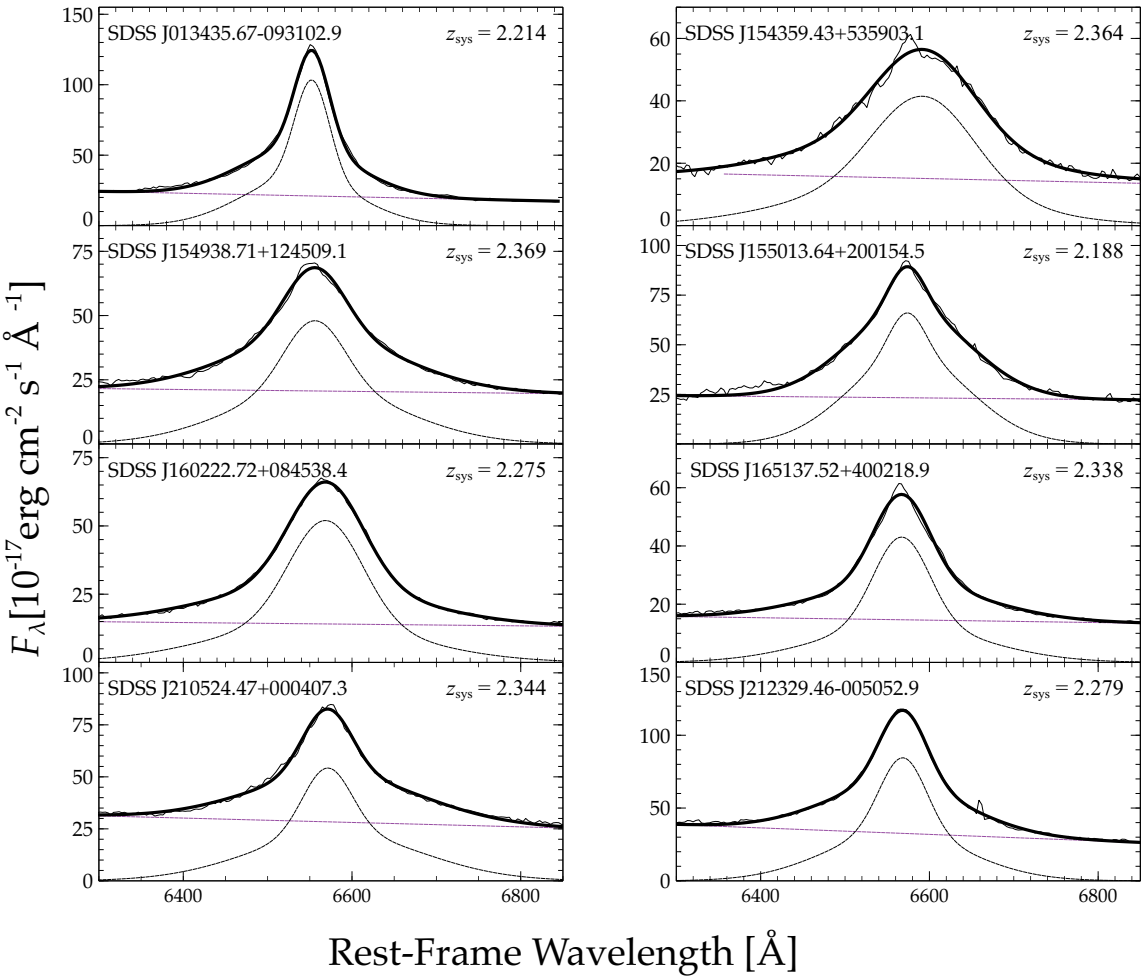

Figure 2.3 NIR spectra of $2.15 < z < 2.65$ quasars. The spectrum in each panel is given by a thin solid line. The fit to the Hα line and linear continuum are indicated by dashed lines. The overall fit to each spectrum is given by the bold solid line.

The spectra for SDSS J025438.36+002132.7 and SDSS J153725.35−014650.3 had extremely poor signal-to-noise ratios, resulting in discrepancies of 108% and 53% for FWHM, and 57% and 210% for EW, respectively, between our measured values and the ones reported in [144]. Substituting our values with the ones reported in [144] for these objects did not have a significant impact on further analysis.

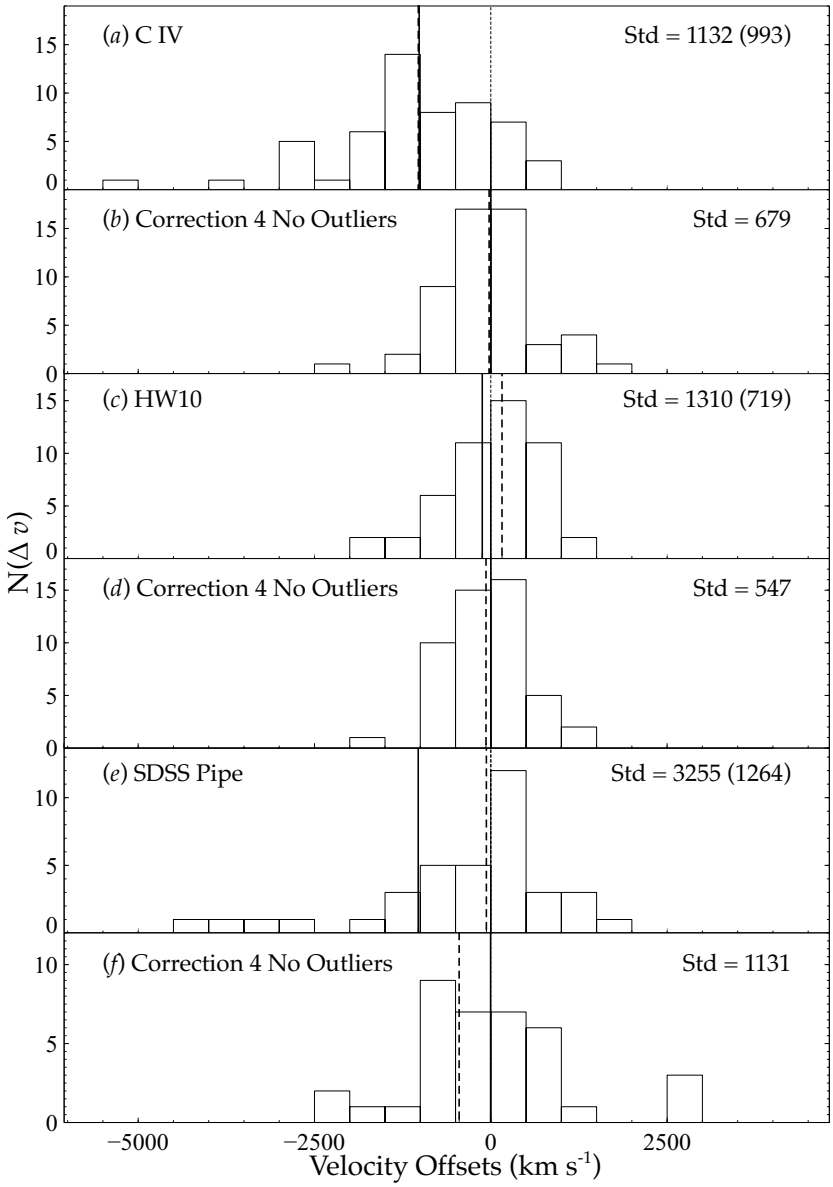

Figure 2.4 Velocity offsets relative to z_{sys} before (panels *a*, *c*, and *e*) and after (panels *b*, *d*, and *f*) the correction provided in bold face in Table 3.7. The numbers reported in parentheses are the standard deviations of the original distributions without the outliers. The mean (solid line) and median (dashed line) are marked in each panel. SDSS J142243.02+441721.2 does not appear on the SDSS Pipe panel, for clarity, because of its abnormally large velocity offset. The outliers that were removed are discussed in Section 2.4.

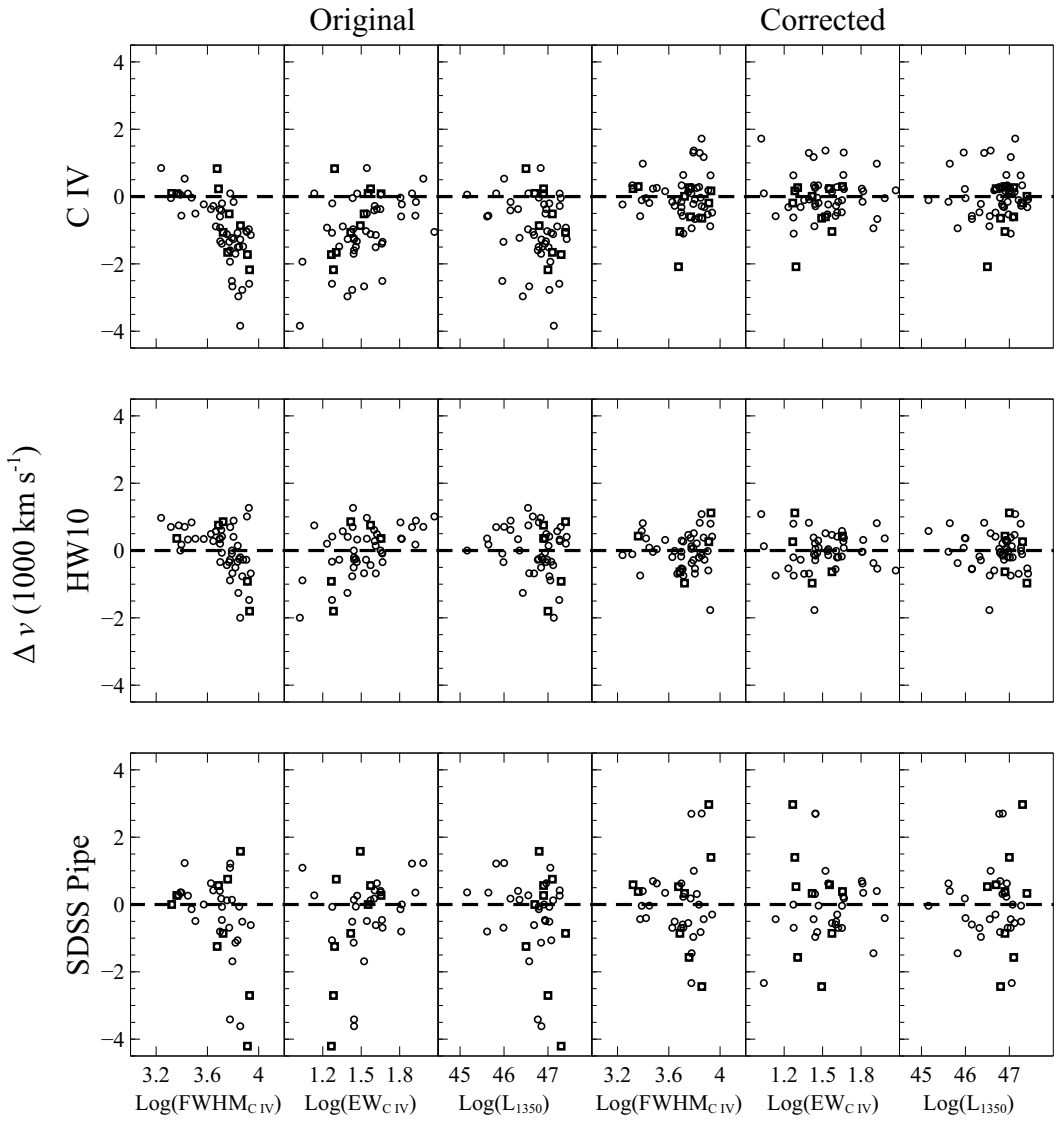

Figure 2.5 The residual velocity offsets with respect to z_{sys} before, three leftmost panels, and after, three rightmost panels, correction are presented against our regression parameters. The corrected method displayed refers to Correction 4 without outliers reported in Table 3.7. Squares (circles) represent data from M17 (UKIRT; this work). The outliers discussed in Section 2.3.1 do not appear in this plot given their abnormally large velocity offsets.

The wavelength of the peak of the C IV emission line was compared to the value predicted by the systemic redshift (z_{sys}) to determine the velocity offset of this line. We now determine z_{sys} from the line peak of the emission line with the smallest uncertainty.

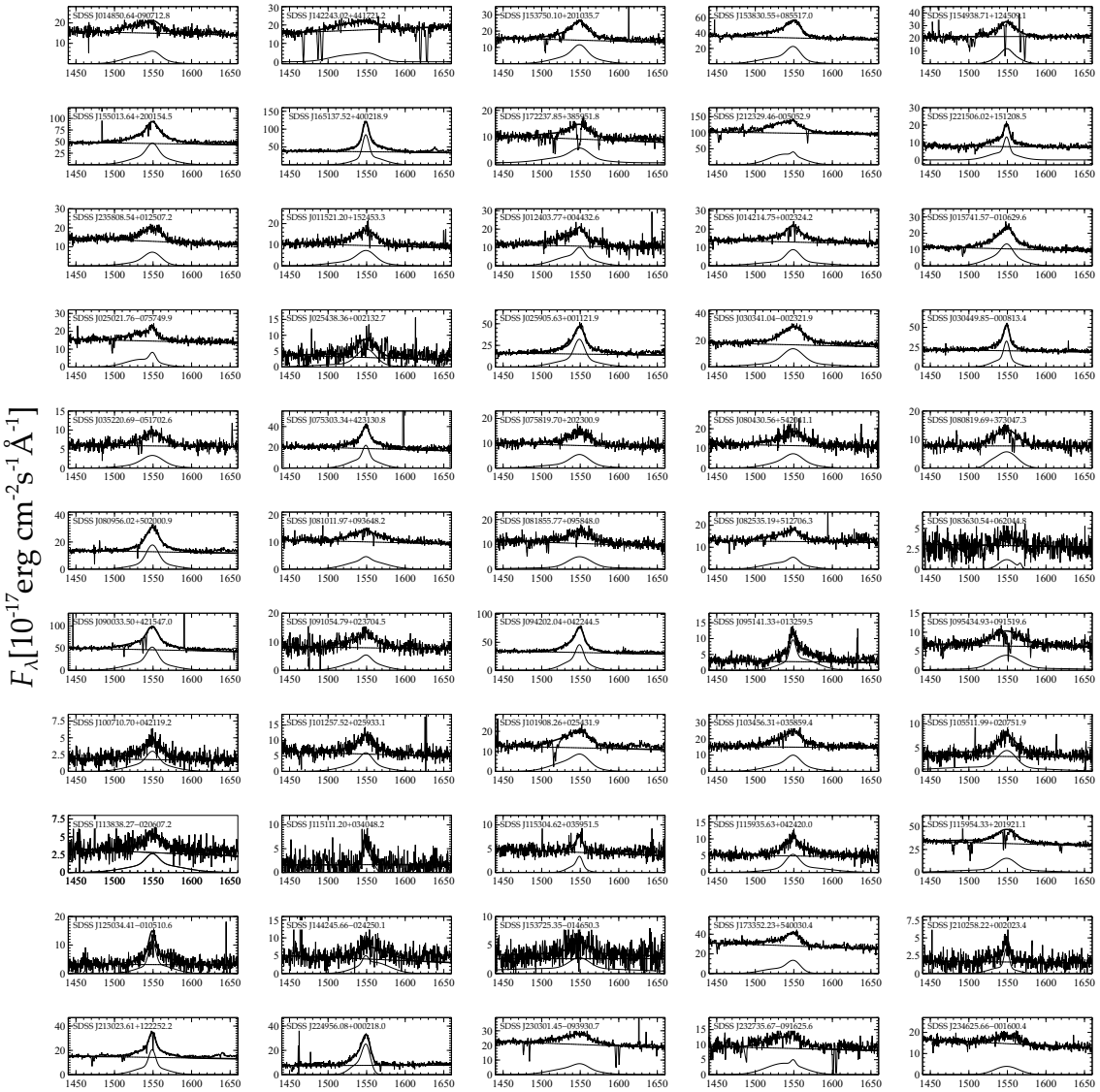

Figure 2.6 C IV fits of all 55 quasars used in the regression analysis. The spectrum and fit to the C IV emission line in each panel are given by a thin solid line. The linear continuum is indicated by a dashed line. The overall fit to each spectrum is given by the bold solid line.

In order, we take our systemic redshift from [O III] (~ 50 km s^{-1}), Mg II (~ 200 km s^{-1}) and Hβ (~ 400 km s^{-1}) [see, 140]. The C IV velocity offsets are shown and reported in Figure 2.4 and Table 2.5, respectively. In Table 2.5, we also report the redshift measurements provided for these sources in HW10 and [106, hereafter P18], where applicable.

Table 2.4. Spectral Measurements of C IV

Quasar Name	FWHM[a] (km s^{-1})	EW[a] (Å)	log L_{1350}[a] (erg s^{-1})	FWHM[b] (km s^{-1})	EW[b] (Å)	log L_{1350}[b] (erg s^{-1})	λ_{peak}[b] (Å)
SDSS J013435.67−093102.9	1045	···	···	···	···	···	···
SDSS J014850.64−090712.8	9545	16.3	47.0	8490	19.2	47.0	6657
SDSS J073607.63+220758.9[c]	···	···	···	2496	10.0	46.8	6872
SDSS J142243.02+441721.2	12475	20.8	47.0	12326	17.9	47.0	7082
SDSS J153750.10+201035.7	6080	37.9	47.1	5886	33.3	47.1	6824
SDSS J153830.55+085517.0	5754	27.1	47.5	5279	26.2	47.4	7023
SDSS J154359.43+535903.1[c]	4713	42.6	47.0	4553	36.9	46.9	5211
SDSS J154446.33+412035.7[c]	15266	192.3	46.3	7350	34.4	46.6	7001
SDSS J154938.71+124509.1	4207	24.2	46.6	4740	19.6	46.5	5233
SDSS J155013.64+200154.5	4273	42.6	47.0	4858	37.4	46.9	4942
SDSS J160222.72+084538.4[c]	4150	27.8	47.0	5615	30.7	47.0	5065
SDSS J163300.13+362904.8[c]	6963	34.9	46.9	6614	42.0	46.8	7067
SDSS J165137.52+400218.9	2818	49.9	46.9	2297	45.2	46.9	5172
SDSS J172237.85+385951.8	···	···	···	7208	31.1	46.8	6745
SDSS J210524.47+000407.3[c]	12603	36.4	47.1	7990	11.9	46.8	5098
SDSS J212329.46−005052.9	8549	16.2	47.4	8168	18.5	47.3	5050
SDSS J221506.02+151208.5	···	···	···	2094	35.8	46.7	6638
SDSS J235808.54+012507.2	···	···	···	5728	20.2	47.1	6761

[a]Columns (2), (3), and (4) were reported in [144].

[b]Columns (5), (6), (7), and (8) were measured from SDSS spectra, as described in the text.

[c]Indicates broad absorption around the C IV line.

The velocity offsets introduced from these redshifts with respect to z_{sys} are presented in Figure 2.4 and Table 2.5. In addition to the velocity offsets for the sources in our UKIRT sample, the velocity offsets from Table 1 of M17 have been included in the following

regression analysis. The C IV emission line properties for the M17 sample are reported in Table 2.6.

We note that the $\Delta v_{\mathrm{C\,IV}}$ values used in M17 differ from the $\Delta v_{\mathrm{C\,IV}}$ values we compute for the M17 sample since M17 used the $\Delta v_{\mathrm{C\,IV}}$ values from [144], combined with the redshift determined from the SDSS Pipeline, in order to find $z_{\mathrm{C\,IV}}$. Our $\Delta v_{\mathrm{C\,IV}}$ values follow directly from the measurement of λ_{peak} (C IV) and our derived z_{sys}. The origin of the discrepancies between the two velocity offsets used stems from the uncertainty in the $\Delta v_{\mathrm{C\,IV}}$ values discussed in [144]. The differences between the $\Delta v_{\mathrm{C\,IV}}$ values we use and those used by M17 are rather small, and using the latter values do not change our results significantly.

A multiple regression analysis has been performed on the velocity offsets and the C IV emission line properties such that:

$$\begin{aligned}\Delta v\ (\mathrm{km\ s^{-1}}) = \alpha \log_{10}(\mathrm{FWHM_{C\,IV}}) \\ +\beta \log_{10}(\mathrm{EW_{C\,IV}}) + \gamma \log_{10}(L_{1350})\end{aligned} \tag{2.1}$$

where Δv is the velocity offset and α, β, and γ are the coefficients associated with our regression analysis. The velocity offset created by each redshift derivation method was determined by the following equation

$$\Delta v = c\left(\frac{z_{meas} - z_{sys}}{1 + z_{sys}}\right). \tag{2.2}$$

Where z_{meas} is the redshift derived using various methods and reported in the studies indicated below. In order to derive the most reliable redshift correction, four regressions were performed using the following parameters from Equation 2.1:

(1) $\log_{10}(\mathrm{FWHM_{C\,IV}})$, $\log_{10}(\mathrm{EW_{C\,IV}})$

(2) $\log_{10}(\mathrm{FWHM_{C\,IV}})$, $\log_{10}(L_{1350})$

(3) $\log_{10}(\mathrm{EW_{C\,IV}})$, $\log_{10}(L_{1350})$

(4) All three parameters

In total, this regression analysis was performed on redshifts determined from: 1) the measured line peak of the C IV emission line, 2) HW10, and 3) the SDSS Pipeline. The coefficients, errors, and confidence statistics from Equation 2.1, determined in each of these cases, are reported in Table 3.6. For the confidence statistics, we report the t-Value to determine the importance of each individual parameter.

The residuals of the velocity offsets after each correction has been determined have been analyzed, and basic statistics resulting from these residuals are listed in Table 3.7. The residuals before and after correction are presented in Figure 3.5. The residual distributions show the significant reduction in the velocity offsets before and after each correction. The corrected velocity offsets for C IV- and HW10-based redshifts are closer to zero than the corrected velocity offsets for the SDSS Pipeline-based redshift, representative of the larger σ value associated with SDSS Pipeline redshift estimates. From evaluating the best fitting coefficients and statistics reported for each correction, we determined the correction that we consider to provide the most reliable results. This correction has been emphasized in bold face in the text.

2.3.1. SDSS J142243.02+441721.2 and SDSS J115954.33+201921.1

SDSS J142243.02+441721.2 from our UKIRT sample has significantly larger velocity offsets compared to the rest of the combined sample. The velocity offsets determined from C IV, HW10, and SDSS Pipeline are -5097 km s^{-1}, -7740 km s^{-1}, and -16384 km s^{-1}, respectively. The latter velocity offset stems from a misidentification of spectral features in the SDSS spectrum of the source as manifested by the SDSS Pipeline products. The SDSS Pipeline redshift for this source is $z = 3.396$ while the SDSS Visual Inspection value is $z = 3.615$. The disparity between these estimates confirms the misidentification of the emission lines by the SDSS Pipeline. Because the velocity offsets for this source had a significant impact on the regression analysis and may be misleading, we have provided the results of the regression analysis with and without this object in Table 3.7.

Table 2.5. Redshift Comparison

Quasar	$z_{\mathrm{C\,IV}}$[a]	Δv (km s^{-1})	z_{pipe}[b]	Δv (km s^{-1})	z_{HW10}[c]	Δv (km s^{-1})
SDSS J013435.67−093102.9	2.214	···	···	···	2.225	1029
SDSS J014850.64−090712.8	3.274	-3786	3.290	-2691	3.303	-1796
SDSS J073607.63+220758.9	3.436	-607	3.464	1285	···	···
SDSS J142243.02+441721.2	3.572	-5097	3.397	-16384	3.531	-7740
SDSS J153750.10+201035.7	3.405	-544	···	···	···	···
SDSS J153830.55+085517.0	3.535	-989	3.537	-856	3.563	858
SDSS J154359.43+535903.1	2.365	89	2.370	536	2.379	1341
SDSS J154446.33+412035.7	3.520	-3087	3.569	131	3.551	-1049
SDSS J154938.71+124509.1	2.378	801	2.355	-1244	···	···
SDSS J155013.64+200154.5	2.190	188	2.194	565	2.196	754
SDSS J160222.72+084538.4	2.270	-458	···	···	2.276	92
SDSS J163300.13+362904.8	3.562	-525	3.538	-2093	3.575	328
SDSS J165137.52+400218.9	2.339	90	2.341	270	2.342	360
SDSS J172237.85+385951.8	3.350	-1168	3.390	1584	···	···
SDSS J210524.47+000407.3	2.293	-4575	···	···	2.307	-3301
SDSS J212329.46−005052.9	2.255	-1376	2.233	-3395	2.269	-92
SDSS J221506.02+151208.5	3.285	70	3.284	0	···	···
SDSS J235808.54+012507.2	3.366	-1572	3.400	753	···	···

[a]Redshifts determined from the λ_{peak} reported in Column (8) of Table 4.1.

[b]Acquired from P18.

[c]Acquired from HW10

The velocity offset of SDSS J115954.33+201921.1, with respect to the redshift determined by the SDSS Pipeline is −10642 km s^{-1}, which is larger than the respective values of the combined sample, excluding SDSS J142243.02+441721.2. SDSS J115954.33+201921.1 was also removed from the SDSS Pipeline regression as discussed more in Section 2.4. Here too, the disparity between the SDSS Pipeline redshift value (z = 3.330) and the respective Visual Inspection value (z = 3.425) indicates a misidentification of spectral features by the SDSS Pipeline.

Table 2.6. C IV Spectral Properties of the M17 Sample

Quasar	z_{HW10}	z_{pipe}	FWHM (km s^{-1})	EW (Å)	log L_{1350} (erg s^{-1})	λ_{peak} (Å)
SDSS J011521.20+152453.3	3.433	3.418	6236	33.3	46.6	6821
SDSS J012403.77+004432.6	3.827	3.836	5646	37.4	47.1	7460
SDSS J014049.18−083942.5[a]	3.726	···	4635	22.7	47.2	7285
SDSS J014214.75+002324.2	3.374	···	5013	29.2	47.0	6753
SDSS J015741.57−010629.6	3.571	3.565	5158	45.9	46.9	7049
SDSS J025021.76−075749.9	3.344	3.337	5173	18.8	47.0	6715
SDSS J025438.36+002132.7	2.464	2.470	5998	78.8	45.8	5355
SDSS J025905.63+001121.9	3.377	3.372	3728	65.6	46.9	6767
SDSS J030341.04−002321.9	3.235	···	6865	41.0	47.0	6524
SDSS J030449.85−000813.4	3.296	···	2066	27.1	47.3	6638
SDSS J035220.69−051702.6	3.271	···	6939	24.7	46.4	6578
SDSS J075303.34+423130.8	3.595	3.594	2804	29.4	47.3	7112
SDSS J075819.70+202300.9	3.753	3.743	6583	27.6	46.8	7333
SDSS J080430.56+542041.1	3.755	3.758	7047	28.7	46.8	7335
SDSS J080819.69+373047.3	3.477	3.426	7183	27.8	46.9	6910
SDSS J080956.02+502000.9	3.288	3.290	4240	41.9	47.0	6623
SDSS J081011.97+093648.2	3.387	···	7558	21.3	46.9	6768
SDSS J081855.77+095848.0	3.688	3.692	7446	26.9	47.0	7213
SDSS J082535.19+512706.3	3.507	3.496	6839	18.7	47.1	6964
SDSS J083630.54+062044.8	3.387	3.413	5971	11.0	47.1	6767
SDSS J090033.50+421547.0	3.294	3.296	4421	40.3	47.3	6639
SDSS J091054.79+023704.5	3.290	3.292	6184	27.7	46.4	6618
SDSS J094202.04+042244.5	3.284	3.272	3208	35.0	46.9	6617
SDSS J095141.33+013259.5	2.419	2.425	2645	96.5	46.0	5293
SDSS J095434.93+091519.6	3.398	3.399	8671	41.1	46.7	6802
SDSS J100710.70+042119.2	2.367	2.354	4988	64.8	45.6	5199
SDSS J101257.52+025933.1	2.441	2.436	5106	39.9	46.1	5312
SDSS J101908.26+025431.9	3.379	···	8012	34.5	47.0	6766
SDSS J103456.31+035859.4	3.388	3.342	5972	27.8	46.8	6767
SDSS J105511.99+020751.9	3.404	···	6372	84.5	46.1	6798
SDSS J113838.27−020607.2	3.347	3.342	5888	46.4	46.0	6711
SDSS J115111.20+034048.2	2.337	2.341	2448	44.8	45.2	5170
SDSS J115304.62+035951.5	3.437	3.430	2379	13.6	46.6	6858

Table 2.6 (cont'd)

Quasar	$z_{\rm HW10}$	z_{pipe}	FWHM (km s^{-1})	EW (Å)	log L_{1350} (erg s^{-1})	λ_{peak} (Å)
SDSS J115935.63+042420.0	3.456	3.457	4969	44.8	46.3	6886
SDSS J115954.33+201921.1	3.432	3.269	6360	24.8	47.4	6827
SDSS J125034.41−010510.6	2.399	2.401	2494	83.7	45.6	5252
SDSS J144245.66−024250.1	2.355	···	6176	46.2	46.0	5155
SDSS J153725.35−014650.3	3.467	···	8098	117.7	46.7	6872
SDSS J173352.23+540030.4	3.435	···	4994	17.1	47.4	6844
SDSS J210258.22+002023.4	3.342	···	1733	35.0	46.8	6723
SDSS J213023.61+122252.2	3.279	···	2596	33.6	47.0	6615
SDSS J224956.08+000218.0	3.323	3.309	2994	64.0	46.8	6677
SDSS J230301.45−093930.7	3.470	···	8425	18.7	47.3	6898
SDSS J232735.67−091625.6	3.470	···	8378	27.3	46.5	6582
SDSS J234625.66−001600.4	3.281	···	7172	10.5	47.1	6892

[a]This object was excluded from the regression analysis after visually inspecting its SDSS spectrum and determining it was a BAL quasar.

Note. — The z_{sys} values used in determining the velocity offsets are reported in Column 3 of Table 1 in M17.

2.4. Discussion

The results of our multiple regression analysis indicate that the most reliable redshift is obtained by correcting the HW10-based redshift employing the FWHM and EW of the C IV line, the monochromatic luminosity at rest-frame 1350 Å, and the respective coefficients listed under the fourth correction to the HW10 method from Table 3.6. Using this correction, and removing SDSS J142243.02+441721.2 from the analysis (see Sec. 2.3.1), we were able to reduce the uncertainty on the redshift determination from 731 km s^{-1} to 543 km s^{-1}, yielding an improvement of $\sim$ 25% with respect to the HW10-based redshifts; similarly, the mean systematic offset of the redshift determination is reduced from −137 km s^{-1} to +1 km s^{-1} (see Table 3.7). For a comparison, utilizing only the M17 sample of 44 sources, the uncertainty on the HW10-based redshifts is reduced by $\sim$ 20%.

Table 2.7. Correction Coefficients

Correction	Equation	Coefficients	Value	Error	t-Value
C IV	$\alpha \log_{10}(\mathrm{FWHM_{C\,IV}}) + \beta \log_{10}(\mathrm{EW_{C\,IV}})$	α	-1301	195	-6.68
		β	2501	472	5.29
	$\alpha \log_{10}(\mathrm{FWHM_{C\,IV}}) + \gamma \log_{10}(L_{1350})$	α	-3966	600	-6.61
		γ	293	48	6.14
	$\beta \log_{10}(\mathrm{EW_{C\,IV}}) + \gamma \log_{10}(L_{1350})$	β	2058	601	3.43
		γ	-88	20	-4.50
	$\alpha \log_{10}(\mathrm{FWHM_{C\,IV}}) + \beta \log_{10}(\mathrm{EW_{C\,IV}}) + \gamma \log_{10}(L_{1350})$	α	-3670	549	-6.68
		β	1604	450	3.57
		γ	217	48	4.53
HW10	$\alpha \log_{10}(\mathrm{FWHM_{C\,IV}}) + \beta \log_{10}(\mathrm{EW_{C\,IV}})$	α	-1069	254	-4.22
		β	2517	612	4.11
	$\alpha \log_{10}(\mathrm{FWHM_{C\,IV}}) + \gamma \log_{10}(L_{1350})$	α	-3191	869	-3.67
		γ	251	69	3.63
	$\beta \log_{10}(\mathrm{EW_{C\,IV}}) + \gamma \log_{10}(L_{1350})$	β	2219	715	3.10
		γ	-75	24	-3.18
	$\alpha \log_{10}(\mathrm{FWHM_{C\,IV}}) + \beta \log_{10}(\mathrm{EW_{C\,IV}}) + \gamma \log_{10}(L_{1350})$	α	-2834	819	-3.46
		β	1877	652	2.88
		γ	161	71	2.26
SDSS Pipe	$\alpha \log_{10}(\mathrm{FWHM_{C\,IV}}) + \beta \log_{10}(\mathrm{EW_{C\,IV}})$	α	-2380	785	-3.03
		β	5087	1891	2.69
	$\alpha \log_{10}(\mathrm{FWHM_{C\,IV}}) + \gamma \log_{10}(L_{1350})$	α	-8024	2732	-2.94
		γ	613	216	2.83
	$\beta \log_{10}(\mathrm{EW_{C\,IV}}) + \gamma \log_{10}(L_{1350})$	β	4732	2240	2.11
		γ	-176	74	-2.39
	$\alpha \log_{10}(\mathrm{FWHM_{C\,IV}}) + \beta \log_{10}(\mathrm{EW_{C\,IV}}) + \gamma \log_{10}(L_{1350})$	α	-6814	2830	-2.41
		β	3114	2212	1.41
		γ	416	255	1.63

The addition of the five sources from our UKIRT sample that have HW10-based redshifts, comprising a $\sim$ 10% increase in the number of sources with respect to the M17 sample, therefore helped to further reduce the uncertainty on the HW10-based redshifts from $\sim$ 20% to $\sim$ 25%. We anticipate that by utilizing a more representative of several hundred high-redshift quasars, we will be able to further improve these uncertainties sig-

nificantly and the results will become increasingly less biased to small number statistics (e.g., Matthews et al., in prep.).

We note that, when we include the source with the highly discrepant $\Delta v_{\mathrm{C\,IV}}$ value, SDSS J142243.02+441721.2, in the regression analysis, the best redshift estimates are obtained from the corrected C IV-based redshifts (see Table 3.7). Here, the mean systematic redshift offsets reduces from -1023 km s^{-1} to -8 km s^{-1} and the uncertainty on the redshifts determination decreases from 1135 km s^{-1} to 746 km s^{-1} (a $\sim 34\%$ improvement).

As it is apparent, even with this sample of 55 quasars, the methods to determine redshift using rest-frame UV features provide uncertainties as large as $\approx 500 - 700$ km s^{-1}. As reported in the first row of each section of Table 3.7, the uncorrected redshift determinations are significantly inaccurate and imprecise. C IV-based redshifts have a mean systematic offset of ~ 1000 km/s (a blueshift) and a similar value for σ (the standard deviation). The HW10 method further improves these C IV-based redshifts by reducing the systematic offsets by ~ 900 km s^{-1} and σ by ~ 300 km s^{-1}. Our prescription further reduces the systematic offset by an additional ~ 100 km s^{-1} and reduces σ by an additional $\sim 200 - 300$ km s^{-1}. Using the SDSS Pipeline redshift estimate, determined from a principal component analysis on multiple features of a spectrum simultaneously [e.g., 17], the mean systematic velocity offset for our combined sample is the largest and extends beyond 1000 km s^{-1} with a standard deviation of 1324 km s^{-1}. Overall, albeit utilizing a smaller combined sample with respect to the samples we use for C IV- and HW10-based redshifts, the redshifts determined from the SDSS Pipeline provide the least reliable results (see Table 3.7). Our best correction applied to these redshifts improves the mean systematic velocity offset by ~ 1000 km s^{-1}, similar to the improvement achieved for C IV-based redshifts, but yields only a modest improvement in σ which remains large.

In order to test the validity of our method, we have preformed the same regression described in the text on the M17 sources ($\sim 80\%$ of our combined sample) and applied it to the remaining sources acquired from UKIRT. The C IV velocity offsets were used in the regression since this sample was the largest of the three UV-based redshift estimates.

Prior to correction, the sample of 10 UKIRT sources had a mean, median and σ of -641 km s^{-1}, -690 km s^{-1}, and 952 km s^{-1} respectively. After running the regression on the M17 sample and applying the new correction to the UKIRT sources, the mean, median and σ improved to 474 km s^{-1}, 376 km s^{-1}, and 772 km s^{-1} respectively, demonstrating the validity of our method.

The SDSS Pipeline redshift estimate, as noted in P18, is subject to highly uncertain redshift determinations due to lower signal-to-noise ratios or unusual objects. As seen in our relatively small sample, large redshift discrepancies are apparent particularly in two of the 39 objects that we have with available SDSS Pipeline-based redshifts. In each case, the velocity offsets are $> 10^4$ km s^{-1} and, when included in the regression analysis, it nearly tripled the uncertainty on the redshift determination. The most robust redshift determination methods involve a correction based on the C IV spectral properties and UV continuum luminosity to either C IV- or HW10-based redshifts. P18 also provides a redshift based off of visual inspection, z_{VI}. We find that this estimate, where available, provides a much more reliable redshift estimate than the one provided by the SDSS Pipeline. The mean systematic offset for this redshift estimate is -290 km s^{-1} with a standard deviation of 762 km s^{-1}.

Regarding the two sources with extremely large velocity offsets,
SDSS J142243.02+441721.2 and SDSS J115954.33+201921.1, we note that our best corrections for their UV-based redshifts provide only modest improvements to the redshift determinations, and that their negative velocity offsets (i.e., blueshifts) take on positive velocity offsets (i.e., redshifts), after the correction is applied. The velocity offsets for SDSS J142243.02+441721.2 improve from -5097 km s^{-1} to 2300 km s^{-1}, -7740 km s^{-1} to 6016 km s^{-1}, and -16384 km s^{-1} to 11848 km s^{-1} for C IV-, HW10-, and SDSS Pipeline-based redshift estimates, respectively. Similarly, the velocity offsets for SDSS J115954.33+201921.1 changed from -1264 km s^{-1} to -58 km s^{-1}, 407 km s^{-1} to -656 km s^{-1}, and -10642 km s^{-1} to 8720 km s^{-1}, respectively. While most of the corrected velocity offsets are closer to zero, they do not improve appreciably and still affect the statistics significantly.

Table 2.8. Correction Statistics

Model	Mean	Median	σ	Skew
C IV [a]	-1016	-1028	1132 (993)	-1.11
C IV 1	-20	-194	885 (792)	0.55
C IV 2	-3	18	837 (755)	0.66
C IV 3	1	-80	1022 (905)	0.67
C IV 4	**0**	**-24**	**750[b] (679)**	**0.37**
HW10[c]	-121	159	1310 (719)	-4.09
HW 1	-14	-116	1123 (575)	3.86
HW 2	-2	-97	1157 (638)	3.38
HW 3	1	-73	1195 (621)	3.98
HW 4	**1**	**-68**	**1067 (547)[b]**	**3.59**
SDSS Pipe[d]	-1029	-63	3255 (1264)	-3.45
Pipe 1	-31	-558	2954 (1161)	2.78
Pipe 2	-8	-578	2928 (1165)	2.66
Pipe 3	-2	-697	3072 (1200)	3.03
Pipe 4	**-3**	**-449**	**2851 (1131)**	**2.54**

[a]55 objects were used in the full correction statistics and 54 objects were used in the correction statistics excluding outliers.

[b]The best results, with and without outliers, are further discussed in Section 2.4.

[c]50 objects were used in the full correction statistics and 49 objects were used in the correction statistics excluding outliers.

[d]39 objects were used in the full correction statistics and 37 objects were used in the correction statistics excluding outliers.

Note. — Bold results are presented in Figure 2.4. The σ reported in parenthesis is the standard deviation once outliers have been removed. For C IV and HW10, only SDSS J142243.02+441721.2 was removed. For SDSS Pipe, SDSS J142243.02+441721.2 and SDSS J115954.33+201921.1 were removed.

The origin for the abnormally large velocity offset of the SDSS Pipeline redshift of SDSS J115954.33+201921.1 most likely stems from the misidentification of the emis-

sion lines in the SDSS spectra by the SDSS Pipeline, as discussed in 2.3.1. As for SDSS J142243.02+441721.2, the origin of the large velocity offset of the C IV-based redshift is intrinsic to the quasar and this should not be confused with the coincidental abnormally large velocity offset stemming from the failure of the SDSS Pipeline to correctly identify the UV spectral features (see Sec. 3.1). Our measured velocity offset of the C IV line (-5097 km s^{-1}) is consistent, within the errors, with the value reported in Table 6 of [161] for the source (-4670 km s^{-1}). Such sources may point to additional spectral parameters that should be taken into account in future prescriptions for UV-based redshift corrections. While such objects may be rare ($\lesssim 5\%$ in our combined sample), their potential effects on future redshift estimates should be scrutinized to ensure that redshift corrections for the general quasar population are not skewed. The difficulty in correcting the UV-based redshift of SDSS J142243.02+441721.2 is also manifested by the HW10-based redshift which is unable to improve the estimate but rather provides a larger velocity offset (-7740 km s^{-1}) with respect to the C IV-based value (-5097 km s^{-1}).

With our combined sample of 55 high-redshift quasars, we verify large velocity offsets between UV-based redshift estimates and z_{sys}. Our calibrations to the UV-based redshift estimates can be used to establish more reliable estimates for z_{sys} when working with high-redshift quasars in the optical band. This effort will lead to more reliable constraints on a range of measurements that require precise distances for quasars.

2.5. Conclusions

In the coming decade, $\approx 10^6$ high-redshift ($z \gtrsim 0.8$) quasars will have their redshifts determined through large spectroscopic surveys conducted in the visible band (i.e., rest-frame UV band), e.g., the DESI survey [e.g., 79, 33]. Many of these quasars, at $1.5 \lesssim z \lesssim 6.0$, will have the prominent C IV emission line covered in their spectra which can provide means for correcting UV-based redshifts.

Using a sample of 55 quasars, our prescription for correcting UV-based redshifts yields a systematic velocity offset which is consistent with zero and improves the uncertainty on the redshift determination by $\sim 25-35\%$ with respect to the method of HW10.

Table 2.9. Outlier Offsets

Name	Offset Before (km s^{-1})	Offset After (km s^{-1})
SDSS J142243.02+441721.2 (C IV)	-5097	2300
SDSS J142243.02+441721.2 (HW10)	-7740	6016
SDSS J142243.02+441721.2 (SDSS Pipe)	-16384	11848
SDSS J115954.33+201921.1 (C IV)	-1264	-58
SDSS J115954.33+201921.1 (HW10)	407	-656
SDSS J115954.33+201921.1 (SDSS Pipe)	-10642	8720

We also find that UV-based redshifts derived from the SDSS Pipeline provide the least reliable results, and the uncertainties with respect to z_{sys} cannot be reduced appreciably. With a larger, uniform sample of high-redshift quasars with NIR spectroscopy (e.g., Matthews et al., in prep.), we plan to improve the reliability of our redshift estimates further and search for additional spectral properties that may further improve these estimates.

We show that the uncertainties on UV-based redshifts for the majority of high-redshift quasars can be reduced considerably by obtaining NIR spectroscopy of a larger sample of sources and using the [O III]-based systemic redshift to inform a C IV-based regression analysis. The reduction in redshift uncertainties is particularly useful for a range of applications involving accurate cosmological distances.

We gratefully acknowledge the financial support by National Science Foundation grants AST-1815281 (C. D., O. S.), and AST-1815645 (M. S. B., A. D. M.). A.D.M. was supported by the Director, Office of Science, Office of High Energy Physics of the U.S. Department of Energy under Contract No. DE-AC02-05CH1123 and Award No. DE-SC0019022. This research has made use of the NASA/IPAC Extragalactic Database (NED), which is operated by the Jet Propulsion Laboratory, California Institute of Technology, under contract with the National Aeronautics and Space Administration, as well as NASA's Astrophysics Data System Bibliographic Services.

CHAPTER 3

GEMINI NEAR INFRARED SPECTROGRAPH - DISTANT QUASAR SURVEY: AUGMENTED SPECTROSCOPIC CATALOG AND A PRESCRIPTION FOR CORRECTING UV-BASED QUASAR REDSHIFTS

3.1. Introduction

Obtaining systemic redshifts ($z_{\rm sys}$) for quasars to accuracies better than 1000 km s^{-1} is necessary for a variety of reasons. These include measuring the kinematics of outflowing material near the supermassive black hole (SMBH) that impact star formation rates in the quasar's host galaxy [e.g., 61, 83, 24], and cosmological studies that utilize redshifts as distance indicators, such as quasar clustering and the proximity effect at high redshift [e.g., 1, 59, 145, 30, 91, 173].

A quasar $z_{\rm sys}$ value is typically determined from spectroscopy in the optical band relying, particularly, on the wavelength of the peak of the narrow [O III] λ5007 emission line at $z \lesssim 0.8$, the Mg II $\lambda\lambda$2798, 2803 doublet for $0.4 \lesssim z \lesssim 2.3$, or the Balmer lines up to $z \sim 1$, in order of increasing uncertainty on the derived z_{sys} value, ranging from $\sim$ 50 km s^{-1} to $\sim$ 600 km s^{-1} [e.g., 18, 140, 99]. However, at higher redshifts, these $z_{\rm sys}$ indicators shift out of the optical band, and redshift determinations usually rely on shorter wavelength, and typically higher ionization emission lines such as C IV λ1549. Such emission lines are known to show additional kinematic offsets of up to several 10^3 km s^{-1} that add uncertainties of this magnitude to the derived redshift values [e.g., 48, 154, 50, 140, 161]. The redshifts of distant quasars determined from large spectroscopic surveys [e.g., Sloan Digital Sky Survey, SDSS, 169, 151, 33, 82], that are limited to $\lambda_{\rm obs} \lesssim 1$ μm, therefore will have uncertainties on the order of tens of Mpc at $z = 2.5$, when converting from velocity space into comoving distance [e.g., 45].

A direct comparison of SDSS Pipeline redshifts [17, 82] with z_{sys} values obtained from rest-frame optical indicators show that corrections to UV-based redshifts can be made despite the presence of potentially large uncertainties. Past investigations such as Hewett

& Wild 2010 ([57]), Mason et al. 2017 ([88]) and Dix et al. 2020 ([36]), hereafter HW10, M17, and D20, respectively, have demonstrated that these uncertainties can be mitigated through corrections obtained from regression analyses based on pre-existing rest-frame optical spectral properties and used as prescriptions for correcting UV-based redshifts.

HW10 relied primarily on sampling methods wherein an average quasar spectrum was generated using a large sample of existing quasar spectra, and then statistical analysis was used to provide offsets for any given quasar with respect to this "master" spectrum in order to correct for any uncertainties. However, this offset correction becomes less reliable for high redshift quasars as important emission lines such as [O III] and Mg II leave the optical-UV regime, and so additional corrections are needed [see, e.g., 119].

M17 and D20 used regression analyses that apply empirical corrections to UV-based redshifts involving the C IV spectroscopic parameter space, a diagnostic of quasar accretion power [120, 119, 125], which affects the wavelengths of emission-line peaks. Specifically, these parameters include the rest-frame equivalent width (EW) and full width at half maximum intensity (FWHM) of the C IV line[1] as well as the continuum luminosity at the base of this line. Such corrections have been applied to sources that lack broad absorption lines and are not radio-loud[2] in order to minimize the effects of absorption and continuum boosting, respectively, to the C IV line profile to mitigate potential complications arising from these sources and provide the most reliable results possible.

The D20 analysis, an extension of the M17 study, was based on a non-uniform sample of 55 SDSS sources with spectral coverage in the rest-frame optical and UV. Here, we use a much larger and more uniform sample of 154 sources with highly reliable z_{sys} values drawn from an augmentation of the Gemini Near Infrared Spectrograph - Distant Quasar Survey (GNIRS-DQS) near-infrared (NIR) spectral inventory [90, hereafter M21]. Our results allow us to obtain significantly improved prescriptions for correcting UV-based

[1]We discuss additional velocity width measurement methods in Appendix 3.5.

[2]We consider radio-loud quasars to have $R > 100$, where R is defined as $R = f_\nu$(5 GHz) / f_ν (4400 Å), where f_ν(5 GHz) and f_ν(4400 Å) are the flux densities at a rest-frame frequency of 5 GHz and a rest-frame wavelength of 4400 Å, respectively [71]

redshifts. Section 5.2.2 describes the properties of the quasar sample and the respective redshift measurements, along with an augmentation of the M21 catalog of spectral properties from GNIRS-DQS. Section 5.2 presents prescriptions for UV-based quasar redshift corrections based on multiple regression analyses including several velocity width indicators, alongside discussion of the redshift dependence of the velocity offset corrections, and redshift estimates for quasars with extremely high velocity outflows. Our conclusions are presented in Section 3.4. Throughout this paper we adopt a flat ΛCDM cosmology with $\Omega_\Lambda = 1 - \Omega_M = 0.7$ and $H_0 = 70$ k$m\ s^{-1}$ Mpc^{-1} [e.g., 148].

3.2. Sample Selection

Our quasar sample is drawn from GNIRS-DQS, which comprises the largest, most uniform sample of optically selected high-redshift quasars having NIR spectroscopic coverage (M21). The GNIRS-DQS sources were selected from all SDSS quasars [106, 82] having $m_i \lesssim 19.0$ mag at $1.55 \lesssim z \lesssim 3.50$ for which the Hβ and [O III] emission-lines can be covered in either the J, H, or K bands. We augment the original GNIRS-DQS sample with 34 additional sources, selected in a similar fashion as described below, and shown in Figure 3.1. Distributions of radio loudness and [O III] λ5007 EW for the GNIRS-DQS sources are shown in Figures 3.2 and 3.3, respectively.

3.2.1. The Augmented GNIRS-DQS Catalog

We add spectroscopic data for 31 sources that were observed in semester 2020B as part of our GNIRS-DQS campaign (see M21 for a detailed description of the observational strategy and the instrument configuration). In addition, we include spectroscopic data for 11 sources that were observed in a similar fashion, albeit with a narrower slit, 0.30″, in semester 2015A (program GN-2015A-Q-68; PI: Brotherton). Of these 42 sources, 34 (comprising 26 from GNIRS-DQS and 8 from GN-2015A-Q-68) had observations that produced useful spectra that we include in the augmented GNIRS-DQS catalog. This fraction is consistent with the overall success rate of ∼ 80% for all the GNIRS-DQS observations. The observation log of these additional objects is given in Table 3.1.

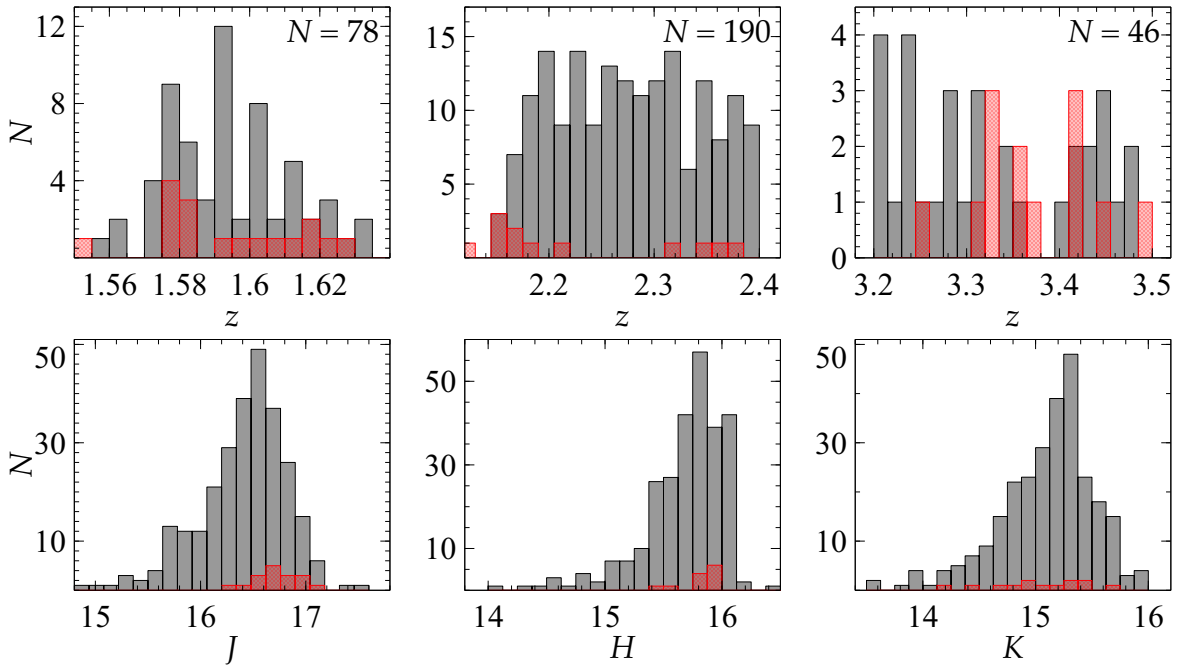

Figure 3.1 Distributions of the most reliable reported redshift estimate from SDSS [82, Table D1, column 27 “Z"] in each redshift interval (top), and corresponding magnitude distributions (bottom). The initial GNIRS-DQS sample is marked in grey, and sources from the augmented sample are shown in red. The three redshift bins correspond to the Hβ and [O III] lines appearing at the center of the J, H, or K photometric bands. The number of sources observed in each redshift bin is marked in each of the top panels. Of a total of 314 sources observed, 272 of which were reported in M21, reliable NIR spectra were obtained for 260 sources; the NIR spectra of 226 of these were presented in M21 and the remaining 34 are presented in this work.

The formatting for the basic spectral properties of all 260 GNIRS-DQS objects is presented in Tables 3.2 and 3.3 in a similar fashion to Tables 2 and 3 in M21. These Tables contain the most reliable measurements for the entire GNIRS-DQS sample. The GNIRS-DQS sample was originally selected from the SDSS quasar catalogs for Data Release (DR) 12 and DR14 [108, 106]; the augmented GNIRS-DQS catalog presented here includes 26 sources that were selected from SDSS DR16 [82] which are marked appropriately in Table 3.1. DR16 measurements have been adopted for the full sample [82].

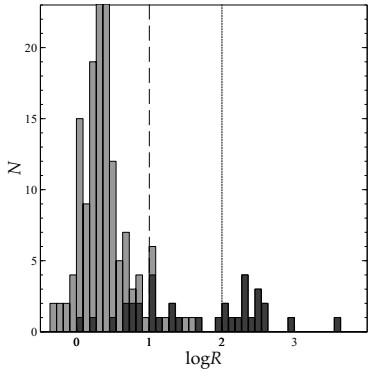

Figure 3.2 Radio-loudness distribution of the GNIRS-DQS sources. Darker shaded regions indicate new sources not in M21. The dashed line at $\log R = 1$ indicates the threshold for radio-quiet quasars, and the dotted line at $\log R = 2$ indicates the threshold for radio-loud quasars (see also M21).

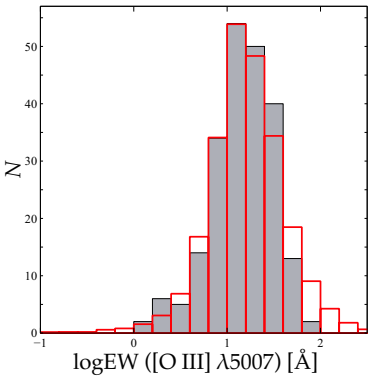

Figure 3.3 [O III] λ5007 rest-frame EW distribution of 222 GNIRS-DQS sources (solid gray histogram) and a similar distribution from Shen et al. (**(year?)**) (red outline; scaled down by a factor of 500). See M21 for additional discussion. We define a threshold of reliability for an [O III] EW measurement at 0.1 Å.

Table 3.4 presents the parameters used to model all of the emission lines, using Gaussian profiles, in the GNIRS-DQS spectra. For each profile, these parameters include the observed-frame wavelength of the line peak, velocity width (FWHM), and flux-density normalization (f_λ). All of the GNIRS spectra and their best-fit models are available electronically at `https://datalab.noirlab.edu/gnirs_dqs.php`[3].

[3] `https://datalab.noirlab.edu/gnirs_dqs.php`

3.2.2. Improved Spectroscopic Inventory

Tables 3.2 and 3.3 include improved measurements of all spectral features. In particular, they include measurements of the rest-frame optical Fe II emission blend which was fitted for each source in the same manner as in M21; however, each such feature now has a measured EW value and errors, thus effectively removing all the upper limits on the EWs (cf. Table 2 of M21). We fit two Gaussians to each broad emission-line profile to accommodate a possible asymmetry arising from, e.g., absorption, or outflows. We note that the two Gaussian fit per broad emission line is adopted only to characterize the line shape; the two Gaussians do not imply two physically distinct regions. The errors on the spectral measurements were calculated in the same manner as the other uncertainties described in M21, with upper and lower values being derived from a distribution of values recorded during the iterative process of broadening the Fe II template (see M21 for a detailed description of the Fe II blend fitting process).

In addition to the inclusion of 34 new sources, Tables 3.2 and 3.3 contain the most reliable data following remeasurement of each source with additional vetting and visual inspection, particularly with respect to the [O III] and Fe II fitting. These values therefore supersede the corresponding values presented in M21.

3.2.3. C IV Emission-Line Measurements

M17 and D20 found that the accuracy and precision of a source's UV-based redshift can be significantly improved when regressed against the FWHM and EW of its C IV line as well as the UV continuum luminosity at a rest-frame wavelength of 1350Å (L_{1350}).[4] The C IV emission line has been measured in the SDSS spectrum of each GNIRS-DQS source using the same fitting approach outlined in D20, which closely follows the methods utilized in both M21 and this work; the C IV emission-line properties of all the GNIRS-DQS sources appear in Dix et al. (2022, in prep).

[4]Objects with redshifts $z < 1.65$ had L_{1350} extrapolated from L_{3000} assuming a continuum power-law of the form $f_\nu \propto \nu^{0.5}$ [e.g., 156].

Table 3.1. Observation Log of Supplemental GNIRS-DQS Objects

Quasar	z_{SDSS}[a]	J	H	K	Obs. Date	Net Exp.	Comments	BAL	RL
		[mag]	[mag]	[mag]		[s]			
(1)	(2)	(3)	(4)	(5)	(6)	(7)	(8)	(9)	(10)
SDSS J001018.88+280932.5*	1.612	16.56	15.80	15.76	2020 Dec 09	1800	···	···	···
SDSS J003001.11−015743.5	1.582	17.08	15.96	15.76	2020 Sep 09	1800	···	···	···
SDSS J003853.15+333044.3	2.357	16.81	15.98	15.29	2020 Dec 25	1800	···	···	···
SDSS J004613.54+010425.7	2.150	16.44	15.85	15.02	2020 Dec 11	1800	···	1	···
SDSS J004710.48+163106.5	2.165	16.33	15.62	14.90	2020 Dec 11	1800	···	···	···
SDSS J005307.71+191022.7*	1.583	16.72	15.79	15.43	2020 Sep 08	1800	···	···	···
SDSS J020329.86-091020.3*	1.579	17.02	15.97	15.64	2020 Aug 23	900	···	···	···
	···	···	···	···	2020 Sep 11	900	···	···	···
SDSS J073132.18+461347.0*	1.578	16.71	15.83	15.31	2020 Sep 29	1350	···	···	···
SDSS J080117.91+333411.9*	1.598	16.73	15.99	15.79	2020 Oct 05	1350	···	···	···
SDSS J080429.61+113013.9*	2.165	16.64	15.99	15.13	2020 Nov 27	1800	···	···	···
SDSS J080636.81+345048.5*	1.553	16.45	15.88	16.58	2020 Sep 30	1800	···	1	···
SDSS J080707.37+260729.1*	2.312	16.84	15.99	15.53	2020 Sep 30	1800	···	···	···
SDSS J081520.94+323512.9*	1.584	16.90	15.85	15.55	2020 Nov 28	1800	2	···	···
SDSS J084017.87+103428.8	3.330	16.69	16.47	15.27	2015 Apr 23	1720	···	···	···
SDSS J084401.95+050357.9	3.350	15.39	14.93	14.19	2015 Apr 06	800	···	···	···
SDSS J084526.75+550546.8*	1.620	16.33	15.65	15.18	2020 Nov 27	1800	···	···	···
SDSS J091425.72+504854.9*	2.341	17.18	15.98	15.17	2020 Nov 29	1800	···	···	···
SDSS J092942.97+064604.1*	1.608	16.65	15.53	15.28	2020 Nov 30	1800	2	···	···
SDSS J094140.16+325703.2*	3.452	16.55	15.81	15.24	2020 Nov 29	1800	···	···	···
SDSS J094427.27+614424.6*	2.340	16.41	15.61	14.72	2020 Dec 09	1800	···	···	···
SDSS J095047.45+194446.1*	1.575	16.80	15.98	15.62	2020 Dec 12	900	···	···	···
	···	···	···	···	2020 Dec 21	900	···	···	···
SDSS J095555.68+351652.6*	1.616	16.99	15.97	15.85	2020 Dec 09	1800	···	···	···
SDSS J101724.26+333403.3*	1.579	16.49	15.84	15.40	2020 Nov 30	1800	···	···	···
SDSS J111127.43+293319.3*	2.178	16.42	15.88	15.10	2020 Dec 31	1800	2	···	···
SDSS J112726.81+601020.2*	2.159	16.60	15.79	15.40	2020 Dec 31	2250	2	···	···
SDSS J112938.46+440325.0*	2.213	16.99	15.88	15.11	2021 Jan 02	1800	···	1	···
SDSS J113330.17+144758.8*	3.248	16.90	15.88	15.64	2021 Jan 02	1800	···	1	···
SDSS J113924.64+332436.9*	2.314	16.38	15.95	14.85	2020 Dec 09	1800	···	···	···

Table 3.1 (cont'd)

Quasar	z_{SDSS}[a]	J	H	K	Obs. Date	Net Exp.	Comments	BAL	RL
		[mag]	[mag]	[mag]		[s]			
(1)	(2)	(3)	(4)	(5)	(6)	(7)	(8)	(9)	(10)
SDSS J122343.15+503753.4	3.491	15.90	15.57	14.69	2015 Mar 30	1160	···	···	···
SDSS J122938.61+462430.5*	2.152	16.30	15.77	15.19	2020 Nov 30	1800	···	···	···
SDSS J130213.54+084208.6	3.305	16.12	15.64	15.02	2015 Apr 01	1720	2	···	···
SDSS J131048.17+361557.7	3.420	15.79	15.11	14.38	2015 Apr 05	800	2	···	···
SDSS J132845.00+510225.8	3.411	16.10	15.53	14.77	2015 Apr 05	1160	···	···	···
SDSS J141321.05+092204.8	3.327	16.16	15.63	15.05	2015 Apr 05	1160	···	···	···
SDSS J142123.97+463318.0	3.378	16.28	15.49	14.89	2015 Apr 07	1700	···	···	···
SDSS J142755.85−002951.1	3.362	16.60	15.91	15.27	2015 Apr 01	1720	···	···	···
SDSS J165523.09+184708.4	3.327	16.28	15.88	15.19	2015 Apr 08	1720	···	···	···
SDSS J173352.23+540030.4	3.424	15.87	15.72	14.95	2015 Mar 23	1190	···	···	···
	···	···	···	···	2015 Apr 01	680	···	···	···
SDSS J210558.29−011127.5	1.625	16.61	15.49	15.54	2020 Aug 21	2250	1	···	···
SDSS J211251.06+000808.3*	1.618	16.85	15.89	15.89	2020 Aug 19	1800	1	···	···
SDSS J213655.35−080910.1	1.591	16.96	15.56	15.74	2020 Aug 23	1800	···	···	···
SDSS J220139.99+114140.8*	2.382	16.87	15.76	15.84	2020 Aug 30	1800	1	···	···
SDSS J222310.76+180308.1*	1.602	16.70	15.99	15.60	2020 Sep 01	1800	1	···	···
SDSS J223934.45−004707.2	2.121	16.91	15.97	15.70	2020 Oct 03	1800	1	···	···
SDSS J233304.61−092710.9	2.121	16.17	15.41	14.83	2021 Jan 01	1800	1	···	···
	···	···	···	···	2021 Jan 02	900	···	···	···

[a]Value based on best available measurement in SDSS DR16 [82, Table D1, column 27 "Z"]

*Denotes object selected from Data Release 16.

Note. — Several sources have more than one observation, indicated by an empty source name. All SDSS data taken from DR16.

Comments in Column (8) represent:
[1] At least one exposure did not meet our observation conditions requirements.
[2] Observation failed to provide spectrum of the source due to bad weather, instrument artifacts, or other technical difficulties during the observation.

Table 3.2. Column Headings for Spectral Measurements

Column (1)	Name (2)	Bytes (3)	Format (4)	Units (5)	Description (6)
1	OBJ	(1-24)	A24	···	SDSS object designation
2	ZSYS	(26-30)	F5.3	···	Systemic redshifts
3	LC_MG II	(32-36)	I5	Å	Mg II observed-frame wavelength[a]
4	LC_MG II_UPP	(38-39)	I2	Å	Upper uncertainty for the line peak of Mg II
5	LC_MG II_LOW	(41-42)	I2	Å	Lower uncertainty for the line peak of Mg II
6	FWHM_MG II	(44-47)	I4	km s^{-1}	FWHM of Mg II
7	FWHM_MG II_UPP	(49-52)	I4	km s^{-1}	Upper uncertainty of FWHM of Mg II
8	FWHM_MG II_LOW	(54-57)	I4	km s^{-1}	Lower uncertainty of FWHM of Mg II
9	EW_MG II	(59-60)	I2	Å	Rest-frame EW of Mg II
10	EW_MG II_UPP	(62-63)	I2	Å	Upper uncertainty of EW of Mg II
11	EW_MG II_LOW	(65-66)	I2	Å	Lower uncertainty of EW of Mg II
12	AS_MG II	(68-76)	E9.2	···	Asymmetry of the double Gaussian fit profile of Mg II
13	KURT_MG II	(78-81)	F4.2	···	Kurtosis of the double Gaussian fit profile of Mg II
14	LC_HB	(83-87)	I5	Å	Hβ observed-frame wavelength[a]
15	LC_HB_UPP	(89-90)	I2	Å	Upper uncertainty for the line peak of Hβ
16	LC_HB_LOW	(92-93)	I2	Å	Lower uncertainty for the line peak of Hβ
17	FWHM_HB	(95-99)	I5	km s^{-1}	FWHM of Hβ
18	FWHM_HB_UPP	(101-105)	I5	km s^{-1}	Upper uncertainty of FWHM of Hβ
19	FWHM_HB_LOW	(107-110)	I5	km s^{-1}	Lower uncertainty of FWHM of Hβ
20	EW_HB	(112-114)	I3	Å	Rest-frame EW of Hβ
21	EW_HB_UPP	(116-117)	I2	Å	Upper uncertainty of EW of Hβ
22	EW_HB_LOW	(119-120)	I2	Å	Lower uncertainty of EW of Hβ
23	AS_HB	(122-130)	E9.2	···	Asymmetry of the double Gaussian fit profile of Hβ
24	KURT_HB	(132-135)	F4.2	···	Kurtosis of the double Gaussian fit profile of Hβ
25	LC_O III	(137-141)	I5	Å	[O III] λ5007 observed-frame wavelength[a]
26	LC_O III_UPP	(143-144)	I2	Å	Upper uncertainty for the line peak of [O III] λ5007
27	LC_O III_LOW	(146-147)	I2	Å	Lower uncertainty for the line peak of [O III] λ5007
28	FWHM_O III	(149-152)	I4	km s^{-1}	FWHM of [O III] λ5007
29	FWHM_O III_UPP	(154-157)	I4	km s^{-1}	Upper uncertainty of FWHM of [O III] λ5007
30	FWHM_O III_LOW	(159-162)	I4	km s^{-1}	Lower uncertainty of FWHM of [O III] λ5007
31	EW_O III	(164-171)	E8.2	Å	Rest-frame EW of [O III] λ5007

Table 3.2 (cont'd)

Column (1)	Name (2)	Bytes (3)	Format (4)	Units (5)	Description (6)
32	EW_O III_UPP	(173-180)	E8.2	Å	Upper uncertainty of EW of [O III] λ5007
33	EW_O III_LOW	(182-189)	E8.2	Å	Lower uncertainty of EW of [O III] λ5007
34	AS_O III	(191-199)	E9.2	···	Asymmetry of the double Gaussian fit profile of [O III] λ5007
35	KURT_O III	(201-204)	F4.2	···	Kurtosis of the double Gaussian fit profile of [O III] λ5007
36	LC_HA	(206-210)	I5	Å	Hα observed-frame wavelength[a]
37	LC_HA_UPP	(212-213)	I2	Å	Upper uncertainty for the line peak of Hα
38	LC_HA_LOW	(215-216)	I2	Å	Lower uncertainty for the line peak of Hα
39	FWHM_HA	(218-221)	I4	km s^{-1}	FWHM of Hα
40	FWHM_HA_UPP	(223-226)	I4	km s^{-1}	Upper uncertainty of FWHM of Hα
41	FWHM_HA_LOW	(228-231)	I4	km s^{-1}	Lower uncertainty of FWHM of Hα
42	EW_HA	(233-235)	I3	Å	Rest-frame EW of Hα
43	EW_HA_UPP	(237-238)	I2	Å	Upper uncertainty of EW of Hα
44	EW_HA_LOW	(240-241)	I2	Å	Lower uncertainty of EW of Hα
45	AS_HA	(243-251)	E9.2	···	Asymmetry of the double Gaussian fit profile of Hα
46	KURT_HA	(253-256)	F4.2	···	Kurtosis of the double Gaussian fit profile of Hα
47	FWHM_FE II	(258-262)	F5.0	km s^{-1}	FWHM of the kernel Gaussian used to broaden the Fe II template
48	EW_FE II	(264-271)	E8.2	Å	Rest-frame EW of optical band Fe II as defined by [19]
49	EW_FE II_UPP	(273-280)	E8.2	Å	Upper uncertainty of EW of Fe II
50	EW_FE II_LOW	(282-289)	E8.2	Å	Lower uncertainty of EW of Fe II
51	LOGFλ5100	(291-296)	F6.2	erg s^{-1}cm^{-2}Å^{-1}	Flux density at rest-frame 5100 Å
52	LOGL5100	(298-302)	F5.2	erg s^{-1} Å^{-1}	Monochromatic luminosity at rest-frame 5100 Å based on z_{sys}

[a]The emission-line peak based on the peak-fit value.

Note. — Data formatting used for the catalog. Asymmetry is defined here as the skewness of the Gaussian fits, i.e., a measure of the asymmetry of the distribution about its mean, $s = E(x - \mu)^3/\sigma^3$, where μ is the mean of x, σ is the standard deviation of x, and $E(t)$ is the expectation value. Kurtosis is the quantification of the "tails" of the Gaussian fits defined as $k = E(x - \mu)^4/\sigma^4$. All of the GNIRS spectra and their best-fit models are available electronically at`https://datalab.noirlab.edu/gnirs_dqs.php`.

Table 3.3. Column Headings for Supplemental Emission-Line Measurements

Column (1)	Name (2)	Bytes (3)	Format (4)	Units (5)	Description (6)
1	OBJ	(1-24)	A24	···	SDSS object designation
2	LC_HD	(26-30)	I5	Å	Hδ observed-frame wavelength[a]
3	LC_HD_UPP	(32-33)	I2	Å	Upper uncertainty for the line peak of Hδ
4	LC_HD_LOW	(35-36)	I2	Å	Lower uncertainty for the line peak of Hδ
5	FWHM_HD	(38-41)	I4	km s^{-1}	FWHM of Hδ
6	FWHM_HD_UPP	(43-45)	I3	km s^{-1}	Upper uncertainty of FWHM of Hδ
7	FWHM_HD_LOW	(47-49)	I3	km s^{-1}	Lower uncertainty of FWHM of Hδ
8	EW_HD	(51-52)	I2	Å	Rest-frame EW of Hδ
9	EW_HD_UPP	(54-55)	I2	Å	Upper uncertainty of EW of Hδ
10	EW_HD_LOW	(57-58)	I2	Å	Lower uncertainty of EW of Hδ
11	AS_HD	(60-68)	E9.2	···	Asymmetry of the double Gaussian fit profile of Hδ
12	KURT_HD	(70-73)	F4.2	···	Kurtosis of the double Gaussian fit profile of Hδ
13	LC_HG	(75-79)	I5	Å	Hγ observed-frame wavelength[a]
14	LC_HG_UPP	(81-82)	I2	Å	Upper uncertainty for the line peak of Hγ
15	LC_HG_LOW	(84-85)	I2	Å	Lower uncertainty for the line peak of Hγ
16	FWHM_HG	(87-90)	I4	km s^{-1}	FWHM of Hγ
17	FWHM_HG_UPP	(92-95)	I4	km s^{-1}	Upper uncertainty of FWHM of Hγ
18	FWHM_HG_LOW	(97-100)	I4	km s^{-1}	Lower uncertainty of FWHM of Hγ
19	EW_HG	(102-103)	I2	Å	Rest-frame EW of Hγ
20	EW_HG_UPP	(105-106)	I2	Å	Upper uncertainty of EW of Hγ
21	EW_HG_LOW	(108-109)	I2	Å	Lower uncertainty of EW of Hγ
22	AS_HG	(111-119)	E9.2	···	Asymmetry of the double Gaussian fit profile of Hγ
23	KURT_HG	(121-124)	F4.2	···	Kurtosis of the double Gaussian fit profile of Hγ
24	LC_O II[b]	(126-130)	I5	Å	[O II] observed-frame wavelength[a]
25	LC_O II_UPP	(132-133)	I2	Å	Upper uncertainty for the line peak of [O II]
26	LC_O II_LOW	(135-136)	I2	Å	Lower uncertainty for the line peak of [O II]
27	FWHM_O II	(138-141)	I4	km s^{-1}	FWHM of [O II]
28	FWHM_O II_UPP	(143-147)	I5	km s^{-1}	Upper uncertainty of FWHM of [O II]

Table 3.3 (cont'd)

Column (1)	Name (2)	Bytes (3)	Format (4)	Units (5)	Description (6)
29	FWHM_O II_LOW	(149-152)	I4	km s^{-1}	Lower uncertainty of FWHM of [O II]
30	EW_O II	(154-155)	I2	Å	Rest-frame EW of [O II]
31	EW_O II_UPP	(157-158)	I2	Å	Upper uncertainty of EW of [O II]
32	EW_O II_LOW	(160-161)	I2	Å	Lower uncertainty of EW of [O II]
33	AS_O II	(163-171)	E9.2	···	Asymmetry of the double Gaussian fit profile of [O II]
34	KURT_O II	(173-176)	F4.2	···	Kurtosis of the double Gaussian fit profile of [O II]
35	LC_NE III[c]	(178-182)	I5	Å	[Ne III] observed-frame wavelength[a]
36	LC_NE III_UPP	(184-185)	I2	Å	Upper uncertainty for the line peak of [Ne III]
37	LC_NE III_LOW	(187-188)	I2	Å	Lower uncertainty for the line peak of [Ne III]
38	FWHM_NE III	(190-193)	I4	km s^{-1}	FWHM of [Ne III]
39	FWHM_NE III_UPP	(195-198)	I4	km s^{-1}	Upper uncertainty of FWHM of [Ne III]
40	FWHM_NE III_LOW	(200-203)	I4	km s^{-1}	Lower uncertainty of FWHM of [Ne III]
41	EW_NE III	(205-206)	I2	Å	Rest-frame EW of [Ne III]
42	EW_NE III_UPP	(208-209)	I2	Å	Upper uncertainty of EW of [Ne III]
43	EW_NE III_LOW	(211-212)	I2	Å	Lower uncertainty of EW of [Ne III]
44	AS_NE III	(214-222)	E9.2	···	Asymmetry of the double Gaussian fit profile of [Ne III]
45	KURT_NE III	(224-227)	F4.2	···	Kurtosis of the double Gaussian fit profile of [Ne III]

[a]The emission-line peak based on the peak-fit value.

[b][O II] λ 3727

[c][Ne III] λ 3870

Note. — Data formatting used for the supplemental measurements in the supplemental features catalog.

Table 3.4. Column Headings for Gaussian Parameters of Emission-Line Profiles

Column (1)	Name (2)	Bytes (3)	Format (4)	Units (5)	Description (6)
1	OBJ	(1-24)	A24	···	SDSS object designation
2	MG II_LAM_PEAK_NARROW	(26-29)	I4	Å	Narrow Mg II peak[a]
3	MG II_STD_NARROW	(31-32)	I2	Å	Narrow Mg II width
4	MG II_F_LAM_NARROW	(34-37)	I4	erg $s^{-1}cm^{-2}Å^{-1}$	Narrow Mg II normalization
5	MG II_LAM_PEAK_BROAD	(39-42)	I4	Å	Broad Mg II peak[a]
6	MG II_STD_BROAD	(44-47)	I4	Å	Broad Mg II width
7	MG II_F_LAM_BROAD	(49-52)	I4	erg $s^{-1}cm^{-2}Å^{-1}$	Broad Mg II normalization
8	O II_LAM_PEAK_NARROW	(54-57)	I4	Å	Narrow [O II] peak[a]
9	O II_STD_NARROW	(59-60)	I2	Å	Narrow [O II] width
10	O II_F_LAM_NARROW	(62-65)	I4	erg $s^{-1}cm^{-2}Å^{-1}$	Narrow [O II] normalization
11	O II_LAM_PEAK_BROAD	(67-70)	I4	Å	Broad [O II] peak[a]
12	O II_STD_BROAD	(72-75)	I4	Å	Broad [O II] width
13	O II_F_LAM_BROAD	(77-78)	I2	erg $s^{-1}cm^{-2}Å^{-1}$	Broad [O II] normalization
14	NE III_LAM_PEAK_NARROW	(80-83)	I4	Å	Narrow [Ne III] peak[a]
15	NE III_STD_NARROW	(85-86)	I2	Å	Narrow [Ne III] width
16	NE III_F_LAM_NARROW	(88-89)	I2	erg $s^{-1}cm^{-2}Å^{-1}$	Narrow [Ne III] normalization
17	NE III_LAM_PEAK_BROAD	(91-94)	I4	Å	Broad [Ne III] peak[a]
18	NE III_STD_BROAD	(96-99)	I4	Å	Broad [Ne III] width
19	NE III_F_LAM_BROAD	(101-102)	I2	erg $s^{-1}cm^{-2}Å^{-1}$	Broad [Ne III] normalization
20	HD_LAM_PEAK_NARROW	(104-107)	I4	Å	Narrow Hδ peak[a]
21	HD_STD_NARROW	(109-110)	I2	Å	Narrow Hδ width
22	HD_F_LAM_NARROW	(112-113)	I2	erg $s^{-1}cm^{-2}Å^{-1}$	Narrow Hδ normalization
23	HD_LAM_PEAK_BROAD	(115-118)	I4	Å	Broad Hδ peak[a]
24	HD_STD_BROAD	(120-123)	I4	Å	Broad Hδ width
25	HD_F_LAM_BROAD	(125-127)	I3	erg $s^{-1}cm^{-2}Å^{-1}$	Broad Hδ normalization

Table 3.4 (cont'd)

Column (1)	Name (2)	Bytes (3)	Format (4)	Units (5)	Description (6)
26	HG_LAM_PEAK_NARROW	(129-132)	I4	Å	Narrow Hγ peak[a]
27	HG_STD_NARROW	(134-135)	I2	Å	Narrow Hγ width
28	HG_F_LAM_NARROW	(137-139)	I3	erg s^{-1}cm^{-2}Å^{-1}	Narrow Hγ normalization
29	HG_LAM_PEAK_BROAD	(141-144)	I4	Å	Broad Hγ peak[a]
30	HG_STD_BROAD	(146-149)	I4	Å	Broad Hγ width
31	HG_F_LAM_BROAD	(151-153)	I3	erg s^{-1}cm^{-2}Å^{-1}	Broad Hγ normalization
32	HB_LAM_PEAK_NARROW	(155-158)	I4	Å	Narrow Hβ peak[a]
33	HB_STD_NARROW	(160-162)	I3	Å	Narrow Hβ width
34	HB_F_LAM_NARROW	(164-166)	I3	erg s^{-1}cm^{-2}Å^{-1}	Narrow Hβ normalization
35	HB_LAM_PEAK_BROAD	(168-171)	I4	Å	Narrow Hβ peak[a]
36	HB_STD_BROAD	(173-175)	I3	Å	Broad Hβ width
37	HB_F_LAM_BROAD	(177-179)	I3	erg s^{-1}cm^{-2}Å^{-1}	Broad Hβ normalization
38	O III_1_LAM_PEAK_NARROW	(181-184)	I4	Å	Narrow [O III] 4959Å peak[a]
39	O III_1_STD_NARROW	(186-187)	I2	Å	Narrow [O III] 4959Å width
40	O III_1_F_LAM_NARROW	(189-191)	I3	erg s^{-1}cm^{-2}Å^{-1}	Narrow [O III] 4959Å normalization
41	O III_1_LAM_PEAK_BROAD	(193-196)	I4	Å	Broad [O III] 4959Å peak[a]
42	O III_1_STD_BROAD	(198-200)	I3	Å	Broad [O III] 4959Å width
43	O III_1_F_LAM_BROAD	(202-204)	I3	erg s^{-1}cm^{-2}Å^{-1}	Broad [O III] 4959Å normalization
44	O III_2_LAM_PEAK_NARROW	(206-209)	I4	Å	Narrow [O III] 5007Å peak[a]
45	O III_2_STD_NARROW	(211-212)	I2	Å	Narrow [O III] 5007Å width
46	O III_2_F_LAM_NARROW	(214-216)	I3	erg s^{-1}cm^{-2}Å^{-1}	Narrow [O III] 5007Å normalization
47	O III_2_LAM_PEAK_BROAD	(218-221)	I4	Å	Broad [O III] 5007Å peak[a]
48	O III_2_STD_BROAD	(223-225)	I3	Å	Broad [O III] 5007Å width
49	O III_2_F_LAM_BROAD	(227-229)	I3	erg s^{-1}cm^{-2}Å^{-1}	Broad [O III] 5007Å normalization
50	HA_LAM_PEAK_NARROW	(231-234)	I4	Å	Narrow Hα peak[a]

Table 3.4 (cont'd)

Column (1)	Name (2)	Bytes (3)	Format (4)	Units (5)	Description (6)
51	HA_STD_NARROW	(236-238)	I3	Å	Narrow Hα width
52	HA_F_LAM_NARROW	(240-243)	I4	erg s^{-1}cm^{-2}Å^{-1}	Narrow Hα normalization
53	HA_LAM_PEAK_BROAD	(245-248)	I4	Å	Broad Hα peak[a]
54	HA_STD_BROAD	(250-252)	I3	Å	Broad Hα width
55	HA_F_LAM_BROAD	(254-256)	I3	erg s^{-1}cm^{-2}Å^{-1}	Broad Hα normalization

[a]The Gaussian profile peak based on the peak-fit value.

Note. — Independent Gaussian feature fit parameters for each emission line that was fit with both a narrow and broad Gaussian profile.

3.3. Correcting UV-Based Redshifts

Our aim is to derive corrections that, on average, shift the velocity offsets of the UV-based redshifts as close as possible to a velocity offset of zero km s^{-1} from $z_{\rm sys}$ based on the [O III] λ5007 line. We make this correction by applying a regression analysis to a calibration sample of 154 sources from GNIRS-DQS as described below.

The sample used for this analysis is a subset of the augmented GNIRS-DQS sample described in Section 5.2.2. Starting with the 260 GNIRS-DQS sources with NIR spectra, we include only the 222 objects with [O III] rest-frame EW measurements greater than 0.1 Å which provide the most accurate values of $z_{\rm sys}$ (see Figure 3.3); i.e., 38 sources whose $z_{\rm sys}$ values were based on either Mg II or Hβ were removed. We then remove 52 broad absorption line (BAL) quasars, as the BAL troughs degrade measurements of the EW and FWHM for C IV [e.g., 10, 50]. These two parameters are of importance for our regression analysis. We also remove 17 radio-loud (RL) quasars (having $R > 100$; see Figure 3.2) (one of which, SDSS J114705.24+083900.6, is also classified as a BAL quasar).

Table 3.5. Redshifts and Velocity Offsets

Quasar	$z_{\rm sys}$[a]	$z_{\rm C\,IV}$[b]	Δv_i (km s^{-1})	$z_{\rm HW10}$[c]	Δv_i (km s^{-1})	$z_{\rm Pipe}$[d]	Δv_i (km s^{-1})
SDSS J001018.88+280932.5	1.613	1.611	-230	···	···	1.612	-110
SDSS J001453.20+091217.6	2.340	2.326	-1250	2.344	340	2.308	-2840
SDSS J001813.30+361058.6	2.311	2.303	-750	2.323	1050	2.316	430
SDSS J001914.46+155555.9	2.267	2.263	-370	2.276	830	2.271	350
SDSS J002634.46+274015.5	2.247	2.243	-340	2.247	50	2.267	1850
SDSS J003001.11−015743.5	1.588	1.579	-1030	1.590	200	1.582	-710
SDSS J003416.61+002241.1	1.631	1.626	-560	1.630	-50	1.627	-410
SDSS J003853.15+333044.3	2.366	2.365	-60	···	···	2.357	-770
SDSS J004710.48+163106.5	2.192	2.162	-2770	···	···	2.165	-2490
SDSS J004719.71+014813.9	1.591	1.588	-340	1.590	-130	1.590	-130

[a]Redshifts determined from the [O III] $\lambda_{\rm peak}$ as described in M21.

[b]Redshifts determined from the C IV $\lambda_{\rm peak}$ values given in Dix et al. (2023, submitted).

[c]Acquired from HW10 and/or from P. Hewett, priv. comm.

[d]Acquired from Lyke et al. (2020)

Note. — Complete table of 154 sources appears in the electronic version.

Finally, two additional sources, SDSS J073132.18+461347.0, and SDSS J141617.38+264906.1, were excluded due to the inability to measure the C IV line reliably (see Dix et al., 2022 in prep.). The result of this selection process is a calibration sample of 154 objects, presented in Table 3.5, which is a representative sample of optically selected quasars (see Section 5.2.2) used to derive prescriptions for correcting UV-based redshifts through linear regression analysis.

The redshift corrections are performed on redshifts obtained from three separate techniques: 1) measurements of the observed-frame wavelength of the peak of the

C IV emission line, 2) HW10 redshifts (P. Hewett, priv. comm.), and 3) SDSS Pipeline redshifts [17, Table D1, column 29 "Z_PIPE"]. The HW10 redshifts are notable as they already have a primary redshift correction applied.

The principal metric under investigation in this work is the initial velocity offset (Δv_i) between each of the aforementioned three UV-based redshifts (z_{meas}) and the $z_{\rm sys}$ value of a source determined from its [O III] λ5007 emission line by measuring the line peak in each spectra, which is presented in Table 3.2. This offset is computed using the following equation (see D20):

$$\Delta v_i = c\left(\frac{z_{meas} - z_{sys}}{1 + z_{sys}}\right). \tag{3.1}$$

These initial velocity offset values are presented in Table 3.5 and are shown in the top panels of Figure 3.4.

As shown in Table 3.5, there are three sources, SDSS J085344.17+354104.5, SDSS J090247.57+304120.7 and SDSS J111119.10+133603.8, where the SDSS Pipeline fails to produce reliable redshifts, resulting in either no produced redshift for the first of these, or unrealistically high velocity offsets of $|\Delta v_i| > 16000$ km s^{-1} for the latter two, while the velocity offsets for these two sources from the C IV and HW10 methods yield values that are only -170 and $+70$ km s^{-1}, and -910 and $+580$ km s^{-1}, respectively. As a result, these three sources are excluded from the SDSS Pipeline analysis, but are retained in the C IV and HW10 analyses.

The regression analysis follows the methods used by M17 and D20, where the correction to the velocity offset depends on the C IV emission-line properties and UV continuum luminosity such that:

$$\begin{aligned}\Delta v_{\rm corr}\ (\mathrm{km\ s^{-1}}) = {} & \alpha \log_{10}\mathrm{FWHM}_{CIV}\ (\mathrm{km\ s^{-1}}) \\ & + \beta \log_{10}\mathrm{EW}_{CIV}\ (\text{Å}) \\ & + \gamma \log_{10} L_{1350}\ (10^{-17}\mathrm{erg\ s^{-1}\,Å^{-1}})\end{aligned} \tag{3.2}$$

where $\Delta v_{\rm corr}$ is the velocity offset we subtract from the initial velocity offset calculated using Equation 3.1. The final, post-correction velocity offset, $\Delta v_f = \Delta v_i - \Delta v_{\rm corr}$, is displayed in the bottom panels of Figure 3.4. Since we fit the observed values of Δv_i to the model shown in Equation 3.2 and solved for the best fit coefficients, then, by definition, the mean (μ) of $\Delta v_i - \Delta v_{corr}$ is zero. This $\Delta v_{\rm corr}$ value is used to obtain a revised $z_{\rm sys}$ prediction by adjusting the initially measured redshift of a quasar. From Equation 3.1, solving for $z_{\rm meas}$, and substituting $z_{\rm meas} = z_{\rm sys}$ and $v_{\rm corr} = v_i$, we get

$$z_{rev} = z_{meas} + \frac{\Delta v_{corr}(1 + z_{meas})}{c} \tag{3.3}$$

where z_{rev} is the revised, more accurate, and more precise redshift.

Starting with our 154-object calibration sample, we run linear regressions using the three parameters defined in Equation 3.2. The results of this linear regression analysis provide the Δv_{corr} values from Equation 3.2 that are subtracted from the initial velocity offsets of the objects (from Table 3.5).

Distributions of the Δv_i and Δv_f values are plotted in the top and bottom panels in Figure 3.4, respectively. We see that the C IV-based Δv_i values are skewed toward negative values (blueshift) with a mean velocity offset of $\mu = -1034$ km s^{-1}, and a standard deviation of $\sigma = 1173$ km s^{-1}. The SDSS Pipeline-based Δv_i values have a considerably smaller negative initial velocity offset of $\mu = -564$ km s^{-1}, yet a larger standard deviation of $\sigma = 1268$ km s^{-1}. As expected, the HW10-based Δv_i values show a mean initial velocity offset much closer to zero ($\mu = 54$ km s^{-1}), however the standard deviation is only slightly smaller than that of the C IV-based Δv_i values ($\sigma = 1038$ km s^{-1}). Despite the improvements demonstrated by the HW10-based values, we are able to use our regression analysis to improve on UV-based redshift determinations further, as shown below.

Our redshift corrections yield mean Δv_f values of zero km s^{-1} using all three UV-based methods (see the bottom panels of Figure 3.4). The standard deviation of the Δv_f values, on the other hand are reduced by $\sim 17\%$, $\sim 3\%$, and $\sim 5\%$ for the C IV, HW10, and SDSS Pipeline methods, respectively, with respect to the measured Δv_i values.

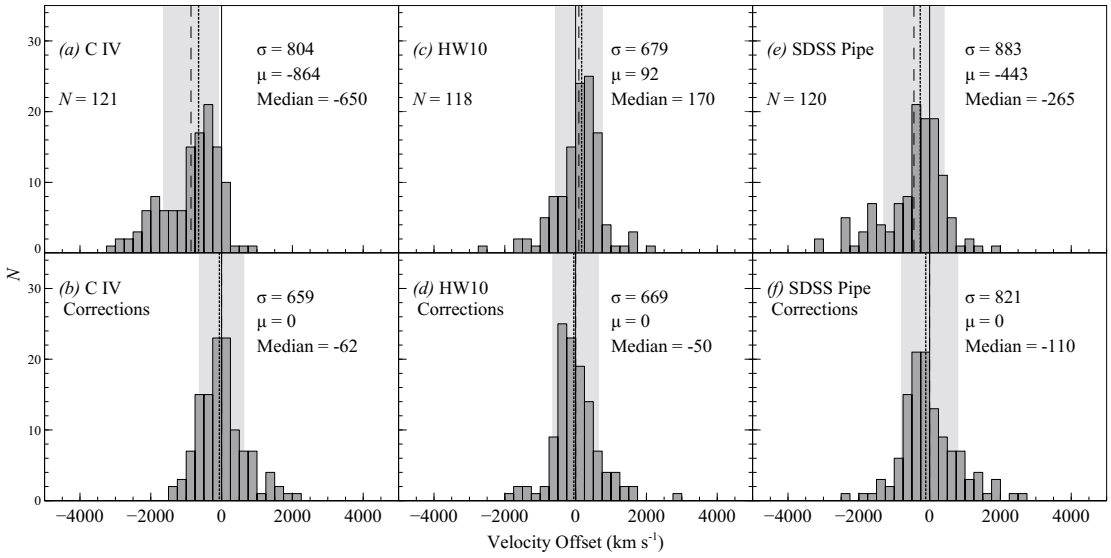

Figure 3.4 Velocity offsets relative to $z_{\rm sys}$ before (panels *a*, *c*, and *e*) and after (panels *b*, *d*, and *f*) the corrections using the linear regression coefficients given in Table 3.6. The standard deviation (shaded region), mean (dashed line), median (dotted line), and zero velocity offset (solid line) are marked in each panel. SDSS J090247.57+304120.7 and SDSS J111119.10+133603.8 do not appear on the SDSS Pipe panels because of their unreliable redshifts, and SDSS J085344.17+354104.5 does not appear as it lacks an SDSS Pipeline redshift.

The median velocity offsets are also reduced for all three methods. The linear regression coefficients (Equation 3.2) used to achieve these corrections are presented in Table 3.6. Table 3.6 also gives the *t*-Value for confidence statistics in determining the importance of each parameter (see also D20), where *t*-Values of $|t| \gtrsim 2$ denote a strong correlation, with decreasing confidence as $t \rightarrow 0$.

Residuals of the 154 source sample both before and after our corrections are applied are presented in Figure 3.5. The residual distributions show the substantial reduction in the velocity offsets before and after each correction. The corrected velocity offsets for both the C IV and HW10-based methods are closer to zero than the corrected velocity offsets for the SDSS Pipeline method.

Table 3.6. Linear Regression Coefficients

UV-Based Redshift Method	Sample Size	Regression Coefficients	Value	Error	t-Value
C IV	154	α	-3268	537	-6.08
		β	1356	356	3.80
		γ	196	47	4.18
HW10	149	α	-1043	592	-1.76
		β	385	298	1.95
		γ	61	51	1.20
SDSS Pipe	151	α	-1696	661	-2.57
		β	452	461	3.17
		γ	79	57	1.37

The improvement in the mean offset (μ), and the standard deviation (σ), achieved for the HW10 method is related to the fact that our analysis is a second-order correction to the one employed by HW10. The C IV-based redshifts provide a smaller standard deviation than the HW10-based method when corrected using our regression analysis (see Figure 3.4). Finally, the SDSS Pipeline-based redshifts provide the least reliable results; in particular, we find that the SDSS Pipeline fails to produce meaningful redshifts for three out of 154 sources in our calibration sample. Furthermore, DR16 redshifts [82, Table D1, column 10 "Z_QN"] available for 129 sources from our sample provide significantly larger standard deviations than the SDSS Pipeline values both before and after the correction.

For our calibration sample of quasars, the maximum Δv_i value is -8910 km s^{-1} obtained from a C IV-based redshift, along with several sources having velocity offsets within the -4000 km s^{-1} $< \Delta v_i < -2000$ km s^{-1} range. Values of this magnitude, while high, are not unexpected due to the kinematics associated with luminous, rapidly accreting quasars that can directly affect the C IV emission line and cause large blueshifts [e.g., 95, 150, 141].

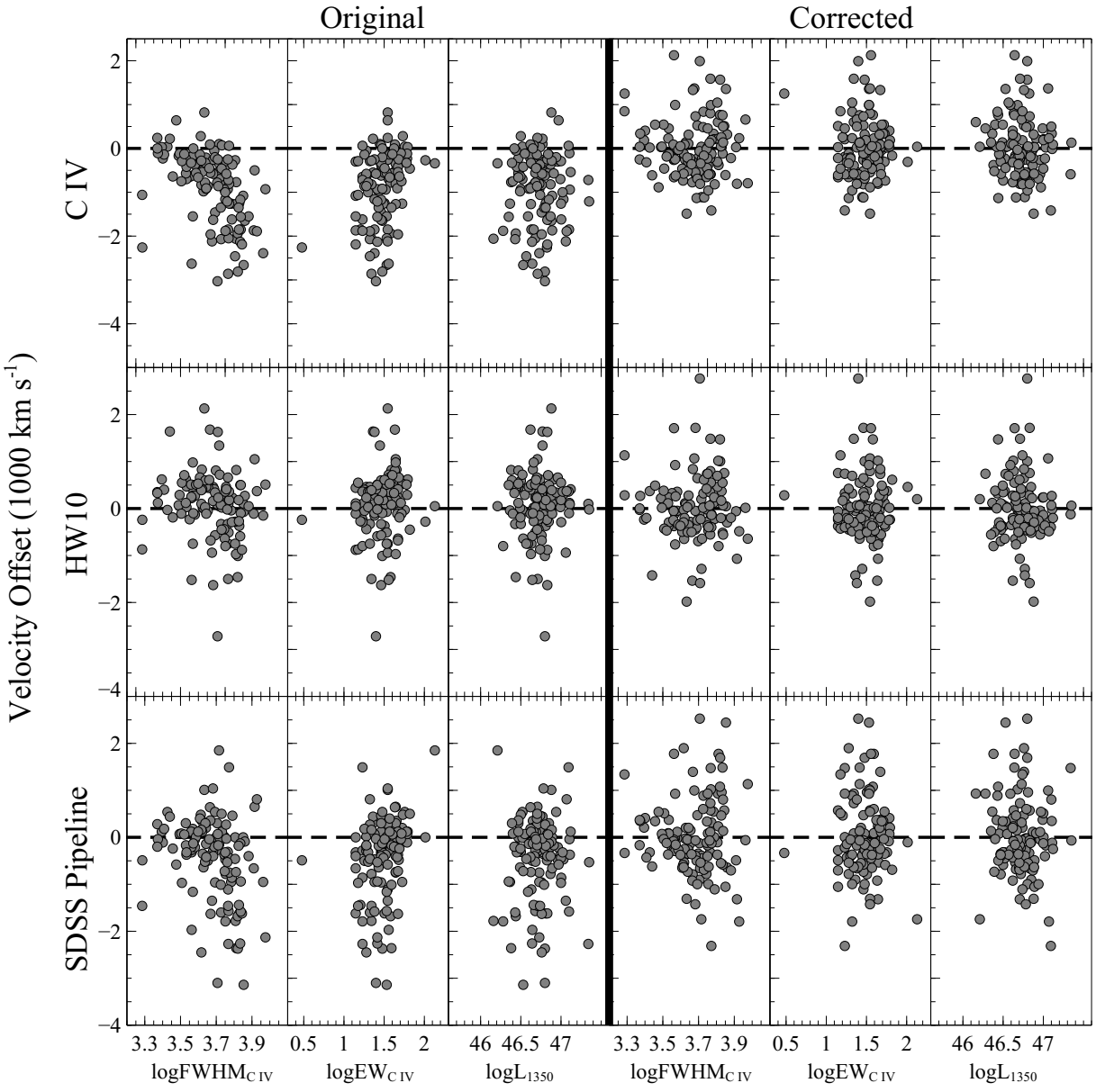

Figure 3.5 Residual velocity offsets with respect to z_{sys} before (three leftmost columns), and after (three rightmost columns), corrections are applied (see Equation 3.2) against our regression parameters. The outliers discussed in Section 5.2 do not appear in this plot.

Nevertheless, our method tends to correct even these large velocity offsets to more reasonable values as shown in Figures 3.4 and 3.6.

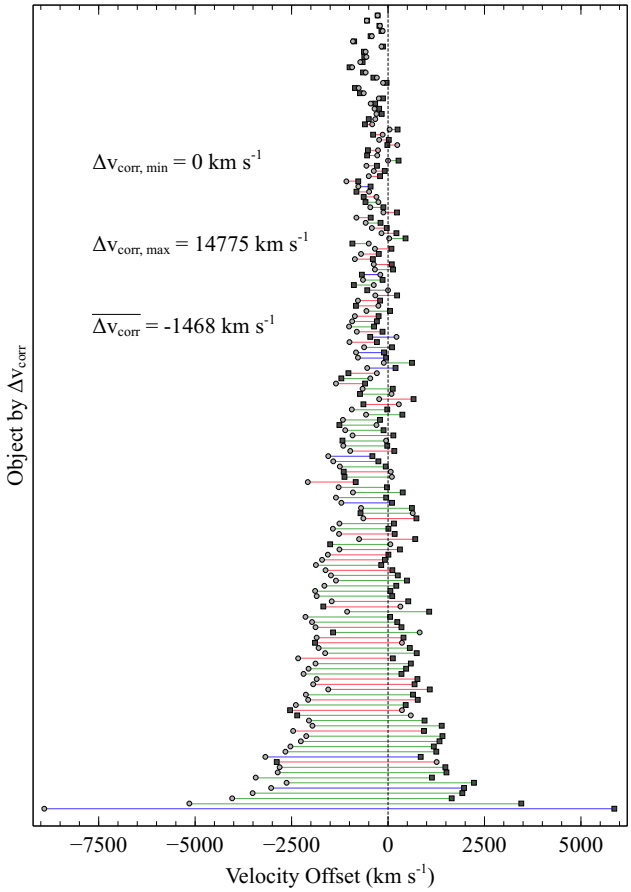

Figure 3.6 Initial velocity offsets (Δv_i; circles) compared to final velocity offsets (Δv_f; squares) for C IV-based redshifts of the calibration sample of 154 sources. The lines connecting the initial and final velocity offsets are sorted from top to bottom by the absolute value of the velocity offset correction ($|\Delta v_{corr}|$), where the lines are color coded with respect to the monochromatic luminosity at rest-frame 5100 Å as such: $46.08 < \log(L_{5100}) < 46.41$, $46.42 < \log(L_{5100}) < 46.74$, and $46.75 < \log(L_{5100}) < 47.09$ are marked in red, green, and blue, respectively. While the majority of the Δv_i values, which are blueshifts, produce Δv_f values with the opposite sign, we also see Δv_i values which are redshifts that end up as blueshifts; however the overall effect of our regression analysis brings Δv_f values closer to zero. We find no trend between $|\Delta v_{corr}|$ and the monochromatic luminosity at rest-frame 5100 Å.

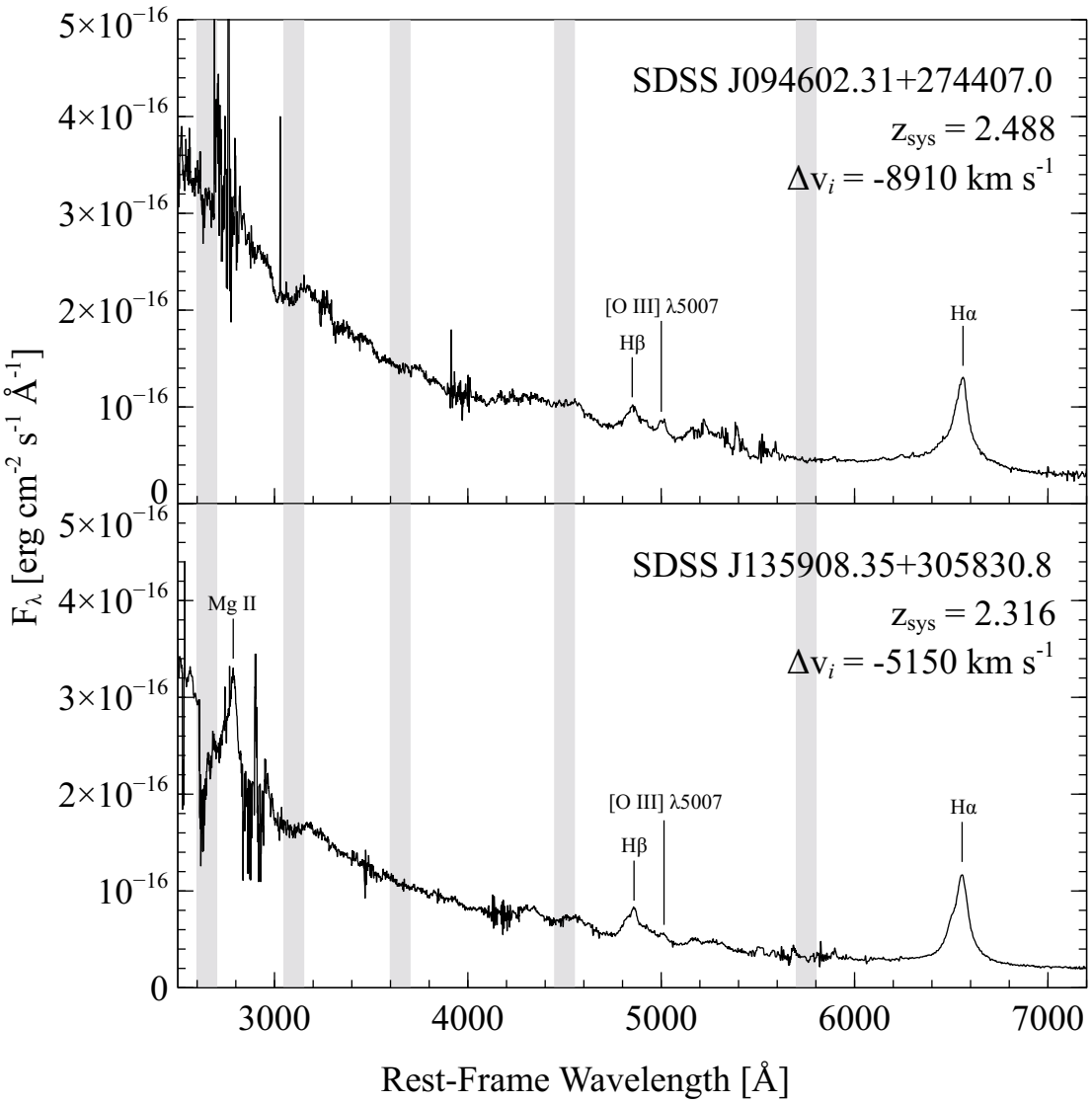

Figure 3.7 GNIRS-DQS spectra of SDSS J094602.31+274407.0 (top) and SDSS J135908.35+305830.8 (bottom). These two objects display the largest velocity offsets (C IV vs. [O III]) in the 154 object calibration sample, with $\Delta v_i = -8910$ and $\Delta v_i = -5150$, respectively. For the GNIRS-DQS sample, we elected to fit Gaussians to residual spectral features after subtracting a localized linear continuum and a convolved Fe II template (see M21 for further discussion).

The results of our regression analysis, presented in Table 3.6, provide considerably improved redshifts over the regression coefficients used by D20. When we employ the D20 regression coefficients on our calibration sample of 154 sources, we obtain standard

deviations on the distributions of Δv_f which are $\sim 8\%$ larger for the HW10 method, $\sim 31\%$ larger for the SDSS Pipeline method, and $\sim 2\%$ larger for the C IV-based redshifts than when using the coefficients from Table 3.6.

In summary, considering the four basic observables associated with the C IV emission line, one can derive the most accurate and precise prediction of the systemic redshift of a quasar.

3.3.1. Redshift and Luminosity Dependence

Typically, redshifts are determined either spectroscopically or photometrically from multiple features (i.e., HW10 and the SDSS Pipeline). When some of these features are no longer available in the spectra, our ability to determine the redshift is affected, and it is plausible that the initial velocity offsets depend also on source redshift. We search for such a dependence in our data by splitting our calibration sample into three redshift bins: $1.55 \lesssim z \lesssim 1.65$ (Bin 1), $2.10 \lesssim z \lesssim 2.40$ (Bin 2), and $3.20 \lesssim z \lesssim 3.50$ (Bin 3), which contain 43, 90, and 21 sources, respectively. These intervals ensure coverage of the [O III] $\lambda 5007$ emission line in the J, H, or K bands (see Section 5.2.2).

We perform the regression analysis as described in Section 5.2 on each redshift bin. The results are presented in Table 3.7, and shown in Figure 3.8. The standard deviation (σ) of the velocity offsets has been reduced by factors of up to $\sim 32\%$ across all redshift bins compared with the respective standard deviations for the bulk sample. For the C IV-based method, the smallest improvement is in Bin 1 ($\sim 2\%$), compared to improvements of $\sim 22\%$ in Bin 2 and $\sim 32\%$ in Bin 3. This trend appears to follow the increase in the average Δv_i in each of those bins ($\mu = -703$ km s^{-1}, $\mu = -1161$ km s^{-1}, and $\mu = -1171$ km s^{-1}, respectively). Although the statistics in Bin 3 are limited, this trend may follow from the fact that the highest redshift bin tends to have higher luminosity quasars, which results in larger C IV blueshifts (e.g., due to outflows or winds) on average for more distant sources [e.g., 120]. Since our regression analysis relies a lot on the C IV parameter space, it is not unexpected that our corrections to the C IV-based redshifts would be more important for the more powerful sources found preferentially at higher redshifts.

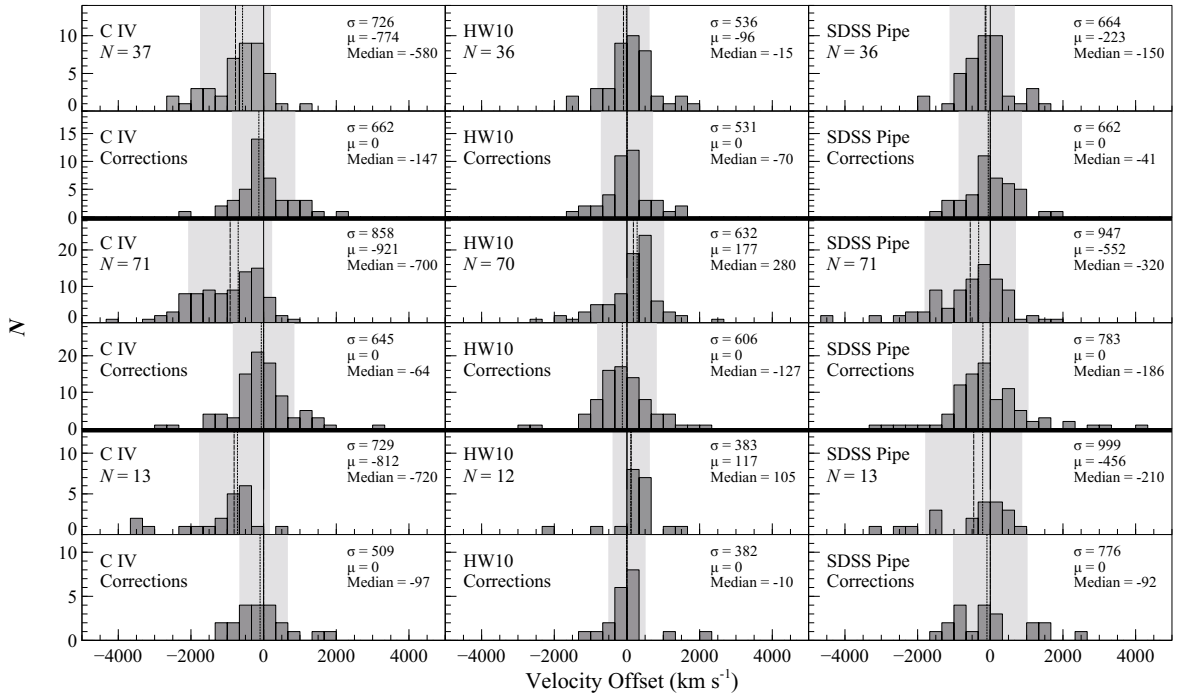

Figure 3.8 Same as Figure 3.4, but split into three redshift bins. Top six panels, middle six panels, and bottom six panels correspond to redshift Bin 1, Bin 2, and Bin 3, respectively, as described in the text.

It is therefore imperative to obtain rest-frame UV-optical spectra of as many quasars at the highest possible redshifts for this type of analysis.

Concerning the HW10-based method, our corrections produce improvements in standard deviation ranging from $\sim$ 2% to $\sim$ 10%, with no apparent trend with redshift. Therefore, it seems that these improvements are not very sensitive to the coverage of the Mg II line, which is absent from Bin 3. This result may be indicative of the overall robustness of the HW10 method, as found from the entire sample (see Section 5.2 and Figure 3.4). Mild improvements, and no significant redshift dependence, are observed for the SDSS Pipeline method, and the overall standard deviations of velocity offset distributions stemming from this method remain high (> 1000 km s^{-1}) in Bins 2 and 3.

Table 3.7. Linear Regression Coefficients for Each Redshift Bin

UV-Based Redshift Method	Redshift Bin[a]	Regression Coefficients	Value	Error	*t*-Value	Number of Sources
		α	-545	809	-0.67	
	1	β	611	475	1.29	43
		γ	9	66	0.13	
		α	-3976	758	-5.24	
C IV	2	β	1726	527	3.27	90
		γ	239	67	3.54	
		α	-5439	1474	-3.69	
	3	β	47	1078	0.04	21
		γ	239	138	2.95	
		α	494	710	0.81	
	1	β	-606	371	-1.55	42
		γ	-22	54	-0.39	
		α	-1831	942	-2.11	
HW10	2	β	1680	558	2.90	87
		γ	92	80	1.23	
		α	1721	1424	1.01	
	3	β	946	1100	0.86	20
		γ	-137	144	-1.10	
		α	108	741	0.15	
	1	β	-166	431	-0.38	42
		γ	-6	60	-0.11	
		α	-2310	959	-2.41	
SDSS Pipe	2	β	1943	668	2.91	89
		γ	108	85	1.27	
		α	2086	2114	0.99	
	3	β	2459	1520	1.62	20
		γ	-250	197	-1.27	

[a]Bins 1, 2, and 3 correspond to redshift ranges of $1.55 \lesssim z \lesssim 1.65$, $2.10 \lesssim z \lesssim 2.40$, and $3.20 \lesssim z \lesssim 3.50$.

In general, the greatest limitation in our ability to search for a redshift dependence is the disparity in the number of sources in each bin. Predictably, Bin 2 yields results that are closer to those obtained for the entire sample, as $\sim 58\%$ of that sample is contained within that bin. A significantly larger sample size, particularly in Bin 3 ($z \sim 3$), may allow for a more definitive conclusion in this matter. This highest redshift bin is particularly important given the absence of the Mg II lines from the optical spectrum, and the need to reliably estimate redshifts of more distant sources.

In addition to exploring a possible redshift dependence, we also look to see if our ability to predict a quasar's $z_{\rm sys}$ value depends on source luminosity. We trisect the calibration sample into three equal L_{5100} bins: $46.08-46.41$, $46.42-46.74$, and $46.75-47.09$, and look for any significant statistical deviations with respect to the entire sample. The results are shown in Figure 3.6. We see that there appears to be no clear dependence on source luminosity. A possible explanation for this result is that our sample is flux limited, and therefore it is difficult to disentangle the strong redshift-luminosity dependence.

3.4. Summary and Conclusions

We present an augmented catalog of spectroscopic properties obtained from NIR observations of a uniform, flux-limited sample of 260 SDSS quasars at $1.55 \lesssim z \lesssim 3.50$. This catalog includes basic spectral properties of rest-frame optical emission lines, chiefly the Mg II, Hβ, [O III], Fe II, and Hα lines, depending on the availability of the line in the spectrum. These measurements provide an enhancement to the existing GNIRS-DQS database enabling one to more accurately analyze and investigate rest-frame UV-optical spectral properties for high-redshift, high-luminosity quasars in a manner consistent with studies of low-redshift quasars.

We also present prescriptions for correcting UV-based redshifts based on a subset of the GNIRS-DQS sample of 154 objects that are non-BAL, non-RL, have accurate C IV measurements, and have $z_{\rm sys}$ values obtained from [O III] measurements. We provide measurements of velocity offsets using three different UV-based methods compared to $z_{\rm sys}$ values. This 154 object sample is three times the size of the calibration sample used

in D20, and is both a higher quality and more uniform dataset than M17 and D20.

We attempt to correct for these velocity offsets using a linear regression based on UV continuum luminosity and C IV emission-line properties. Using this approach, we can decrease the standard deviation of the distribution of velocity offsets in our calibration sample by $\sim$ 3% with respect to the best available UV-based redshift method, and by $\sim$ 17% using C IV-based redshifts. The SDSS Pipeline provides the least precise UV-based redshifts, as the standard deviation on the velocity offsets is larger by $\sim$ 20% compared with the other two methods both before and after the correction. We find that the simplest, most reliable way to obtain an accurate and precise $z_{\rm sys}$ value is using the C IV parameter space alone via four basic observables associated with the C IV emission line, and applying the following methodology:

(1) Measure the observed peak wavelength, EW, and FWHM of C IV, and the monochromatic luminosity at 1350 Å (L_{1350}).
(2) Calculate an initial redshift measurement, $z_{\rm meas}$, with the observed peak wavelength of C IV.
(3) Use Equation 3.2 and the coefficients in Table 3.6 to calculate $\Delta v_{\rm corr}$.
(4) Use Equation 3.3 with the observed $z_{\rm meas}$ and calculated $\Delta v_{\rm corr}$ to obtain a revised, more accurate, and more precise redshift measurement.

Additionally, we explore whether our prescriptions depend on 1) velocity width measurement, of which we determine there is no overt discrepancy based on methodology, 2) source redshift, where we determine that additional data are needed, particularly at the highest redshifts under investigation, in order to obtain more robust results, and 3) source luminosity, where no clear trends are apparent, consistent with the flux-limited nature of our sample.

A primary interest going forward would be bolstering the sample with supplementary observations of quasars, primarily at $z \sim 3$, in order to obtain statistically meaningful results on a potential redshift dependence, and further improve UV-based redshift determinations. Another avenue of further investigation includes increasing the sample size

of quasars with significantly higher spectral resolution, e.g., using Gemini's Spectrograph and Camera for Observations of Rapid Phenomena in the Infrared and Optical [SCORPIO; 126], in order to further improve the UV-based redshift corrections by obtaining more accurate line peaks of spectral features. Machine learning can also play an important role as larger data sets will be produced that require redshift correction *en masse*. By utilizing the entire quasar UV spectrum, as opposed to a few key parameters, it will be possible to test if machine learning algorithms can produce more reliable estimates of $z_{\rm sys}$ much more efficiently than our prescriptions allow.

As future projects begin to produce data, we can expect that $\approx 10^6$ high-redshift ($z \gtrsim 0.8$) quasars will have redshifts determined through large spectroscopic surveys conducted in the rest-frame UV-optical regime from instruments such as the Dark Energy Spectroscopic Instrument [DESI; 79, 33], the 4m Multi-Object Spectroscopic Telescope [31], and the Subaru Prime Focus Spectrograph [PFS, 151]. For those quasars at $1.5 \lesssim z \lesssim 5.0$, coverage of the C IV emission line will enable crucial redshift corrections, as has been demonstrated in this work. Instruments such as the James Webb Space Telescope [JWST, 47] can provide simultaneous coverage of C IV, Mg II, and [O III] for $6 \lesssim z \lesssim 9$, allowing for similar investigations of redshift dependencies and corrections for the most distant known quasars.

This work is supported by National Science Foundation grants AST-1815281 (B. M. M., C. D., O. S.) and AST-1815645 (M. S. B., A. D. M.). W.N.B. acknowledges support from NSF grant AST-2106990. This work was enabled by observations made from the Gemini North telescope, located within the Maunakea Science Reserve and adjacent to the summit of Maunakea. We are grateful for the privilege of observing the Universe from a place that is unique in both its astronomical quality and its cultural significance. This research has made use of the NASA/IPAC Extragalactic Database (NED), which is operated by the Jet Propulsion Laboratory, California Institute of Technology, under contract with the National Aeronautics and Space Administration. We thank Paul Hewett for helpful contributions of redshift data.

3.5. Appendix: Comparing Different Velocity Widths of the C IV Line

In our regression analysis, we have elected to use the FWHM of the C IV line. However, there has been some debate in the literature concerning the overall reliability of using FWHM as the quantification of the velocity width of an emission line [e.g., 109, 29]. While M17 and D20 used FWHM for their analyses, other methods for measuring velocity widths of emission-line profiles include Line Dispersion (σ) and Mean Absolute Deviation (MAD) [e.g., 32, 29]. We therefore repeated our analysis by replacing FWHM with each of these two velocity width methods, measured from the Gaussian fits presented in Table 3.4, and compared the results obtained from all three velocity widths. We find that replacing FWHM with σ or MAD gave no notable improvement in the dispersion on the relevant corrections, as shown in Figure 3.9. We thus have elected to adopt the FWHM parameterization throughout this work.

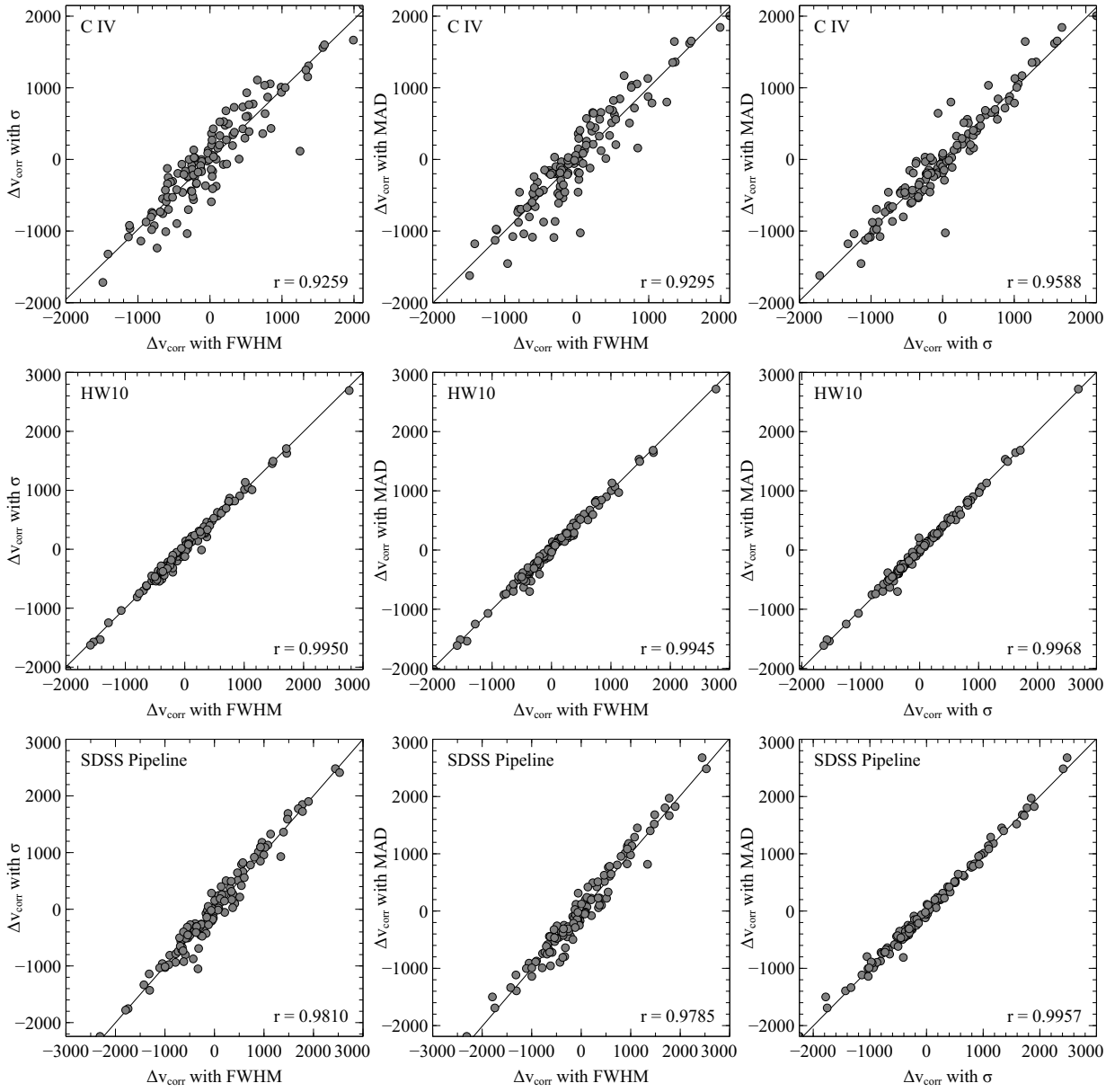

Figure 3.9 Comparison of the velocity offsets produced using C IV FWHM, σ, and MAD for each UV-based redshift method. Each panel displays the correlation between the corrected velocity offset values produced by our regression analysis when using either FWHM, σ, or MAD, along with a corresponding Pearson linear correlation coefficient r, where $r \rightarrow 1$ corresponds to a strong correlation. No significant difference exists in this regression analysis between the three different parameters.

CHAPTER 4

GEMINI NEAR INFRARED SPECTROGRAPH - DISTANT QUASAR SURVEY: PRESCRIPTIONS FOR CALIBRATING UV-BASED ESTIMATES OF SUPERMASSIVE BLACK HOLE MASSES IN HIGH-REDSHIFT QUASARS

4.1. Introduction

A persisting point of interest in astrophysics today is understanding the co-evolution of supermassive black holes (SMBHs) and their host galaxies through cosmic time [e.g., 62, 34, 20, 24, 26, 149]. A fundamental ingredient in this research area is the SMBH mass ($M_{\rm BH}$). Over the past four decades, several methods have been employed for obtaining $M_{\rm BH}$ values in galaxies [such as stellar kinematics, masers, interferometry and spectrophotometric monitoring campaigns of active galaxies, e.g., 43, 49, 53, 54, 139, 55, 52]. Overall, the masses obtained from these methods are consistent with each other but deriving $M_{\rm BH}$ values in active galactic nuclei (AGN) have the best prospects of obtaining the SMBH mass function through cosmic time given the large luminosities of such sources and their mass observable indicators at all accessible redshifts [e.g., 73, 143, 153].

The $M_{\rm BH}$ values for AGN, or quasars, are usually determined through measurements of broad emission lines in the optical band. Specifically, following the virial assumption [see, 114], we use measurements of the size of the broad emission line region (BELR), $R_{\rm BELR}$, and the velocity width of an emission line stemming from the BELR, ΔV, in order to estimate $M_{\rm BH}$ for AGN. Of these terms, estimating the value of $R_{\rm BELR}$ becomes the most pertinent for reliable estimates of $M_{\rm BH}$.

Ideally, measurements of $R_{\rm BELR}$ are derived from reverberation mapping (RM) of AGN or quasars, which uses time lags between continuum fluctuations and photoionized BELR emission line fluctuations to determine the size of the BELR [e.g., 16, 111, 105]. To date, $M_{\rm BH}$ has been measured successfully using RM campaigns for $\approx$ 150 quasars primarily with the Hβ λ4861 emission line [e.g., 7, 13, 56, 6, 155]. One of the most important findings from these RM campaigns is the BELR size-luminosity ($R-L$) relation,

where $R_{\rm BELR} \propto L^{\alpha}$ with $\alpha \sim 0.5$, in agreement with expectations from photoionization theory [e.g., 76, 70, 69, 14, 12].

Since RM campaigns are currently impractical for $M_{\rm BH}$ measurements in $\approx 10^6$ of known quasars [e.g., 139], [160] have proposed that the $R - L$ relation, in conjuction with the virial assumption, allows one to *estimate* single epoch (SE) $M_{\rm BH}$ values by substituting the continuum luminosity for $R_{\rm BELR}$. Estimates of $M_{\rm BH}$ values for $\approx 10^5$ quasars have been obtained in this fashion during the past two decades [e.g., 144, 118].

Nevertheless, estimating $M_{\rm BH}$ values using the SE method faces additional challenges, particularly at high redshift. First, the most reliable SE indicator for $M_{\rm BH}$ is obtained from spectroscopic measurements of low-ionization emission lines such as the Hβ line, and at $z \gtrsim 1$, this line is shifted into the less accessible near-infrared (NIR) band. Second, recent Super-Eddington Accreting Massive Black Hole (SEAMBH) and Sloan Digital Sky Survey-RM campaigns discovered many highly accreting objects that lie below the $R - L$ relation [e.g., 44], suggesting that an additional correction to account for accretion rate is warranted for SE $M_{\rm BH}$ estimates.

To overcome the first of these, SE $M_{\rm BH}$ estimates using other prominent emission lines have been calibrated against Hβ-based $M_{\rm BH}$ estimates in the nearby universe. The two most common emission lines that are used for such calibrations are Mg II $\lambda\lambda 2798, 2803$ [e.g., 158, 174, 164, 77] and C IV $\lambda 1549$ [e.g., 160, 3, 21, 109, 27, 29]. However, these emission lines have yielded relatively fewer successful $M_{\rm BH}$ measurements through RM campaigns [e.g., 22, 140, 80, 55, 60], and each of these line profiles contains its own intrinsic measurement challenges [e.g. 159, 9]. To address the second challenge, [39] have proposed to include a correction to the $R - L$ relationship based on the Fe II emission blend flanking the Hβ emission line, which is known to be an accretion-rate indicator. Recently, [84] implemented such a correction and found that $M_{\rm BH}$ estimates in highly accreting sources are overestimated.

In this work, we utilize a large spectroscopic inventory for high-redshift quasars that allows us to obtain the most reliable $M_{\rm BH}$ estimates using rest-frame ultraviolet (UV)

emission lines. Our inventory includes high quality measurements of the Hβ, Fe II, Mg II, and C IV emission lines, which allows us to implement two separate accretion-rate based corrections to the estimated $M_{\rm BH}$ value while investigating the effects of using different BELR velocity width measurements.

This paper is organized as follows. In Section 5.2.2, we describe our sample and data analysis. In Section 4.3, we present the results of multiple regression analyses used for obtaining prescriptions for reliable $M_{\rm BH}$ estimates at high redshift. In Section 4.4 we discuss our results and in Section 5.4 we present our conclusions. Throughout this paper, we compute luminosity distances using $H_0 = 70$ km s^{-1} Mpc^{-1}, $\Omega_{\rm M} = 0.3$, and $\Omega_\Lambda = 0.7$ [e.g., 148].

4.2. Sample Selection and Measurements

Our sample is drawn from the Gemini Near Infrared Spectrograph - Distant Quasar Survey (GNIRS-DQS; Matthews et al. 2022, hereafter M22). These quasars were selected from all the Sloan Digital Sky Survey [SDSS; 169] quasars [82] having $m_i \sim 19.0$ that lie in the redshift intervals $1.55 \lesssim z \lesssim 1.65$, $2.10 \lesssim z \lesssim 2.40$, and $3.20 \lesssim z \lesssim 3.50$; these redshift intervals assure that the Hβ spectral region is covered in either the J, H, or K bands.

From all 260 GNIRS-DQS sources, we were able to reliably measure C IV emission-line profiles for 177 sources from their respective SDSS spectra. Specifically, the C IV emission line is difficult to measure reliably in broad absorption line (BAL) quasars due to BAL troughs impacting the emission-line profile. Therefore, all 65 BAL quasars from the GNIRS-DQS sample were removed during our C IV-based $M_{\rm BH}$ estimate analysis. Since our analysis involves measurements of the rest-frame equivalent width (EW) of the C IV emission line, we further removed 16 radio-loud quasars (RLQs)[1] from the sample. This was done in order to avoid potential dilution of the C IV emission line by continuum emission originating in the radio jets. We note that one of the BAL quasars we removed, SDSS J114705.24+083900.6, is also radio loud. Finally, we removed two sources,

[1]We define radio loud quasars as sources having radio-loudness values of $R > 100$ [where R is the ratio of the flux densities at 5 GHz and 4400 Å ; 71]

SDSS J073132.18+461347.0 and SDSS J141617.38+264906.1, for which we were unable to measure the C IV emission line reliably from their SDSS spectra due to a poor signal-to-noise ratio (S/N). The remaining sample of 177 non-BAL, non-RL sources with reliable C IV measurements was used in the C IV-based $M_{\rm BH}$ estimate analysis below.

The GNIRS spectra provide reliable Mg II measurements for 99 of the GNIRS-DQS sources (see, M22): only 70 of these sources also have reliable C IV measurements following the removal of 22 BAL quasars and seven RLQs. From these 99 quasars, 65 (47 with reliable C IV measurements) lie in the redshift range of $2.10 \lesssim z \lesssim 2.40$, and 34 (23 with reliable C IV measurements) lie at $3.20 \lesssim z \lesssim 3.50$. In both of these redshift ranges Mg II and Hβ are covered in the same spectrum, however, in the latter range Mg II has the highest S/N [see below, and cf. 174].

Furthermore, we were able to reliably measure the Mg II profile in the SDSS spectra that adequately covered that emission line in 179 of the GNIRS-DQS sources: 34 and 13 of these sources do not have reliable C IV measurements given that these are BAL quasars and RLQs, respectively. From this sample of 179 quasars, 53 sources had a measurable Mg II profile in both the SDSS and the GNIRS-DQS spectra. When combining all available Mg II measurements, either from SDSS or GNIRS-DQS or both, we compiled a total sample of 225 sources: 47, 16, and 2 of these sources do not have reliable C IV measurements given that these are BAL quasars, RLQs, or sources with unreliable C IV measurements, respectively.

4.2.1. Fitting the SDSS Spectra

The SDSS spectra of the sources were fit utilizing a local linear continuum and two Gaussians for each broad emission line. We find that fitting two Gaussians to each of the C IV and Mg II emission lines is sufficient given the S/N of ~ 40 across both the SDSS and GNIRS spectra. The Fe II and Fe III emission complex that blends with the Mg II emission line was modeled with the empirical template of [159]. This template was broadened with a Gaussian kernel having a full width at half maximum (FWHM) intensity that was free to vary up to 10000 km s^{-1} and was determined based on a least squares analysis of each

fitted region.

The Gaussians were constrained such that the flux density would lie between 0 and twice the value of the peak of the respective emission line and the FWHM was restricted to lie within 0 and 15000 km s^{-1}. The peaks of these Gaussians were also constrained to lie within ±1500 km s^{-1} of the rest-frame wavelength of the peak of the emission line based on the systemic redshift from M22. After the initial fitting was performed for each region, we visually inspected the fit to see if more lenient constraints with interactive fitting were warranted.

Spectral properties stemming from these fits are reported in Table 4.1 for C IV and Mg II. In this Table, Column (1) reports the source's SDSS designation. Columns (2), (3), (4), (5), and (6) list the FWHM, mean absolute deviation (MAD; described below), line dispersion ($\sigma_{\rm line}$), EW, and the observed-frame wavelength of the emission-line peak, $\lambda_{\rm peak}$, respectively, for C IV. Columns (7), (8), (9), (10), and (11) list the same spectral properties for the Mg II emission line.

4.2.2. Measurements and Error

For each emission-line profile in either the GNIRS or SDSS spectra, we measured the values of the $\sigma_{\rm line}$ and MAD. The line dispersion is defined by

$$\sigma_{\rm line} = \left[\frac{\int (\lambda - \lambda_0)^2 P(\lambda) d\lambda}{\int P(\lambda) d\lambda} \right]^{1/2} \tag{4.1}$$

where λ_0 is the line centroid and $P(\lambda)$ is the emission-line profile. The MAD is defined as

$$\mathrm{MAD} = \int |\lambda - \lambda_{\rm med}| P(\lambda) d\lambda \Big/ \int P(\lambda) d\lambda \ , \tag{4.2}$$

where $\lambda_{\rm med}$ is the median wavelength of the emission-line profile, first suggested in [32] as

an appropriate representation for the emission-line width. For each emission-line profile in the GNIRS spectra, we obtained the FWHM, EW, and observed-frame wavelength of the peak emission from M22.

We present three different values for the velocity widths (FWHM, MAD, $\sigma_{\rm line}$) due to the uncertainties inherent in the accuracy of FWHM, the most popular of these parameters [see, 109, 29, 77]. While $\sigma_{\rm line}$ is a dependable measurement to describe the emission-line velocity width, [32] suggest that MAD provides an accurate estimate of this quantity for low-quality data. Overall, we recognize that the best virial velocity width indicator is debatable, therefore, we provide calibrations for the $M_{\rm BH}$ estimates utilizing all of these parameters.

We have also derived the monochromatic luminosities, L_{1350} and L_{3000}, by measuring the continuum flux densities, at rest-frame λ1350 Å and λ3000 Å , respectively, and employing our chosen cosmology. All the flux densities and monochromatic luminosities (L_{5100}) at rest-frame λ5100 Å used in this work were obtained from the M22 catalog. The flux calibration for the GNIRS-DQS data is extensively discussed in [90, hereafter M21]. In certain cases, the flux density at rest-frame wavelength 3000 Å was not measurable in the GNIRS-DQS spectrum due to this wavelength range falling outside of the J band. In these cases, the flux density was determined by extrapolating from the flux density at rest-frame wavelength 5100 Å using the canonical quasar optical-UV continuum of the form $f_\nu \propto \nu^{-0.5}$ [e.g., 156]. Similarly, there are SDSS spectra that do not have a reliable flux density value for the rest-frame wavelength 1350 Å due to low S/N at the blue end of the SDSS spectrum. In these cases, we employed the same model as described above extrapolating from the flux density at rest-frame 1450 Å.

The uncertainties for all emission line measurements reported in Table 1, were determined by following the methods described in M21 and M22. Briefly, we created mock spectra that introduced random Gaussian noise to the original spectra. We then fit these spectra as described above, and measured the newly fit profiles. This process was repeated 1000 times in order to obtain a distribution for each of our parameters, and the

68% range is reported as our measurement uncertainty.

4.3. UV-Based Black Hole Mass Calibration

4.3.1. Estimating Black Hole Masses

We obtain SE $M_{\rm BH}$ estimates for each emission line in this work by, first, following the virial assumption,

$$M_{\rm BH} = \frac{f R_{\rm BELR} \Delta V^2}{G}, \tag{4.3}$$

where G is the gravitational constant and f is the virial factor which depends on the geometry and orientation of the system and is assumed to be on the order of ≈ 1 [e.g., 58, 170]. Then, we substitute the continuum luminosity for $R_{\rm BELR}$ according to the $R - L$ relation (see, Section 5.1) as $R_{\rm BELR} \propto L^{0.5}$.

We estimate Hβ-based $M_{\rm BH}$ values by further correcting the $R_{\rm BELR}$ parameter in Equation 4.3 (hereafter, $R_{\rm H\beta}$) for the source accretion rate, based on the scaling relation presented in [39] in the following way

$$\log(R_{\rm H\beta}/{\rm lt-days}) = \delta + \beta \log \ell_{44} + \gamma \mathcal{R}_{\rm Fe} \tag{4.4}$$

where $\ell_{44} = L_{5100}/10^{44}$ erg s^{-1}, $\delta = 1.65 \pm 0.06$, $\beta = 0.45 \pm 0.03$, $\gamma = -0.35 \pm 0.08$, and $\mathcal{R}_{\rm Fe}$ is an indicator of the strength of the Fe II emission defined as the ratio of the flux (F) or EW between Fe II in the 4434-4684Å rest-frame band; [19] and Hβ; $\mathcal{R}_{\rm Fe} = F_{\rm FeII}/F_{\rm H\beta} \approx {\rm EW}_{\rm FeII}/{\rm EW}_{\rm H\beta}$. In this work we employ the ratio of EWs to determine $\mathcal{R}_{\rm Fe}$. For the virial factor in Equation 4.3, we adopt $f = 1.5$ and the FWHM as ΔV for Hβ-based $M_{\rm BH}$ values [84]. The value for the f factor introduces additional uncertainty, on the order of ~2-3 [e.g., 92], in our estimation of $M_{\rm BH}$. Our adopted value is consistent with [172] and the emipirical best fit value obtained from the $M - \sigma_\star$ correlation [e.g., 103, 58, 165].

[84] have shown that this accretion-rate correction is necessary for adjusting $M_{\rm BH}$ values that are overestimated by a factor of 2 for typical luminous high-redshift quasars.

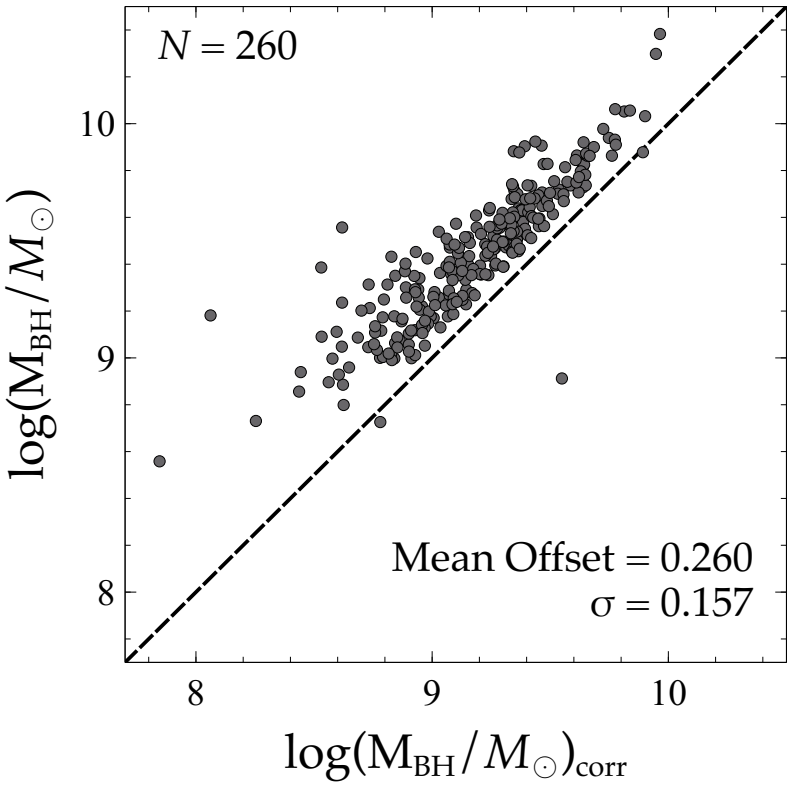

Figure 4.1 The Hβ-based $M_{\rm BH}$ estimates of all 260 quasars from the GNIRS-DQS sample calculated using the VP06 approach (y-axis) and correcting for accretion rate (x-axis). The dashed line represents a one-to-one relationship. This figure shows that Hβ-based $M_{\rm BH}$ esimates that were not corrected for accretion rate are systematically overestimated.

We compare the accretion rate corrected Hβ-based $M_{\rm BH}$ estimates for our sample to the traditional approach of VP06 which uses the following equation to obtain Hβ-based $M_{\rm BH}$ values:

$$\log\left(\frac{M_{\rm BH}}{M_\odot}\right) = 0.91 + 2\log\left(\frac{\rm FWHM_{H\beta}}{\rm km\ s^{-1}}\right) + 0.5\log\left(\frac{\lambda L_\lambda(5100\text{Å})}{10^{44}\rm erg\ s^{-1}}\right), \tag{4.5}$$

utilizing a virial factor on the order of unity. Figure 4.1 presents the Hβ-based $M_{\rm BH}$ masses for our sample, based on the relation of VP06 against our accretion-rate-corrected values. We find that the masses, computed according to the VP06 approach, are systematically overestimated by 0.26 dex, consistent with the [84] finding.

Given that correcting for accretion-rate is necessary for reliable $M_{\rm BH}$ estimates, we explore whether additional accretion rate based corrections would further improve $M_{\rm BH}$ estimates for rest-frame UV emission lines. To accomplish this, we introduce a term into our UV-based $M_{\rm BH}$ estimates that includes the C IV EW, as this parameter has been shown to be generally anti-correlated with the quasar's accretion rate [e.g., 9, 135].

Following Equation 4.3 with the addition of our C IV EW term, we derive C IV-based $M_{\rm BH}$ estimates as

$$\log\left(\frac{M_{\rm BH}}{M_\odot}\right) = 2\log\left(\frac{\Delta V}{1000\ {\rm km\ s^{-1}}}\right) + 0.5\log\left(\frac{\lambda L_\lambda(1350\text{Å})}{10^{44}{\rm erg\ s^{-1}}}\right) + \ a + b\log\left(\frac{\rm EW_{CIV}}{\text{Å}}\right). \tag{4.6}$$

The coefficients a and b were determined from a linear-regression analysis to the calibration set of Hβ-based $M_{\rm BH}$ estimates. By design, we allow a and b to freely vary during the regression analysis, resulting in a zero mean offset between the C IV-based and Hβ-based $M_{\rm BH}$ estimates.

The linear-regression was performed such that the difference between our UV-based $M_{\rm BH}$ values and the Hβ-based $M_{\rm BH}$ values was minimized. Specifically, we subtracted the first two terms in Equation 4.6 from the derived Hβ-based $M_{\rm BH}$ estimates and fit the remaining coefficients, a and b, to this difference. This was accomplished utilizing the REGSTATS function in the Statistics Toolbox 11.4 of MATLAB 9.5. As the errors associated with SE $M_{\rm BH}$ values are large (on the order of 0.5-0.6 dex and 0.7 dex for relative and absolute uncertainty, respectively; see, Section 4.4), we did not include the errors as part of the linear-regression. Despite this, we also employed the LINMIX_ERR algorithm [72] where we adopted a 0.5 dex uncertainty to have a basis of comparison for our regression, and found the results were generally consistent. The uncertainty of the coefficients, presented in our equations below, stem directly from the linear fit.

Unlike the case for C IV above, for Mg II-based $M_{\rm BH}$ estimates, we calibrate our estimates in two separate runs using the following equation,

$$\log\left(\frac{M_{\rm BH}}{M_\odot}\right) = 2\log\left(\frac{\Delta V}{1000\ {\rm km\ s^{-1}}}\right) + 0.5\log\left(\frac{\lambda L_\lambda(3000\text{Å})}{10^{44}{\rm erg\ s^{-1}}}\right) + \ c + d\log\left(\frac{\rm EW_{CIV}}{\text{Å}}\right), \tag{4.7}$$

where ΔV is the velocity width of Mg II; the Mg II lines were measured from a combination of the SDSS and GNIRS spectra of the sources as described below. The coefficients c and d were determined differently in each run through a linear-regression analysis to the calibration set of Hβ-based $M_{\rm BH}$ estimates. The first run set the coefficient d to 0 in order to provide a prescription that only used the Mg II emission line while allowing c to be a free parameter. For this run we did not need any C IV measurements, allowing us to use all of the Mg II measurements in each subsample (see, Section 5.2.2). The second run allowed both c and d to be free parameters during the regression. This run required C IV measurements, reducing our Mg II sample as described in Section 5.2.2. In both runs, we used the same type of linear-regression as discussed for the C IV analysis, but using Equation 4.7 and coefficients c and d instead.

Given the considerably lower S/N ratio of the GNIRS spectra at $\lambda \lesssim 1.2\ \mu$m (M21), we split the analysis utilizing the Mg II line measured from the GNIRS spectra into three different parts based on source redshift (see Section 5.2.2). In addition to these subsamples, we analyzed the total of 160 and 225 sources for the subsample including SDSS and/or GNIRS Mg II measurements with and without C IV. For the subsample of 53 sources that have Mg II measurements available in both the GNIRS and SDSS spectra, the average of these measurements was used in the regression analyses (see Section 4.3.4).

4.3.2. Testing Different Velocity Width Parameters

We substitute the FWHM, MAD, and $\sigma_{\rm line}$ as the velocity width parameter in each of our $M_{\rm BH}$ estimates in Equations 4.6 and 4.7 to investigate which of these provides $M_{\rm BH}$ values closest to those obtained from Hβ. We calibrate the C IV- and Mg II-based $M_{\rm BH}$ estimates to the Hβ-based values that use the FWHM for the velocity width of Hβ [84].

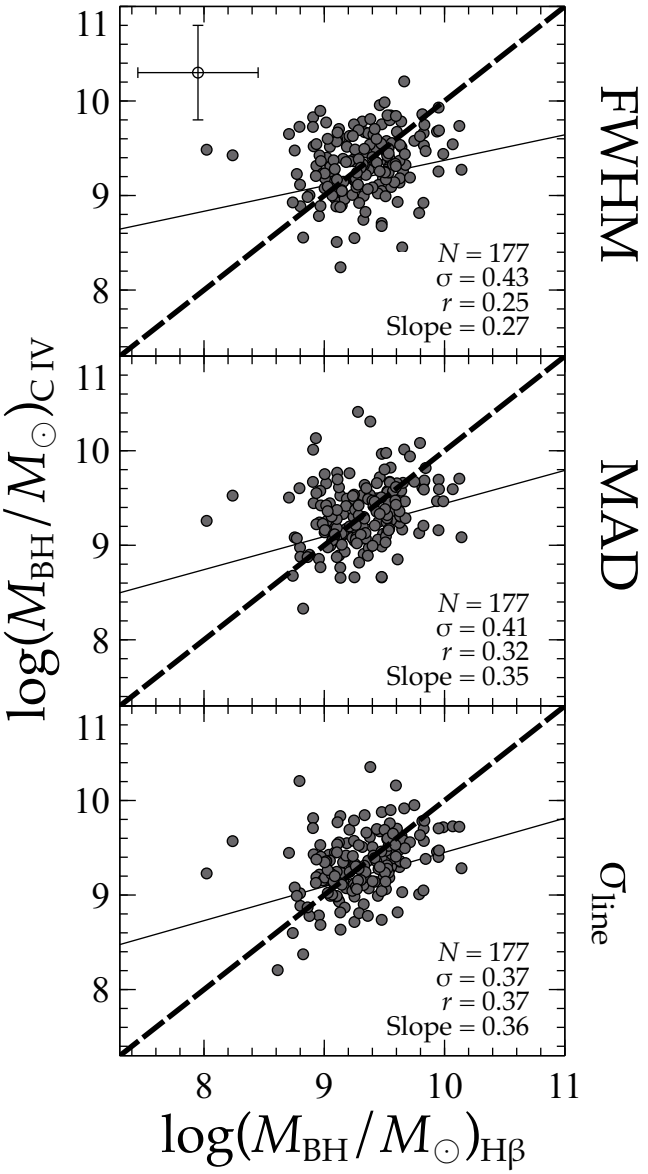

Figure 4.2 The calibrated C IV-based $M_{\rm BH}$ estimates using the three velocity width parameters, discussed in Section 4.3.1, against the calibration set of Hβ-based $M_{\rm BH}$ estimates. The dashed line in each panel represents a one-to-one relationship and the thin solid line in each panel represents the best linear fit to the data. The r value provided in each panel is the Pearson correlation coefficient and the slope is the slope of the best-fit line. Notably, using $\sigma_{\rm line}$ as the velocity width parameter provides the most precise C IV-based $M_{\rm BH}$ estimates with respect to the Hβ-based $M_{\rm BH}$ estimates. Additionally, using $\sigma_{\rm line}$ as the velocity width parameter leads to the largest Pearson correlation coefficient and steepest slope of the best fit relation. Typical uncertainty of 0.5 dex on the $M_{\rm BH}$ values is displayed in the top panel for reference.

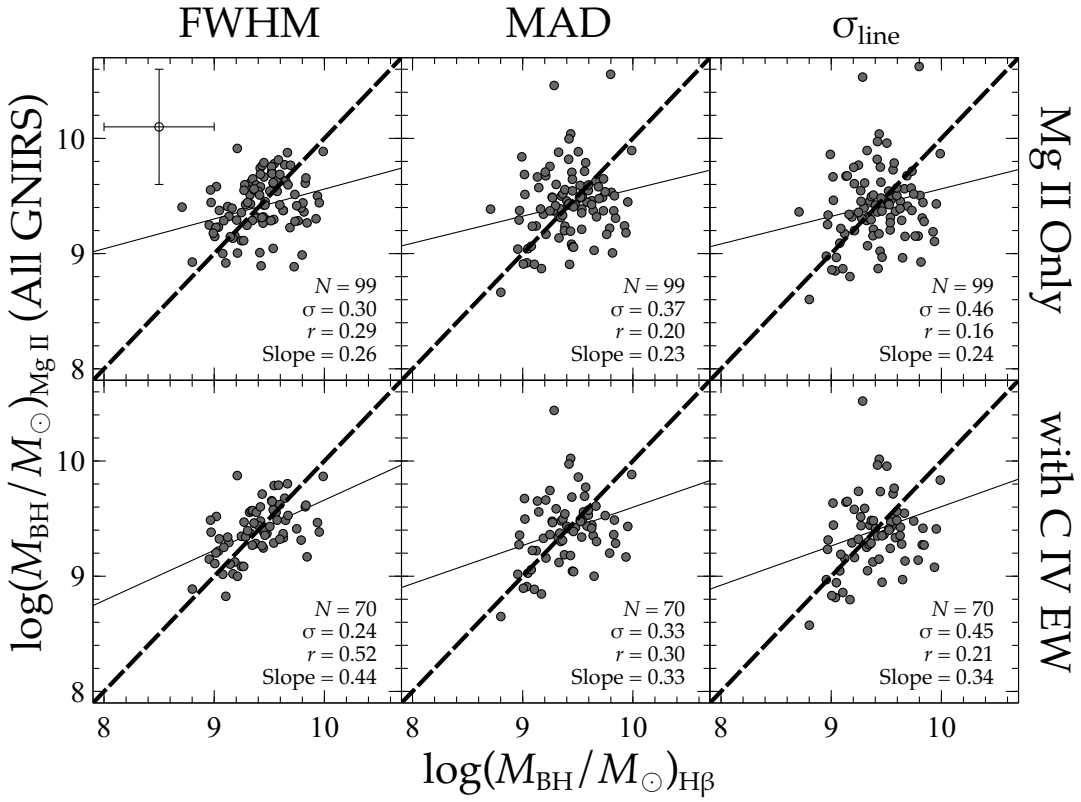

Figure 4.3 Calibrated Mg II-based $M_{\rm BH}$ estimates using the three velocity width parameters against the Hβ-based $M_{\rm BH}$ estimates; the bottom panels present the results when adding EW(C IV) to the analysis as discussed in Section 4.3.1. The symbols are the same as in Figure 4.2. For all the Mg II-based $M_{\rm BH}$ estimates, using the FWHM as the velocity width parameter provided the most accurate and precise results when compared to the Hβ-based $M_{\rm BH}$ estimates. As can be seen when comparing the standard deviations and r from the top panels and the bottom panels, including the C IV EW in the Mg II-based $M_{\rm BH}$ estimate resulted in a higher precision for each velocity width parameter. Typical uncertainty of 0.5 dex on the $M_{\rm BH}$ values is displayed in the top left panel for reference.

For the C IV-based $M_{\rm BH}$ estimates, presented in Figure 4.2, $\sigma_{\rm line}$ produced the most reliable results when compared to the Hβ-based $M_{\rm BH}$ values. We determined which velocity width parameter was preferred based on the lowest standard deviation, steepest slope of the best-fit relation and largest Pearson correlation coefficient when comparing the resulting UV- and Hβ-based $M_{\rm BH}$ values.

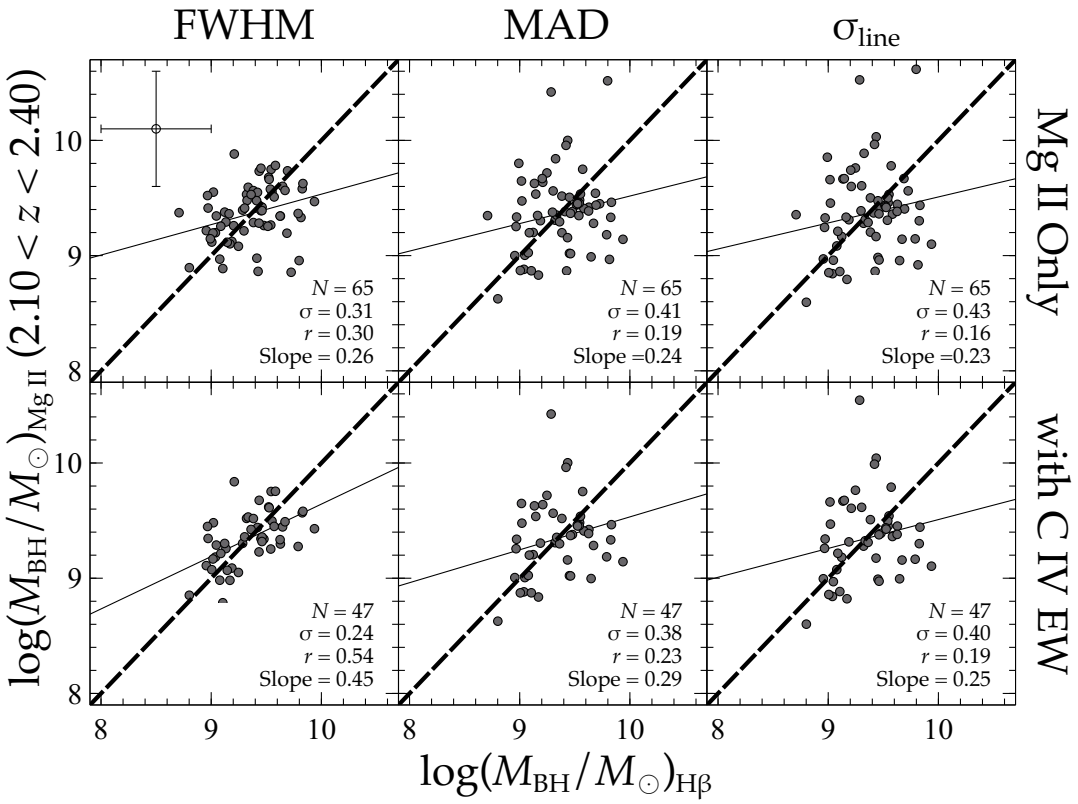

Figure 4.4 Same as Figure 4.3 but for the subset of sources in the range $2.10 \lesssim z \lesssim 2.40$. As observed for the entire redshift range (Figure 4.3), the FWHM of Mg II is the most reliable velocity width parameter and the inclusion of the C IV EW helped improve the accuracy and precision of the Mg II-based $M_{\rm BH}$ estimates with respect to the Hβ-based estimates.

For each of the Mg II subsamples described above, we present the calibrated Mg II-based $M_{\rm BH}$ estimates in Figures 4.3, 4.4, 4.5, and 4.6 both with (bottom panels) and without (top panels) the inclusion of the C IV EW. Except for the subsample of sources at $3.20 \lesssim z \lesssim 3.50$, all the other Mg II-based subsamples showed the strongest corrrelation with the Hβ-based $M_{\rm BH}$ estimates when using the FWHM as the velocity width parameter for the Mg II line. For the subsample at $3.20 \lesssim z \lesssim 3.50$, we now find that using the MAD for the velocity width parameter in $M_{\rm BH}$ estimates provides the best results when using only the Mg II emission line (see, Figure 4.5). We also recognize that this small discrepancy may be a result of the limited sample size which may not provide meaningful statistics.

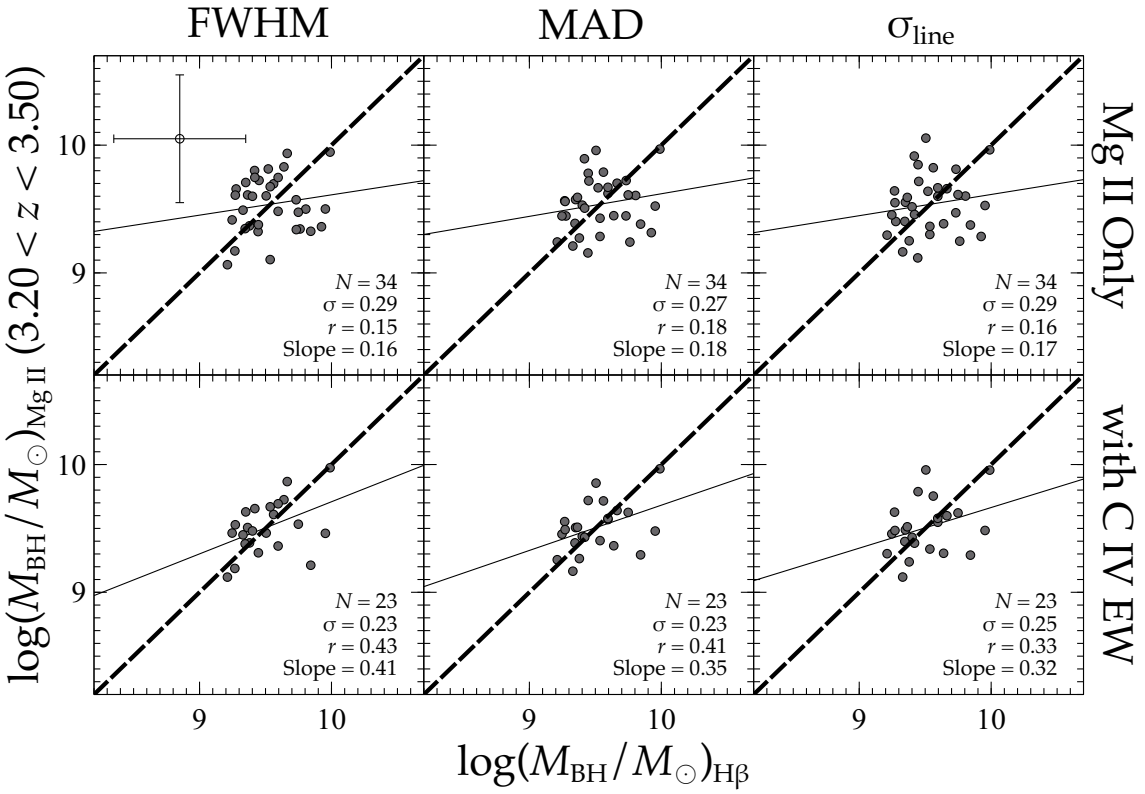

Figure 4.5 Same as Figure 4.3 but for the subset of sources in the range $3.20 \lesssim z \lesssim 3.50$. In this subset of sources the most reliable velocity width parameter for deriving Mg II only-based $M_{\rm BH}$ estimates is the MAD instead of the FWHM. This is determined from evaluating the standard deviations and r in each panel. This disparity suggests the importance of expanding the sample of quasars that lie in this redshift range. As we find for the entire redshift range, the inclusion of the EW of C IV (bottom panels) improves the accuracy and precision of these Mg II-based $M_{\rm BH}$ estimates.

In spite of this, the results from this subsample are considered to be the least uncertain given that Mg II and Hβ are measured in the same spectrum with the highest S/N ratio possible. The best fit coefficients stemming from our linear-regression analyses appear in Table 4.2.

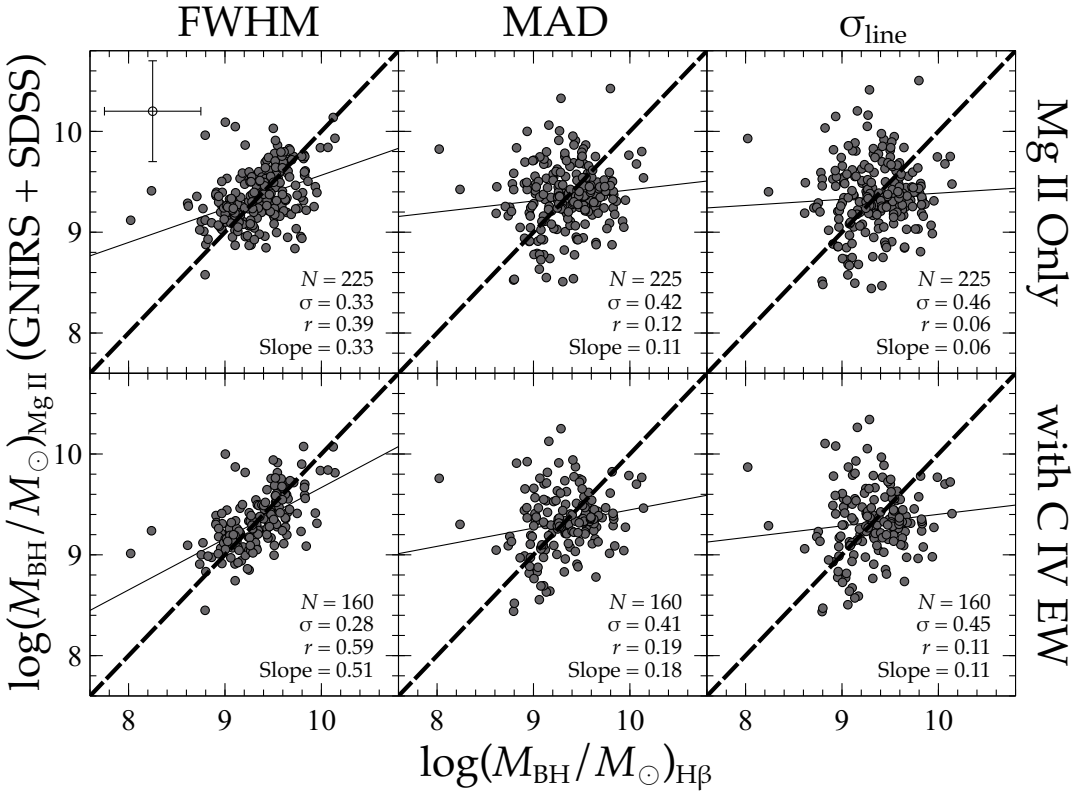

Figure 4.6 Same as Figure 4.3 but for the source sample having Mg II measurements taken from GNIRS-DQS and/or SDSS. From evaluating the standard deviations and Pearson correlation coefficients in each panel, we find that using the FWHM as the velocity width parameter in the calculation for Mg II-based $M_{\rm BH}$ estimates provides the most reliable $M_{\rm BH}$ estimates with respect to the Hβ-based $M_{\rm BH}$ values. As we find for each Mg II subsample, the inclusion of the EW of C IV (bottom panels) improves the accuracy and precision of our Mg II-based $M_{\rm BH}$ estimates.

4.3.3. Comparison with Previous Studies

In order to have a basis of comparison for this work, we provide estimates for the C IV-based $M_{\rm BH}$ values for our sample using the prescriptions provided in VP06, [109, hereafter P17], and [27, hereafter C17]. VP06, P17, and C17, use the following Equations to determine C IV-based $M_{\rm BH}$ estimates, respectively,

$$\log\left(\frac{M_{\rm BH}}{M_\odot}\right) = 6.66 + 2.0\log\left(\frac{\rm FWHM_{CIV}}{1000\ {\rm km\ s^{-1}}}\right) + 0.53\log\left(\frac{\lambda L_\lambda(1350\text{Å})}{10^{44}{\rm erg\ s^{-1}}}\right), \tag{4.8}$$

$$\log\left(\frac{M_{\rm BH}}{M_\odot}\right) = 6.73 + 2.0\log\left(\frac{\sigma_{\rm line,CIV}}{1000\ {\rm km\ s^{-1}}}\right) + 0.43\log\left(\frac{\lambda L_\lambda(1350\text{Å})}{10^{44}{\rm erg\ s^{-1}}}\right), \tag{4.9}$$

$$\log\left(\frac{M_{\rm BH}}{M_\odot}\right) = 6.71 + 2.0\log\left(\frac{\rm FWHM_{CIV,Corr.}}{1000\ {\rm km\ s^{-1}}}\right) + 0.53\log\left(\frac{\lambda L_\lambda(1350\text{Å})}{10^{44}{\rm erg\ s^{-1}}}\right). \tag{4.10}$$

C17 uses a velocity width ($\rm FWHM_{CIV,Corr.}$) that has been adjusted by the blueshift of the C IV emission-line peak with respect to the line peak of Hβ [see, 27].

In Figure 4.7 we present the C IV-based $M_{\rm BH}$ estimates for our sample based on the prescriptions from the literature. In comparison, our prescription,

$$\begin{aligned}\log\left(\frac{M_{\rm BH}}{M_\odot}\right) = 6.299 \pm 0.169 + 2\log\left(\frac{\sigma_{\rm line}}{1000\ {\rm km\ s^{-1}}}\right) + \\ 0.5\log\left(\frac{\lambda L_\lambda(1350\text{Å})}{10^{44}{\rm erg\ s^{-1}}}\right) + 0.385 \pm 0.119\log\left(\frac{\rm EW_{CIV}}{\text{Å}}\right),\end{aligned} \tag{4.11}$$

which is plotted at the bottom panel of Figure 4.2, provides the smallest scatter, steepest slope of the best-fit relation, largest Pearson correlation coefficient, and, by design, corrects the mean offset[2] between previous C IV-based $M_{\rm BH}$ estimates and Hβ-based $M_{\rm BH}$ values.

To form a basis of comparison for our Mg II-based $M_{\rm BH}$ estimates, we followed the prescriptions provided in [158, hereafter VO09], [174, hereafter Z15], and [77, hereafter L20]. VO09, Z15, and L20 use the following Equations to determine Mg II-based $M_{\rm BH}$ estimates, respectively,

$$\log\left(\frac{M_{\rm BH}}{M_\odot}\right) = 0.86 + 2.0\log\left(\frac{\rm FWHM_{MgII}}{\rm km\ s^{-1}}\right) + 0.5\log\left(\frac{\lambda L_\lambda(3000\text{Å})}{10^{44}{\rm erg\ s^{-1}}}\right), \tag{4.12}$$

$$\log\left(\frac{M_{\rm BH}}{M_\odot}\right) = 1.07 + 2.0\log\left(\frac{\rm FWHM_{MgII}}{\rm km\ s^{-1}}\right) + 0.48\log\left(\frac{\lambda L_\lambda(3000\text{Å})}{10^{44}{\rm erg\ s^{-1}}}\right), \tag{4.13}$$

[2]The mean offset correction accounts for the bias introduced when not considering a source's accretion rate in their Hβ-based $M_{\rm BH}$ values [see, 84].

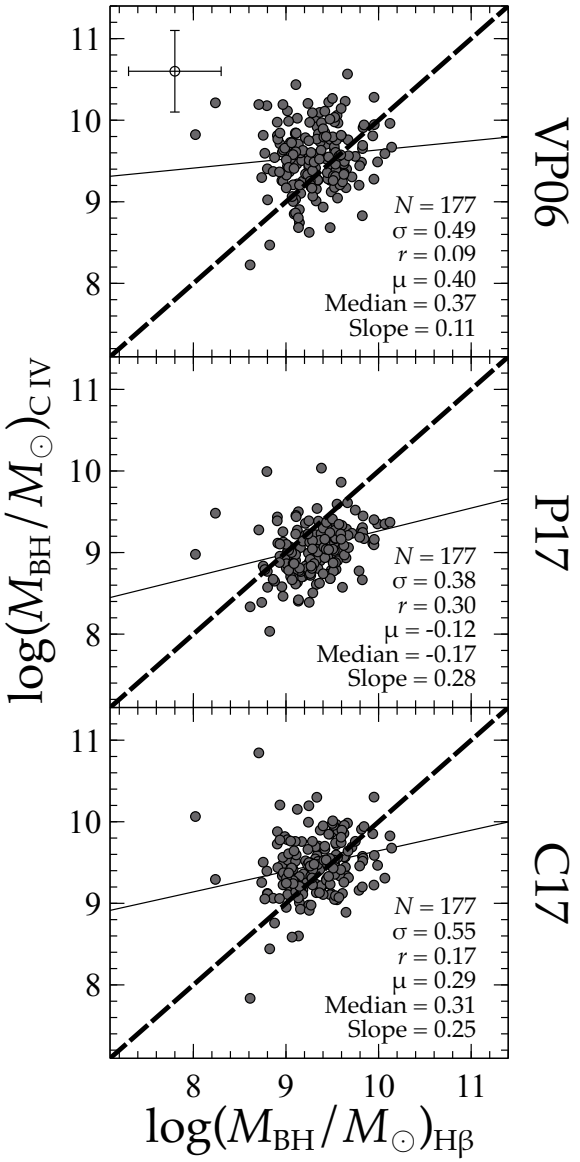

Figure 4.7 C IV-based $M_{\rm BH}$ estimates of our sample derived through the methodology of, from top to bottom: VP06, P17, and C17 against the Hβ-based $M_{\rm BH}$ estimates. The dashed lines represent one-to-one relationships and the thin solid lines represent the best linear fit to the data in each panel. The most reliable C IV-based $M_{\rm BH}$ values from this work were derived utilizing $\sigma_{\rm line}$ as the velocity width parameter (see the bottom panel of Figure 4.2). Our prescription shows a considerable improvement in the value of the Pearson correlation coefficient, r, albeit a modest improvement in the standard deviation, with respect to previous work. Additionally, our prescription corrects the mean offset due to considering the accretion rate when estimating Hβ-based $M_{\rm BH}$ values. Typical uncertainty of 0.5 dex on the $M_{\rm BH}$ values is displayed in the top panel for reference.

$$\log\left(\frac{M_{\rm BH}}{M_\odot}\right) = 7.00 + 2.0\log\left(\frac{\rm FWHM_{MgII}}{1000\ {\rm km\ s^{-1}}}\right) + 0.5\log\left(\frac{\lambda L_\lambda(3000\text{Å})}{10^{44}{\rm erg\ s^{-1}}}\right). \tag{4.14}$$

In Figure 4.8, we present the Mg II-based $M_{\rm BH}$ estimates from Equations 4.12, 4.13, and 4.14. The three panels of Figure 4.8 that correspond to these three equations are almost identical to each other given the similarities between these equations. For comparison, we elect to use the Mg II subsample that contains SDSS and/or GNIRS measurements as it is the largest and, therefore, provides the most meaningful statistics. From our comparison, we find that our Mg II-based $M_{\rm BH}$ estimates given by,

$$\log\left(\frac{M_{\rm BH}}{M_\odot}\right) = 7.000 \pm 0.022 + 2\log\left(\frac{\rm FWHM_{MgII}}{1000\ {\rm km\ s^{-1}}}\right) + 0.5\log\left(\frac{\lambda L_\lambda(3000\text{Å})}{10^{44}{\rm erg\ s^{-1}}}\right) \tag{4.15}$$

which is plotted at the top left panel of Figure 4.6, provides results that are consistent with those from the prescriptions of the previous studies except for the mean offset correction stemming from consideration of the accretion rate. The consistency between Equations 4.14 and 4.15 confirm the results derived in L20.

When the C IV EW is included in the regression analysis for the Mg II-based $M_{\rm BH}$ values, we obtain the following prescription (for 160 sources; see, Section 5.2.2),

$$\begin{aligned}\log\left(\frac{M_{\rm BH}}{M_\odot}\right) = 6.793 \pm 0.047 + 2\log\left(\frac{\rm FWHM_{MgII}}{1000\ {\rm km\ s^{-1}}}\right) + \\ 0.5\log\left(\frac{\lambda L_\lambda(3000\text{Å})}{10^{44}{\rm erg\ s^{-1}}}\right) + 0.005 \pm 0.001\log\left(\frac{\rm EW_{CIV}}{\text{Å}}\right),\end{aligned} \tag{4.16}$$

which is plotted in the bottom left panel of Figure 4.6. In this case, we see a clear improvement in the scatter and the Pearson correlation coefficient and slope of the best-fit relation.

We report all the $M_{\rm BH}$ estimates stemming from our analysis for the Hβ, C IV and Mg II emission lines in Table 4.3 where Column (1) provides the SDSS designation of the object, and Columns (2), (3), and (4) provide the Hβ-based $M_{\rm BH}$ estimates derived using the FWHM, MAD, and $\sigma_{\rm line}$ as the velocity width, respectively. Columns (5), (6), and (7) provide C IV-based $M_{\rm BH}$ estimates derived from VP06, P17, and C17, respectively.

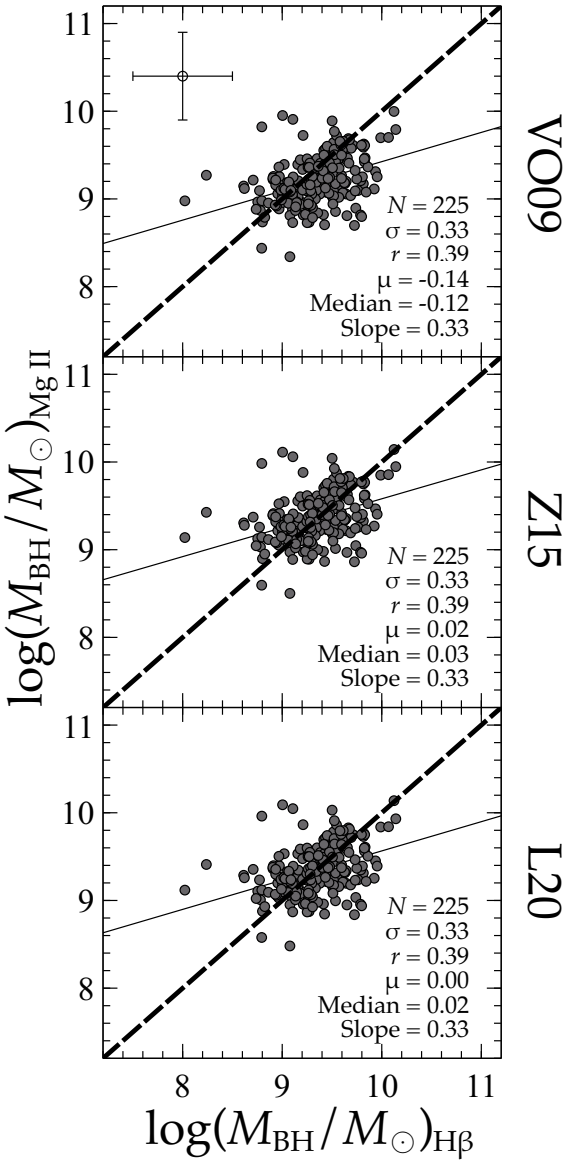

Figure 4.8 Mg II-based $M_{\rm BH}$ estimates of our sample derived through the methodology of, from top to bottom, VO09, Z15, and L20 against the Hβ-based $M_{\rm BH}$ estimates. The panels include all Mg II measurements available in SDSS and/or GNIRS. The dashed line in each panel represents a one-to-one relationship and the thin solid line in each panel represents the best linear fit to the data. We find that our results are consistent with those of previous work when only measuring Mg II, but are clearly improved with the inclusion of the C IV EW (see the left most panels of Figure 4.6). Our prescriptions, by design, correct the mean offsets between the Mg II- and Hβ-based $M_{\rm BH}$ values with or without the inclusion of the C IV EW. Typical uncertainty of 0.5 dex on the $M_{\rm BH}$ values is displayed in the top panel for reference.

Columns (8), (9), and (10) are the C IV-based estimates derived using the regression analysis for each C IV velocity width parameter, FWHM, MAD, and $\sigma_{\rm line}$, respectively. We report in columns (11), (12), and (13) the Mg II-based $M_{\rm BH}$ estimates derived using the prescriptions of VO09, Z15, and L20. Lastly, in columns (14), (15), and (16), we report the Mg II-based $M_{\rm BH}$ estimates using each of the three Mg II velocity width parameters, FWHM, MAD, and $\sigma_{\rm line}$, respectively. For our Mg II-based $M_{\rm BH}$ estimates, values are provided with and without the C IV EW term.

4.3.4. Mg II Covered by both SDSS and GNIRS Spectra

For 53 sources from the GNIRS-DQS catalog of M22, in the $2.10 \lesssim z \lesssim 2.40$ redshift range, we have measurable Mg II profiles from both GNIRS and SDSS spectra. In order to confirm consistency across the SDSS and GNIRS spectra, we compare the effects of measuring these spectra in different epochs using different instruments by evaluating the differences in Mg II-based $M_{\rm BH}$ estimates stemming from each spectrum. In order to stay consistent, we used the VO09 method for calculating the Mg II-based $M_{\rm BH}$ estimates for all measurements in our comparison. This comparison is presented in Figure 4.9. Overall, we conclude that the two sets of measurements are consistent with each other and the mean offset between the $\log(M_{\rm BH})$ values is only -0.012.

4.4. Discussion

In this work, we perform calibrations between C IV- and Mg II-based $M_{\rm BH}$ estimates and those based on the Hβ line using the largest, homogeneous sample of luminous quasars at high redshift that cover these three emission lines. The Hβ-based $M_{\rm BH}$ estimates that we calibrate to are accretion-rate-corrected according to the scaling relation presented in [39] that involves the optical Fe II emission. We show that the inclusion of the C IV EW in our calibrations to these Hβ-based $M_{\rm BH}$ values allow for an additional accretion-rate correction in UV-based $M_{\rm BH}$ estimates. The inclusion of this term in our prescriptions leads to UV-based $M_{\rm BH}$ estimates that are closest to those obtained from Hβ.

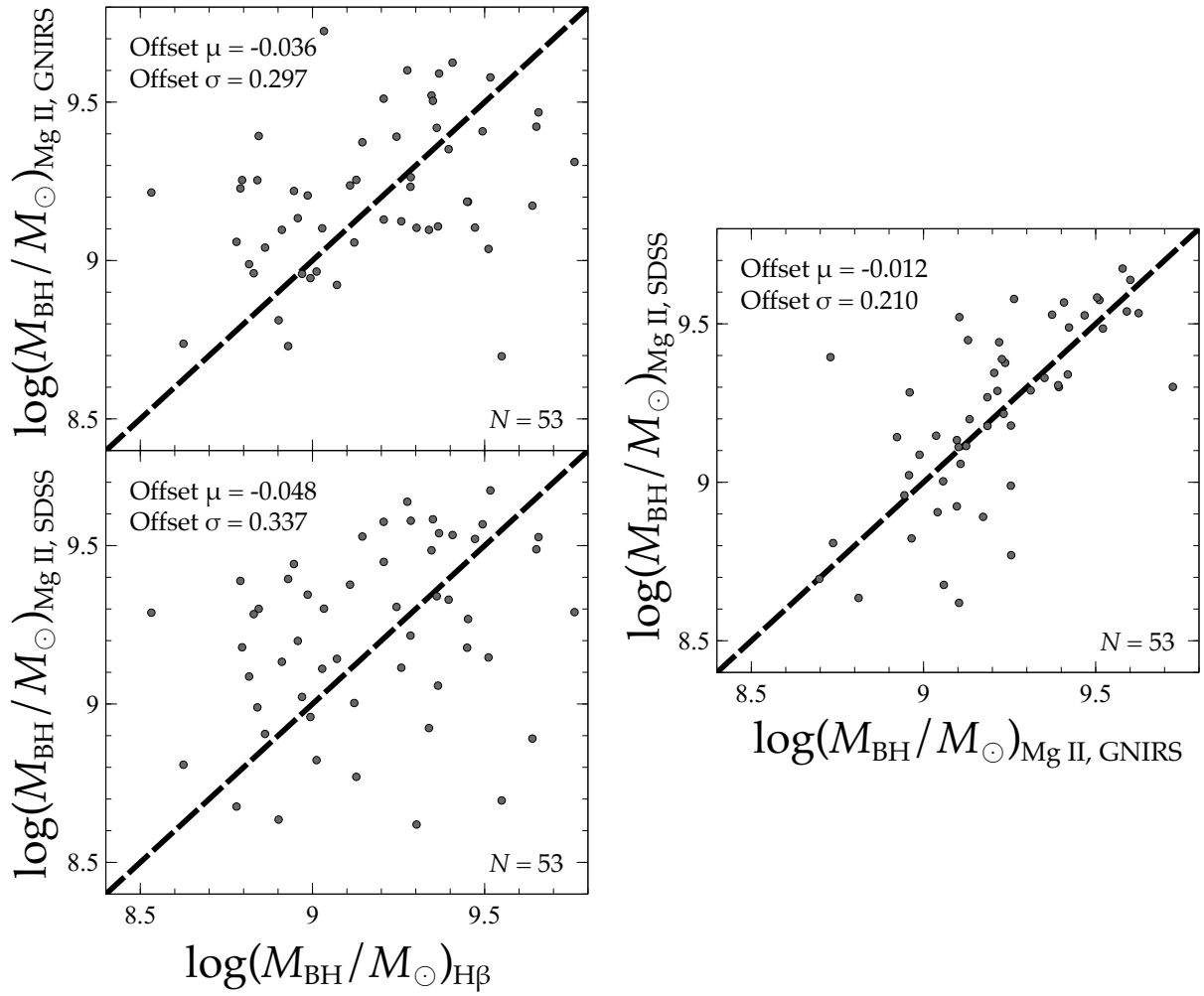

Figure 4.9 The upper leftmost and lower leftmost panel compare the GNIRS-DQS and SDSS, respectively, Mg II-based $M_{\rm BH}$ estimates based on the VO09 methodology using the Hβ-based masses. The rightmost panel presents the direct comparison of the SDSS- and GNIRS-DQS-based estimates to each other. In each panel, the mean and standard deviation of the residuals are reported. The dashed line in each panel represents a one-to-one relationship. Overall, we find that the measurements of the Mg II lines from the GNIRS spectra are consistent with the respective measurements from SDSS.

Our results display improvements with respect to similar $M_{\rm BH}$ calibrations from previous studies that excluded such accretion-rate corrections. When utilizing $\sigma_{\rm line}$ as the velocity width parameter, we obtain the most reliable prescription (Equation 4.11) for

C IV-based $M_{\rm BH}$ values, compared with previous studies of this kind. As shown in the bottom panel of Figure 4.2 we reduce the scatter of C IV-based $M_{\rm BH}$ estimates with respect to those from Hβ by $\sim$ 24%, $\sim$ 3%, and $\sim$ 33% compared to the prescriptions of VP06, P17, and C17, respectively (see, Figure 4.7). Similarly, the Pearson correlation coefficient between C IV-based and Hβ-based $M_{\rm BH}$ values improves from 0.09, 0.30, and 0.17 to 0.37, respectively. The slope of the best-fit relation between C IV-based and Hβ-based $M_{\rm BH}$ values also improves from 0.11, 0.28, and 0.25 to 0.36, respectively.

We also present a prescription (Equation 4.15) for obtaining Mg II-based $M_{\rm BH}$ estimates when only the Mg II line is covered in the spectrum. This prescription is consistent with the findings of L20, confirming their results. This L20 prescription is recommended when only the Mg II emission line is available as there is no systematic mean offset present when compared to the accretion-rate corrected Hβ-based masses. We also note that for the subsample of 34 sources in the highest redshift bin ($3.20 \lesssim z \lesssim 3.50$), the scatter in our prescription is further reduced by $\sim$ 25% (see, Figures 4.5 and 4.6). A larger sample of sources in this redshift range is necessary in order to draw firm conclusions as to whether a larger improvement can be achieved.

When we introduce the additional accretion-rate correction factor, in the form of the EW of C IV, we obtain a significantly improved Mg II-based $M_{\rm BH}$ value using Equation 4.16. Compared to the Mg II-based $M_{\rm BH}$ estimates derived from Equation 4.15, this prescription reduces the scatter in the calibration with Hβ-based $M_{\rm BH}$ estimates, by $\sim$ 15%. Similarly, the Pearson correlation coefficient is increased by $\sim$ 51% (see, Figure 4.6). With respect to previous studies discussed throughout this work, our prescriptions, by design, correct the mean offset between UV-based and accretion-rate-corrected Hβ-based $M_{\rm BH}$ estimates. These corrections are critical, as manifested in Figures 4.7 and 4.8, where mean offsets of up to 0.40 and 0.14 appear in the μ values for C IV and Mg II, respectively.

We note that SE $M_{\rm BH}$ estimates, in general, have a 0.5-0.6 dex relative uncertainty and 0.7 dex absolute uncertainty [e.g., Table 5, 160]. Meanwhile, $M_{\rm BH}$ measurements that stem from RM campaigns have an inherent uncertainty of 0.3-0.5 dex due to their

calibration against the $M - \sigma_\star$ relation [e.g. 113, 157, 137, 58], and such observations are quite challenging at high redshift [e.g., 68]. While not being able to completely bridge the gap between these two approaches, the improvements this work provides to the accuracy and precision of SE UV-based $M_{\rm BH}$ estimates are considerable. We find that even when significant outliers are removed from all the $M_{\rm BH}$ comparisons performed above, the resulting improvements in the scatter of up to $\sim 7\%$ do not warrant the removal of otherwise ordinary looking sources from the sample. Overall, our work shows that when using a large, uniform calibration sample of quasars having coverage of C IV, Mg II, Fe II and Hβ, and when correcting for accretion rate both in the optical ($\mathcal{R}_{\rm Fe}$) and in the UV (EW(C IV)), one can obtain the most reliable prescriptions for obtaining SE UV-based $M_{\rm BH}$ estimates.

4.4.1. Hα-based $M_{\rm BH}$ values

The GNIRS-DQS spectral inventory of M22 also provides measurements for the Hα emission line where available. In order to test the applicability of using this emission line as a $M_{\rm BH}$ indicator [e.g., 53], we ran the entire regression analyses presented in this paper substituting FWHM(Hα) for FWHM(Hβ). We find that the results based on Hα are consistent with those obtained from Hβ, thereby confirming the applicability of using Hα to estimate $M_{\rm BH}$ values in quasars.

4.5. Conclusions

We provide prescriptions for reliable rest-frame UV-based $M_{\rm BH}$ estimates with respect to $M_{\rm BH}$ estimates obtained from the Hβ line. Utilizing the GNIRS-DQS catalog (M22), we calibrate SE C IV- and Mg II-based $M_{\rm BH}$ estimates to Hβ-based $M_{\rm BH}$ estimates using a linear regression analysis that includes two basic accretion-rate observable indicators: the relative strength of the optical Fe II emission with respect to Hβ and the EW of the C IV emission line. We also investigate the use of different velocity width parameters for the C IV- and Mg II-based $M_{\rm BH}$ estimates and compare our results with previous studies. We summarize our main results as follows:

(1) The Hβ-based $M_{\rm BH}$ estimates in this work are overestimated by a factor of ~ 2 when the relative strength of the optical Fe II emission is not taken into account, consistent with the results of [84]. All of the $M_{\rm BH}$ prescriptions throughout this work take that correction into account.

(2) The inclusion of the C IV EW in our prescriptions considerably improves the accuracy and precision of UV-based $M_{\rm BH}$ estimates. With respect to previous studies, our most reliable UV-based $M_{\rm BH}$ values reduces the scatter by $\sim 15\%$ when compared to Hβ-based values.

(3) The preferred velocity width parameters for estimating $M_{\rm BH}$ using C IV and Mg II are $\sigma_{\rm line}$ and FWHM, respectively.

(4) Equation 4.11 presents the prescription for obtaining the most reliable C IV-based $M_{\rm BH}$ estimates, in the absence of Mg II coverage. Conversely, if the source's spectrum only covers the Mg II line, the prescription from L20 (Equation 4.14) is preferred. Otherwise, Equation 4.16 presents the most robust prescription for UV-based $M_{\rm BH}$ estimates when there is spectral coverage of both C IV and Mg II emission lines.

(5) NIR observations of additional sources at $3.20 \lesssim z \lesssim 3.50$ would allow us to test if further significant improvements can be achieved for UV-based $M_{\rm BH}$ estimates. Primarily, this redshift range reduces the uncertainty introduced when measuring Mg II by shifting the emission line further from the blue edge of the J-band. A larger sample with more reliable measurements at this range may reveal further discrepancies between low and high luminosity objects.

In the coming decade, we expect that millions of high-redshift ($z \gtrsim 0.8$) quasars will have $M_{\rm BH}$ estimates derived from rest-frame UV emission lines through large spectroscopic surveys, e.g., the Dark Energy Spectroscopic Instrument [DESI, 79, 33] and the 4m Multi-Object Spectroscopic Telescope [31]. It is therefore crucial to derive the most reliable $M_{\rm BH}$ estimates for future high-redshift quasar catalogs using the prescriptions provided in this work.

We gratefully thank the contributions to this work from Yue Shen and Michael A. Strauss. This work is supported by National Science Foundation grants AST-1815281 (C. D., O. S., B. M. M.), AST-1815645 (M. S. B., A. D. M.), and AST-2106990 (W. N. B.). I.A. acknowledges the support from Universidad Nacional de La Plata through grant 11/G153. This research has made use of the NASA/IPAC Extragalactic Database (NED), which is operated by the Jet Propulsion Laboratory, California Institute of Technology, under contract with the National Aeronautics and Space Administration.

Table 4.1. C IV and Mg II Spectroscopic Measurements

	C IV					Mg II						
Quasar	FWHM (km s^{-1})	MAD (km s^{-1})	$\sigma_{\rm line}$ (km s^{-1})	EW (Å)	$\lambda_{\rm peak}$ (Å)	FWHM (km s^{-1})	MAD (km s^{-1})	$\sigma_{\rm line}$ (km s^{-1})	EW (Å)	$\lambda_{\rm peak}$ (Å)	λL_{1350} (erg s^{-1})	λL_{3000} (erg s^{-1})
SDSS J001018.88+280932.5	2517^{+53}_{-78}	2274^{+37}_{-54}	3158^{+55}_{-82}	61^{+1}_{-1}	4045^{+0}_{-0}	···	···	···	···	···	46.4	···
SDSS J001249.89+285552.6	···	···	···	···	···	4195^{+188}_{-249}	2183^{+480}_{-757}	2956^{+637}_{-1017}	21^{+7}_{-9}	11874^{+3}_{-5}	···	46.9
SDSS J001355.10-012304.0	···	···	···	···	···	2815^{+344}_{-455}	1249^{+260}_{-401}	1595^{+332}_{-515}	17^{+1}_{-2}	12274^{+4}_{-5}	···	46.7
SDSS J001453.20+091217.6	6487^{+822}_{-1227}	3798^{+910}_{-1358}	5788^{+1383}_{-2064}	39^{+3}_{-5}	5152^{+5}_{-7}	2999^{+943}_{-1248}	1833^{+1906}_{-1833}	2375^{+2580}_{-2375}	25^{+8}_{-11}	9374^{+8}_{-10}	46.4	46.5
SDSS J001813.30+361058.6	6079^{+197}_{-294}	3247^{+238}_{-356}	3861^{+369}_{-550}	26^{+1}_{-2}	5116^{+2}_{-3}	5129^{+983}_{-1301}	3354^{+1648}_{-2632}	4543^{+2198}_{-3511}	25^{+8}_{-11}	9303^{+13}_{-17}	46.8	46.6
SDSS J001914.46+155555.9	4162^{+215}_{-320}	2329^{+81}_{-120}	3038^{+121}_{-180}	45^{+1}_{-1}	5054^{+1}_{-2}	4380^{+327}_{-433}	1628^{+821}_{-1235}	2061^{+1092}_{-1643}	23^{+1}_{-1}	9141^{+5}_{-6}	46.7	46.5
SDSS J002634.46+274015.5	5196^{+739}_{-1103}	6331^{+868}_{-1295}	6701^{+1462}_{-2181}	135^{+10}_{-15}	5023^{+5}_{-7}	3158^{+150}_{-198}	1747^{+645}_{-979}	2373^{+934}_{-1418}	36^{+1}_{-1}	9097^{+2}_{-2}	46.2	46.5
SDSS J003001.11-015743.5	6077^{+265}_{-396}	3339^{+251}_{-374}	3719^{+449}_{-669}	53^{+2}_{-3}	3995^{+1}_{-2}	···	···	···	···	···	45.9	···
SDSS J003416.61+002241.1	4213^{+107}_{-160}	2092^{+43}_{-65}	2710^{+66}_{-98}	29^{+0}_{-0}	4067^{+1}_{-1}	4141^{+203}_{-269}	1767^{+233}_{-308}	2278^{+414}_{-548}	39^{+2}_{-2}	7366^{+2}_{-2}	46.4	46.4
SDSS J003853.15+333044.3	8273^{+564}_{-841}	2485^{+403}_{-602}	3817^{+593}_{-884}	14^{+1}_{-1}	5213^{+11}_{-17}	···	···	···	···	···	46.3	···

Note. — C IV and Mg II emission line measurements for the first ten quasars in our sample. The entire table is available online.

Table 4.2. Regression Coefficients

Emission Line	FWHM	MAD	$\sigma_{\rm line}$
C IV (a, b)	$(5.172 \pm 0.196, 0.960 \pm 0.138)$	$(6.727 \pm 0.187, 0.250 \pm 0.131)$	**(6.299±0.169, 0.385±0.119)**
Mg II only (c, d)	**(7.000±0.022, 0)**	$(7.562 \pm 0.028, 0)$	$(7.309 \pm 0.031, 0)$
Mg II & C IV (c, d)	**(6.793±0.047, 0.005±0.001)**	$(7.410 \pm 0.0.068, 0.005 \pm 0.002)$	$(7.168 \pm 0.074, 0.004 \pm 0.002)$

Note. — Resulting regression coefficients from Equations 4.6 and 4.7 for each of our velocity width parameters. Bold coefficients are the recommended prescription for each emission line (see, Section 4.4).

Table 4.3. $M_{\rm BH}$ Estimates

	Hβ			C IV			Mg II								
Quasar	FWHM	MAD	$\sigma_{\rm line}$	VP06	P17	C17	FWHM	MAD	$\sigma_{\rm line}$	VO09	Z15	L20	FWHM[a]	MAD[a]	$\sigma_{\rm line}$[a]
SDSS J001018.88+280932.5	9.15	8.58	8.82	8.74	8.77	9.01	8.90	9.10	9.20	···	···	···	··· ···	··· ···	··· ···
SDSS J001249.89+285552.6	9.42	8.75	8.99	···	···	···	···	···	···	9.55	9.71	9.69	··· 9.69	··· 9.69	··· 9.70
SDSS J001355.10-012304.0	9.92	9.22	9.44	···	···	···	···	···	···	9.11	9.27	9.25	··· 9.25	··· 9.11	··· 9.07
SDSS J001453.20+091217.6	9.64	8.70	8.90	9.55	9.28	9.44	9.51	9.47	9.63	v9.05	9.22	9.20	9.20 9.20	9.36 9.33	9.33 9.30
SDSS J001813.30+361058.6	9.44	8.61	8.82	9.71	9.10	9.29	9.49	9.50	9.41	9.57	9.73	9.71	9.65 9.71	9.87 9.91	9.89 9.92
SDSS J001914.46+155555.9	9.32	8.81	9.08	9.30	8.83	9.38	9.32	9.20	9.22	9.37	9.53	9.51	9.54 9.51	9.27 9.22	9.22 9.17
SDSS J002634.46+274015.5	9.48	8.86	9.09	9.26	9.33	9.48	9.75	9.97	9.88	9.10	9.26	9.24	9.76 9.24	9.75 9.29	9.74 9.30
SDSS J003001.11-015743.5	9.18	8.50	8.71	9.25	8.70	9.17	9.36	9.17	9.07	···	···	···	··· ···	··· ···	··· ···
SDSS J003416.61+002241.1	9.33	8.71	8.96	9.16	8.61	9.13	9.00	8.91	8.90	9.27	9.44	9.41	9.36 9.41	9.21 9.23	9.18 9.20
SDSS J003853.15+333044.3	9.37	8.60	8.83	9.73	8.90	9.90	9.27	8.97	9.07	···	···	···	··· ···	··· ···	··· ···

[a]log($M_{\rm BH}$) estimates derived with (top row) and without (bottom row) the inclusion of the C IV EW, where available.

Note. — Data in this Table are presented as log($M_{\rm BH}/M_{\odot}$). Data for 10 sources are shown. The entire table is available online.

CHAPTER 5

SHEDDING NEW LIGHT ON WEAK EMISSION-LINE QUASARS IN THE C IV–Hβ PARAMETER SPACE

5.1. Introduction

Weak emission-line quasars (WLQs) are a subset of Active Galactic Nuclei (AGN) with extremely weak or undetectable rest-frame optical–UV emission lines [e.g., 42, 2, 28, 115]. The Sloan Digital Sky Survey [SDSS; 169] has discovered $\approx 10^3$ Type 1 quasars with Lyα+N v λ1240 rest-frame equivalent widths (EWs) < 15.4 Å and/or C IV λ1549 EW < 10.0 Å [e.g., 35, 93]. These numbers represent a highly significant concentration of quasars at $\gtrsim 3\sigma$ deviation from the log-normal EW distribution of the SDSS quasar population, with no corresponding "tail" at the opposite end of the distribution [35, 167]. Furthermore, the fraction of WLQs among the broader quasar population increases sharply at higher redshifts (and thus higher luminosities), from $\sim 0.1\%$ at $3 \lesssim z \lesssim 5$ to $\sim 10-15\%$ at $z \gtrsim 5.7$ [35, 4, 146].

Multi-wavelength observations of sources of this class have shown that they are unlikely to be high-redshift galaxies with apparent quasar-like luminosity due to gravitational-lensing amplification, dust-obscured quasars, or broad-absorption-line (BAL) quasars [e.g., 134, 136], but that their UV emission-lines are intrinsically weak. Furthermore, WLQs are typically radio-quiet, and have X-ray and mid-infrared properties inconsistent with those of BL Lac objects [132, 75, 167, 89].

About half of WLQs have notably lower X-ray luminosities than expectations from their monochromatic luminosities at 2500 Å [e.g., 81, 101, 100, 152]. One explanation for this phenomenon is that, at small radii, the geometrically thick accretion disks of these WLQs are 'puffed up' and prevent highly ionizing photons from reaching the broad emission-line region [BELR; e.g, 168, 167, 81, 101, 100]. The X-ray radiation is partially absorbed by the thick disk, resulting in low apparent X-ray luminosities at high inclinations (i.e., when these objects are viewed edge-on). When these objects are viewed at much

lower inclinations, their notably steep X-ray spectra indicate accretion at high Eddington luminosity ratio [$L_{\rm bol}/L_{\rm Edd}$, hereafter $L/L_{\rm Edd}$; e.g., 133, 81, 86].

The indications of high Eddington ratios in WLQs may provide a natural explanation for the weakness of their emission lines in the context of the Baldwin Effect. In its classical form, this effect is an anti-correlation between the EW(C IV) and the quasar luminosity [5]. Subsequent studies, however, have found that this relation stems from a more fundamental anti-correlation between EW(C IV) and Hβ-based $L/L_{\rm Edd}$ (Baskin & Laor 2004 [8], hereafter BL04; Dong et al. 2009 [37]). This anti-correlation, coined the Modified Baldwin Effect (MBE), was extensively studied and built upon by [135, hereafter SL15] [however, see also 163]. SL15 utilized a sample of nine WLQs and 99 non-radio-loud, non-BAL ('ordinary') quasars spanning wide ranges of luminosity and redshift to analyze the relative strength of the C IV emission-line and the Hβ-based Eddington ratio. They confirmed the findings of BL04 for the sample of ordinary quasars. However, all nine WLQs were found to possess relatively low $L/L_{\rm Edd}$ values, while the MBE predicts considerably higher Eddington ratios for these sources. This finding led SL15 to conclude that the Hβ-based $L/L_{\rm Edd}$ parameter cannot depend solely on EW(C IV) for all quasars. Such a conclusion may also be consistent with subsequent findings that WLQs possess strong Fe II emission and large velocity offsets of the C IV emission-line peak with respect to the systemic redshift (hereafter, Blueshift(C IV)) [87], and that $L/L_{\rm Edd}$ correlates with Blueshift(C IV) at high Blueshift(C IV) values [see Figure 14 of 119].

In this work, we explore two possible explanations for the findings of SL15. The first of these is that the traditional estimation of Hβ-based black-hole mass ($M_{\rm BH}$) values, and therefore $L/L_{\rm Edd}$ values, fails to accurately predict $M_{\rm BH}$, particularly in quasars with strong optical Fe II emission [e.g., 137]. Such a case is typical for WLQs, and thus a correction via measurement of the strength of the Fe II emission-complex in the optical band is required [39, 172]. The second explanation is that EW(C IV), by itself, is not an ideal indicator of the quasar accretion rate. In addition to EW(C IV), we utilize a recently defined parameter, the 'C IV || Distance' [124, hereafter R22], which represents a combination of the EW(C IV) and

Blueshift(C IV) [120, 125], and search for a correlation between that parameter and $L/L_{\rm Edd}$.

To investigate these explanations, we extend the WLQ sample of SL15 to nine additional sources available from the Gemini Near-IR Spectrograph - Distant Quasar Survey [GNIRS-DQS; 90, 2022, submitted, hereafter M22]. Furthermore, we study the distribution of WLQs in $L/L_{\rm Edd}$ space versus a sample of ordinary quasars from SL15 and M22. We aim to investigate the underlying driver for the weak emission lines in WLQs and test the assertion that all WLQs have extremely high accretion rates.

The structure of this paper is as follows. In Section 5.2, we discuss our sample selection and the relevant equations used to estimate Hβ-based $L/L_{\rm Edd}$ values. In Section 5.3, we analyze the samples' spectroscopic properties as well as the sources' black-hole masses and accretion rates. Then, we discuss the correlation between the C IV parameter space and $L/L_{\rm Edd}$. In Section 5.4, we summarize our findings. Throughout this paper, we compute luminosity distances using a standard ΛCDM cosmology with H_0 = 70 km s^{-1} Mpc^{-1}, $\Omega_{\rm M}$ = 0.3, and Ω_Λ = 0.7 [e.g., 148].

5.2. Sample Selection and Data Analysis

5.2.1. WLQ Sample

We compile a sample of 18 WLQs in this work. All these WLQs have accurate full-width-at-half-maximum intensity of the broad component of the Hβ λ4861 emission line (hereafter, FWHM(Hβ)), monochromatic luminosity at rest-frame 5100 Å (hereafter, νL_ν(5100 Å)), EW(Fe II $\lambda\lambda 4434-4684$), and EW(Hβ) measurements. Nine of these sources were obtained from SL15, seven from the GNIRS-DQS sample of M22 (see Section 5.2.2), and two from this work (see Appendix 5.5). SL15 compiled a sample of nine WLQs: SDSS J0836+1425, SDSS J1411+1402, SDSS J1417+0733, SDSS J1447−0203 [115, 116], SDSS J0945+1009 [63, 116], SDSS J1141+0219, SDSS J1237+6301 [35, 136], SDSS J1521+5202 [66, 168], and PHL 1811 [78].

Table 5.4 provides basic properties for the 18 WLQs in our sample. Column (1) provides the source name; Column (2) gives the systemic redshift determined from the peak of, in order of preference, the [[O III]] λ5007, Mg II λ2798, and Hβ emission lines;

Column (3) gives $\log \nu L_\nu$ (5100 Å); Column (4) gives FWHM(Hβ); Column (5) gives $R_{\rm Fe\,II} \approx$ EW(Fe II)/EW(Hβ); Column (6) gives traditional Hβ-based $M_{\rm BH}$ estimates (following Equations 5.2 and 5.4); Column (7) gives Fe II-corrected Hβ-based $M_{\rm BH,\,corr}$ estimates (following Equations 5.3 and 5.4); Column (8) gives traditional Hβ-based $L/L_{\rm Edd}$ values (from Equation 5.5); Column (9) gives Fe II-corrected Hβ-based $L/L_{\rm Edd,\,corr}$ values (from Equation 5.5); Column (10) gives EW(C IV); Column (11) gives Blueshift(C IV); Columns (12) and (13) provide the references for the rest-frame optical and UV spectral measurements, respectively. All derived properties are discussed in detail in Section 5.2.3.

The two WLQs from [136] and the two introduced in Appendix 5.5 do not have a reliable C IV line measurement in the literature, hence we perform our own measurements from their SDSS spectra, following the procedure in Dix et al. (2022, hereafter D22). Briefly, we fit the C IV emission line with a local, linear continuum and two independent Gaussians. These Gaussians are constrained such that the flux densities lie between 0 and twice the value of the peak of the emission line; the FWHM is restricted to not exceed 15000 km s^{-1}. The EW of the line emission can then be measured, as well as the blueshift, which is calculated from the difference between λ1549 and the peak of the Gaussians (see Equation 5.1).

These WLQs possess stronger relative optical Fe II emission (indicated by the larger $R_{\rm Fe\,II}$ values) compared to ordinary quasars from the same samples. WLQs are only selected based on their C IV emission-line strength (EW(C IV) $<$ 10 Å), so we are unaware of any biases introduced by the rest-frame optical emission to the selection process of the WLQs in this work.

5.2.2. Ordinary Quasar Sample Selection

In order to create a comprehensive comparison sample of quasars for our analysis, which requires measurements of both the Hβ and C IV emission lines, we select two catalogs of ordinary quasars from the literature. For the high-redshift quasars ($1.5 \lesssim z \lesssim 3.5$), C IV emission properties can be obtained from SDSS, but the Hβ emission line lies outside of the SDSS range, and therefore it has to be measured with NIR spectroscopy.

In this redshift range, we utilize the GNIRS-DQS catalog in M22. GNIRS-DQS is the largest and most comprehensive inventory of rest-frame optical properties for luminous quasars, notably the Hβ, [[O III]], and Fe II emission lines. To complement this sample of high-redshift, high-luminosity quasars, we include an archival sample of quasars in the low-redshift regime from the BL04 subsample also utilized in SL15. In this redshift range ($z < 0.5$), the Hβ emission properties can be obtained from optical spectra, but the C IV emission-line properties are more difficult to obtain, and are available primarily from the *Hubble Space Telescope* (HST) and the *International Ultraviolet Explorer* (IUE) archives. Below, we briefly discuss the selection process for our ordinary quasar sample.

The GNIRS-DQS sources were selected to lie in three narrow redshift intervals, $1.55 \lesssim z \lesssim 1.65$, $2.10 \lesssim z \lesssim 2.40$, and $3.20 \lesssim z \lesssim 3.50$ to center the Hβ+[[O III]] spectral complex in the NIR bands covered by GNIRS (i.e., the J, H, and K bands, respectively). In total, the survey comprises 260 sources with high-quality NIR spectra and comprehensive Hβ, [[O III]], and Fe II spectral measurements [see 90, and M22 for more details]. We exclude 64 BAL quasars, 16 radio-loud quasars (RLQs), and one quasar, SDSS J114705.24+083900.6 that is both BAL and radio loud. We define RLQs as sources having radio-loudness values of $R > 100$ [where R is the ratio between the flux densities at 5 GHz and 4400 Å; 71]. RLQs and BAL quasars are excluded to minimize the potential effects of continuum boosting from a jet [e.g., 93] and absorption biases (e.g., see BL04), respectively. Two quasars, SDSS J073132.18+461347.0 and SDSS J141617.38+264906.1, are excluded due to a lack of C IV measurements from D22. In total, 177 GNIRS-DQS quasars are included in our analysis; of these, seven sources with EW(C IV) < 10 Å can be formally classified as WLQs (see Section 5.2.1). We adopt values of FWHM(Hβ), νL_ν(5100 Å), EW(Hβ), and EW(Fe II) values from M22. The latter two parameters are used to derive $R_{\rm Fe\,II}$.

Quasars in the M22 sample are crossmatched with the C IV emission-line measurements from D22, who also report the wavelengths of the C IV emission-line peaks. The

Blueshift(C IV) values are derived following Equation (2) in [36]

$$\frac{\Delta v}{\mathrm{km\ s^{-1}}} = \left[\frac{c}{\mathrm{km\ s^{-1}}}\right]\left(\frac{z_{meas} - z_{sys}}{1 + z_{sys}}\right), \tag{5.1}$$

where z_{meas} is the redshift measured from the wavelength of the C IV emission-line peak, and z_{sys} is the systemic redshift with respect to the [[O III]], the Mg II, or the Hβ emission lines reported in M22. In this work, we report the Blueshift(C IV) $\equiv -\Delta v$ values.

WLQs often have extremely weak or undetectable [[O III]] emission, so we must use alternative emission lines as the reference for z_{sys}. Although there are known, non-negligible intrinsic uncertainties associated with using the Mg II and Hβ emission lines as z_{sys} indicators [$\sim 200\,\mathrm{km\,s^{-1}}$ and $\sim 400\,\mathrm{km\,s^{-1}}$, respectively; 140], WLQs often possess large Blueshift(C IV) values (> 2000 km s^{-1} in $\sim 60\%$ of the WLQs in our sample); therefore, the uncertainty associated with using, e.g., an Hβ-based z_{sys} value is relatively small compared to the quasar's Blueshift(C IV) value, and does not affect the conclusions of this work.

Sixty quasars at $z < 0.5$ from BL04 are added to our analysis from the 63 BL04 quasars in SL15. PG 0049+171, PG 1427+480, and PG 1415+451 are excluded due to a lack of published Fe II spectral measurements. The UV data in the BL04 sample comes, roughly equally, from both the *HST* and the *IUE* archives [see, 9]. Throughout this work, we check whether including only one *HST* or *IUE* data changes the conclusion of the paper, but we find no statistical difference in the results of Section 5.3. Therefore, we include both subsets in the main body of this work. We obtain the FWHM(Hβ), νL_ν(5100 Å), and $R_{\mathrm{Fe\,II}}$ values for the BL04 sources from [19], and their EW(C IV) and Blueshift(C IV) values from [9]. Table 5.4 lists the basic properties of the ordinary quasars in our sample with the same formatting as Table 5.4.

5.2.3. M_{BH} and L/L_{Edd} Estimates

Traditional estimation of single-epoch M_{BH} values has made use of the reverberation-mapping (RM) scaling relationship between the size of the Hβ-emitting region ($R_{\mathrm{H}\beta}$) and νL_ν(5100 Å) [e.g., 76, 162, 69, 12]. In this work, we use the empirical scaling relation

established by [12] for consistency with other recent studies [e.g., 84, D22]:

$$\log\left[\frac{R_{\mathrm{H}\beta}}{\mathrm{lt{-}days}}\right] = (1.527 \pm 0.031) + (0.533 \pm 0.035)\log \ell_{44} \tag{5.2}$$

where $\ell_{44} \equiv \nu L_\nu(5100\ \text{Å})\ /10^{44}\ \mathrm{erg\ s^{-1}}$.

However, the Hβ RM sample was subsequently determined to be biased toward objects with strong, narrow [[O III]] emission-lines, and, in effect, is biased in favor of low-accretion-rate broad-line AGNs [see, e.g., 127, 142]. Recent RM campaigns aimed at minimizing such bias, such as the Super-Eddington Accreting Massive Black Hole (SEAMBH; [38, 40, 41]) and the SDSS-RM project [139], found deviations from the traditional size-luminosity relationship. In particular, SEAMBH found a population of rapidly accreting AGNs with a BELR size up to 3-8 times smaller than predicted by Equation 5.2, which implies an overestimation of super-Eddington-accreting M_{BH} values from single-epoch spectra by the same factor. We apply a correction to the traditional Hβ-based M_{BH} estimation, developed by [39], which utilizes the $R_{\mathrm{Fe\,II}}$ parameter in addition to FWHM(Hβ) and νL_ν (5100 Å).

For the Fe II-corrected values of M_{BH} (hereafter, $M_{\mathrm{BH,\,corr}}$), we apply the size-luminosity scaling relation for $R_{\mathrm{H}\beta}$ following Equation (5) of [39]:

$$\log(R_{\mathrm{H}\beta}/\text{lt-days} = (1.65 \pm 0.06) + (0.45 \pm 0.03)\log(\ell_{44}) + (-0.35 \pm 0.08)R_{\mathrm{Fe\,II}} \tag{5.3}$$

Subsequently, M_{BH} ($M_{\mathrm{BH,\,corr}}$) can be estimated using the following relationship:

$$\begin{aligned}
&\frac{M_{BH}\ (M_{BH,\,corr})}{M_\odot} \\
&= f\left[\frac{R_{BELR}}{\mathrm{p}c}\right]\left[\frac{\Delta V}{\mathrm{k}m\ s^{-1}}\right]^2\left[\frac{G}{\mathrm{p}c\ M_\odot^{-1}\ (km\ s^{-1})^2}\right]^{-1} \\
&\approx 1.5\left[\frac{R_{\mathrm{H}\beta}\ (R_{\mathrm{H}\beta,\,corr})}{\mathrm{p}c}\right]\left[\frac{FWHM(H\beta)}{\mathrm{k}m\ s^{-1}}\right]^2 \\
&\cdot\left[\frac{4.3\times10^{-3}}{\mathrm{p}c\ M_\odot^{-1}\ (km\ s^{-1})^2}\right]^{-1},
\end{aligned} \tag{5.4}$$

where we adopt $f = 1.5$ for the virial coefficient, consistent with results from [58, 170, 171, 84], $R_{BELR} \approx R_{\mathrm{H}\beta}$ is the size-luminosity relation from Equation 5.2 or 5.3, ΔV is the

velocity width of the emission line, which is taken here as FWHM(Hβ), assuming Doppler broadening [162], and G is the gravitational constant.

The $L/L_{\rm Edd}$ parameter can be computed from the corresponding $M_{\rm BH}$ value following Equation (2) of [136] assuming that L_{Edd} is computed for the case of solar metallicity:

$$L/L_{\rm Edd,\,corr} = 1.06 f(L) \left[\frac{\nu L_\nu(5100\text{Å})}{10^{44}\text{ergs s}^{-1}}\right] \left[\frac{10^6 M_\odot}{M_{\rm BH,\,corr}}\right] \tag{5.5}$$

where $f(L)$ is the luminosity-dependent bolometric correction to νL_ν(5100 Å), derived from Equation (21) of [85].

We note that a wide range of bolometric corrections for quasars is available in the literature [e.g., 121, 96, 128, 97]. However, in general, the range of these corrections is not large enough to affect the conclusion of our work. For example, [84] recently used a constant bolometric correction of $L_{\rm Bol}/\nu L_\nu(5100\text{ Å}) \sim 9$; the bolometric corrections we derive are in the range of $\sim$ 5-6, which results in a relatively small *systematic* offset in the derivation of the $L/L_{\rm Edd}$ parameter.

The uncertainties associated with the corrected $M_{\rm BH}$ and $L/L_{\rm Edd}$ values in this work are estimated to be at least $\sim$ 0.3 dex [see Table 2 of 84], but could be much larger ($\sim 0.4 - 0.6$ dex) for high $L/L_{\rm Edd}$ objects such as WLQs (see also, SL15).

5.3. Results and Discussion

5.3.1. Black Hole Masses and Accretion Rates

For the 248 quasars included in this work, we determine the virial Hβ-based $M_{\rm BH,\,corr}$ and corresponding $L/L_{\rm Edd,\,corr}$ values from their derived optical properties, following the Fe II-corrected BELR size-luminosity relation of Equation 5.3, applied to Equations 5.4 and 5.5. We also calculate these quasars' $M_{\rm BH}$ and $L/L_{\rm Edd}$ values following the traditional BELR size-luminosity relation of Equation 5.2 to compare the two methods for estimating black-hole masses and accretion rates.

Figure 5.1 presents the traditional versus corrected $M_{\rm BH}$ and $L/L_{\rm Edd}$ values for the quasars in our sample, that are found following the procedure of [84].

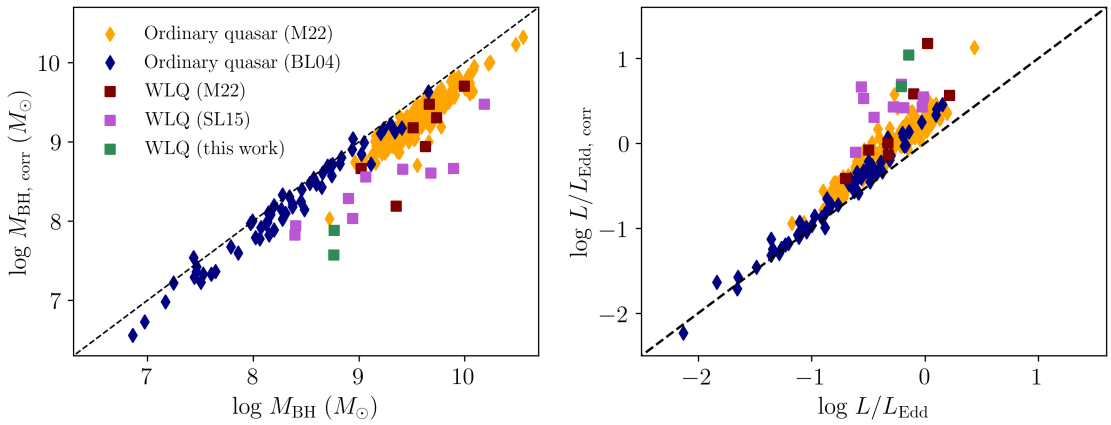

Figure 5.1 Black-hole mass (left panel) and accretion rate (right panel) calculated using the traditional (x-axis) and $R_{\rm Fe\,II}$-corrected (y-axis) BELR size-luminosity relation for all quasars in our analysis. Diamonds mark ordinary quasars and squares mark WLQs. The dashed lines represent a one-to-one relation between the two methods. The traditional relation overestimates $M_{\rm BH}$ in rapidly-accreting quasars by roughly an order of magnitude. In turn, the traditional relation underestimates $L/L_{\rm Edd}$ by a similar factor. In particular, the $R_{\rm Fe\,II}$-corrected accretion rates are much larger for a considerably larger fraction of sources in the WLQ subset than in the ordinary quasars, due to their larger $R_{\rm Fe\,II}$ values.

The Hβ-based $M_{\rm BH,\,corr}$ values of ordinary quasars show small systematic deviations from the traditional BELR size-luminosity relation estimates (less than a factor of two for 222 out of 230 quasars). On the other hand, for a majority of the WLQs, due to the relative weakness in Hβ emission compared to Fe II, $M_{\rm BH,\,corr}$ values deviate significantly from the traditional relation, by up to one order of magnitude. Since $L/L_{\rm Edd}$ is inversely proportional to $M_{\rm BH}$, the $L/L_{\rm Edd,\,corr}$ values are enhanced by a similar factor. This result is in line with the [84] finding of a larger deviation from the one-to-one relation in high-accretion-rate quasars.

5.3.2. The Anti-correlation between EW(C IV) and $L/L_{\rm Edd}$

We use our sample to explore the anti-correlation between EW(C IV) and Hβ-based $L/L_{\rm Edd}$ previously studied in SL15, as well as with $L/L_{\rm Edd,\,corr}$. Figure 5.2 shows EW(C IV) plotted against the traditional $L/L_{\rm Edd}$ values (left) and against the Fe II-corrected

$L/L_{\mathrm{Edd,\,corr}}$ values (right). The first four rows of Table 5.3 present the respective Spearman-rank correlation coefficients (r_S) and chance probabilities (p) of the ordinary quasar sample and the complete sample, including WLQs, for the correlation involving EW(C IV). We detect significant anti-correlations between EW(C IV) and L/L_{Edd} both with and without WLQs (i.e., $p \ll 1\%$). However, the anti-correlation for the sample including WLQs is slightly weaker than without WLQs (both p values are roughly similar, but r_S increases slightly). Our result reaffirms findings by SL15, who found WLQs to be outliers in this relation.

With a Fe II correction, the $L/L_{\mathrm{Edd,\,corr}}$ values provide a significantly stronger anti-correlation with EW(C IV) as the r_S value decreases from -0.36 (for the L/L_{Edd} case) to -0.48. Furthermore, the inclusion of WLQs no longer spoils the Spearman-rank correlation; in fact, the p value remains extremely low ($p = 4.02 \times 10^{-20}$ for the entire sample), and the r_S value decreases from -0.48 to -0.54, indicative of a stronger anti-correlation. Nevertheless, the $L/L_{\mathrm{Edd,\,corr}}$ values of most of the WLQs in our sample still appear considerably smaller than a linear model would suggest (see Figure 5.2). To quantify the deviation of WLQs from the MBE, we fit a simple linear model, without considering the errors, to the log EW(C IV) and log $L/L_{\mathrm{Edd,\,corr}}$ values of the ordinary quasar sample. Our WLQs deviate from the best-fit model by a mean of $\sim 3.4\sigma$, with a range in deviation from 1.08σ to 8.02σ. Such a discrepancy paints WLQs as significant outliers in this correlation.

We also explore whether a bolometric luminosity correction based on the peculiarity of WLQs could account for this discrepancy. Although several methods for correcting bolometric luminosity are available in the literature [e.g., 121, 96, 128, 97], if WLQs were to be reliably predicted by the MBE, these corrections must be up to $\sim 10^5$ times larger than those of [85] (as in the case of SDSS J1141+0219 with EW(C IV) = 0.4 Å). Such a discrepancy is larger than the difference expected by any of the current bolometric correction methods in the literature. These results reveal that EW(C IV) is likely not the sole indicator of accretion rate in all quasars, in agreement with SL15.

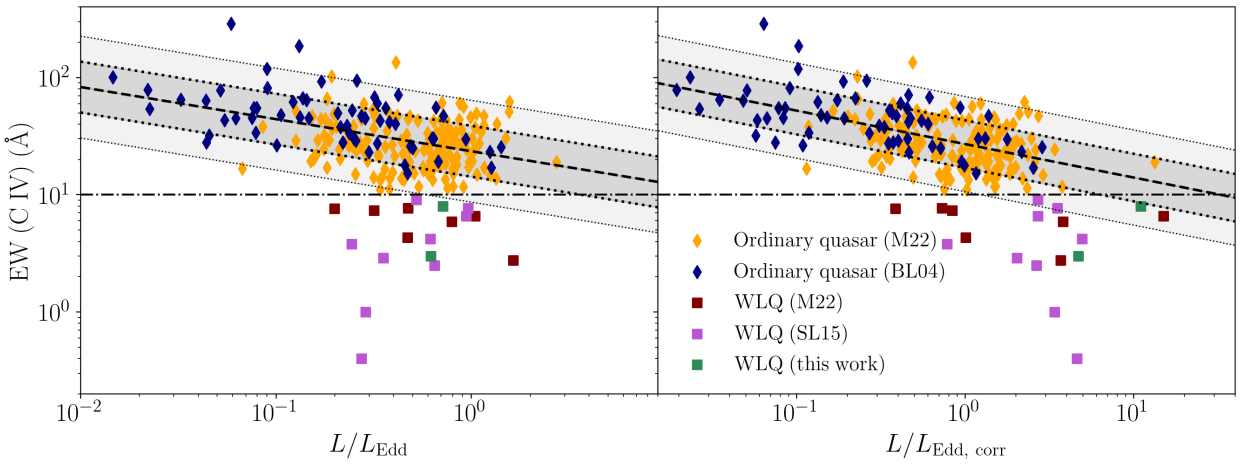

Figure 5.2 Correlation between EW(C IV) and $L/L_{\rm Edd}$ of ordinary quasars (diamonds) and WLQs from Table 5.4 (squares). The left panel presents the traditional $L/L_{\rm Edd}$ values, and the right panel displays the Fe II-corrected $L/L_{\rm Edd,\ corr}$ values. The dotted-dashed lines represent the EW threshold for quasars, below which objects are defined as WLQs. The correlation for the ordinary quasar sample, obtained by fitting a linear model, is shown as a dashed line. The shaded regions represent the 1- and 2-σ deviation from the fitted correlation. Correcting the traditional $L/L_{\rm Edd}$ values results in a stronger anti-correlation expected by the MBE (see Table 5.3); however, WLQs' $L/L_{\rm Edd,\ corr}$ values are still considerably (more than an order of magnitude) over-predicted by the MBE, suggesting that EW(C IV) is not the sole indicator of quasars' accretion rates.

5.3.3. The C IV || Distance as an Indicator of $L/L_{\rm Edd}$

[125] used an independent component analysis (ICA) technique to analyze the spectral properties of the C IV emission line in 133 quasars from the SDSS-RM project [139]. In particular, they fitted a curve to trace the positions of these sources on the EW(C IV) and the Blueshift(C IV) plane. The position of a quasar projected onto this curve is defined as its 'C IV || Distance' (for more details on how this parameter is calculated, see R22). This parameter essentially indicates the location along a non-linear first principal component of the C IV parameter space, and encodes information about the physics of the C IV-emitting gas [e.g., 120, 122, 51].

The left panel of Figure 5.3 shows the distribution of EW(C IV) versus Blueshift(C IV) of the 248 quasars in our sample. The right panel of Figure 5.3 shows the same distribution in scaled space, following the procedure in R22, and the piece-wise polynomial best-fit curve from Figure 2 of R22. Even though our sources are drawn from samples that are different from those of R22, the best-fit curve traces the C IV parameter space of sources across wide ranges of redshifts and luminosities. Since all quasars in our sample are selected photometrically, either in optical (for GNIRS-DQS quasars) or UV (for BL04 quasars) surveys, and were not selected based on their spectroscopic characteristics, there are no known biases associated with their selection, and thus they are expected to trace the C IV parameter space in a similar manner to larger samples of quasars in other studies [e.g., see also 119].

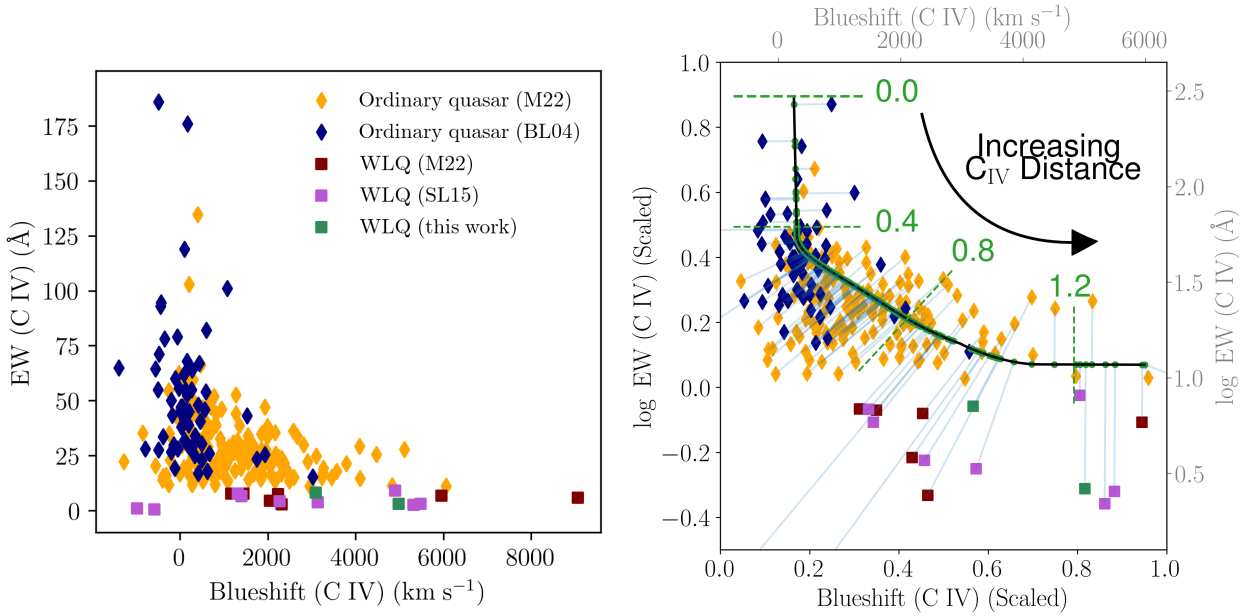

Figure 5.3 Left panel: distribution of EW(C IV) versus Blueshift(C IV) for our sample. Right panel: illustration of the C IV || Distance parameter. The data are first scaled so that the two axes share the same limit, then each data point is projected onto the best-fit curve obtained from R22. The C IV || Distance value of each quasar is defined as its projected position (green point) along the solid black curve. Three of the WLQs are out-of-range in the right panel, but only their projected positions onto the curve are relevant to our results.

While the EW(C IV) parameter, on its own, is not an ideal accretion-rate indicator, the C IV || Distance parameter appears to provide a robust indication of the accretion rates for all quasars including WLQs. We plot the C IV || Distance versus Hβ-based $L/L_{\rm Edd}$ (left) and $L/L_{\rm Edd,\,corr}$ (right) for all quasars in our sample in Figure 5.4. The last four rows of Table 5.3 provide the Spearman-rank correlation coefficients and chance probabilities for the correlations involving the C IV || Distance. Both the $L/L_{\rm Edd}$ and $L/L_{\rm Edd,\,corr}$ are significantly correlated with the C IV || Distance parameter (i.e., $p \ll 1\%$).

In the case of C IV || Distance versus $L/L_{\rm Edd,\,corr}$, the correlation coefficient is considerably larger than the correlation involving $L/L_{\rm Edd}$ (0.56 versus 0.36), indicating the importance of the Fe II correction to $M_{\rm BH}$. Furthermore, the inclusion of WLQs in the sample both strengthens the correlation ($r_{\rm S}$ increases from 0.51 to 0.56 while the p value remains extremely small, $< 10^{-16}$), and allows the high-$L/L_{\rm Edd,\,corr}$ end of the correlation to be fully populated. There is also no significant deviation of the WLQs from this correlation, as opposed to their behavior in the MBE (see, Figure 5.2) as well as in the C IV || Distance versus traditional $L/L_{\rm Edd}$ (see left panel of Figure 5.4). To quantify this effect, we fit a linear model to the C IV || Distance and $L/L_{\rm Edd}$ ($L/L_{\rm Edd,\,corr}$) space, taken into account only the ordinary quasars. Then, we calculate the mean scatter of the WLQs from this line. In the case of $L/L_{\rm Edd}$, we find the deviation from the best-fit line to range from 0.97σ to 3.00σ, and the mean deviation to be $\sim 1.8\sigma$. Meanwhile, the deviation in the case of $L/L_{\rm Edd,\,corr}$ ranges from 0.01σ to 2.33σ, with a mean deviation of $\sim 1.1\sigma$. Thus, using $L/L_{\rm Edd,\,corr}$ not only results in a stronger correlation with C IV || Distance, but C IV || Distance also serves as a better predictor for $L/L_{\rm Edd,\,corr}$ than for $L/L_{\rm Edd}$.

The right panel of Figure 5.4 shows that WLQs are not a disjoint subset of quasars in the UV−optical space [see also, 87]. Our results indicate that WLQs possess high accretion rates, due not only to their extremely weak C IV lines, but also in their relatively large values of the C IV || Distance parameter. Similarly, we observe quasars with high accretion rates (and large values of C IV || Distance) that do not necessarily possess extremely weak C IV lines, some of which have Eddington ratios that are larger than those of several WLQs.

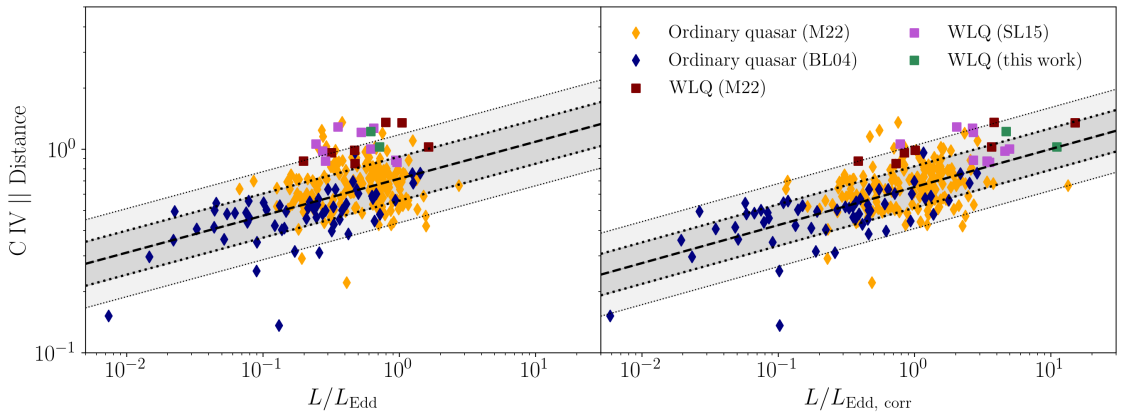

Figure 5.4 C IV || Distance versus $L/L_{\rm Edd}$ of 248 quasars in our sample. In the left panel, the C IV || Distance values are plotted against the traditional Hβ-based $L/L_{\rm Edd}$ parameter, and in the right panel, against the Fe II-corrected Hβ-based $L/L_{\rm Edd,\,corr}$ parameter. The correlation for the ordinary quasar sample, obtained by fitting a linear model, is shown as a dashed line. The shaded regions represent the 1- and 2-σ deviation from the fitted correlation. While using the traditional size-luminosity relation to estimate accretion rates already yields a strong correlation, the Fe II-corrected accretion rates show a much stronger correlation with the C IV || Distance parameter for *all* quasars. Furthermore, this parameter serves as a better predictor for $L/L_{\rm Edd,\,corr}$ than for $L/L_{\rm Edd}$.

Finally, while we are unaware of a large population of quasars that deviate significantly from the correlations of Figure 5.4, a future examination of, e.g., Hβ-based $L/L_{\rm Edd}$ values of quasars with very large EW(C IV) [e.g., 46] is warranted to further test our results.

In this work, we show that the C IV and Hβ parameter space provides important diagnostics for quasar physics. In particular, we found that the C IV || Distance can serve as a robust predictor of quasar's accretion rate, especially after a correction based on $R_{\rm Fe\,II}$ is applied. Within the limits of our sample, we also find that WLQs are not a disjoint subset of the Type 1 quasar population, but instead lie preferentially towards the extreme end of the C IV-Hβ parameter space.

5.4. Conclusions

We compile a statistically meaningful sample of ordinary quasars and WLQs to study the dependence of quasar accretion rates, corrected for the relative strength of Fe II emission with respect to Hβ, upon source location in the C IV parameter space. Utilizing 18 WLQs, 16 of which are obtained from the literature and two of which are presented in this work, we confirm the findings of [84] that the traditional approach to estimating the Eddington ratio for rapidly-accreting quasars systematically underestimates this property by up to an order of magnitude compared to Fe II-corrected values of this parameter.

Using the Fe II-corrected values of Hβ-based $L/L_{\rm Edd}$, we investigate the correlation between this parameter and the C IV parameter space. We confirm and strengthen the SL15 results by finding that WLQs spoil the anti-correlation between EW(C IV) and Hβ-based $L/L_{\rm Edd}$ for quasars, whether the latter parameter is estimated using the traditional method, or whether a correction based on Fe II emission is employed in the $M_{\rm BH}$ estimate. In keeping with SL15, we conclude that the EW(C IV) cannot be the sole indicator of accretion rate in quasars.

We also investigate the relationships between a recently-introduced parameter, the C IV || Distance, which is a combination of EW(C IV) and Blueshift(C IV), and the traditional Hβ-based $L/L_{\rm Edd}$ and the Fe II-corrected $L/L_{\rm Edd,\,corr}$. Such relationships yield strong correlations, especially in the case of Fe II-corrected $L/L_{\rm Edd,\,corr}$, and can accommodate *all* the quasars in our sample. Our finding suggests that WLQs are not a disjoint subset of sources from the general population of quasars. We find that many WLQs have extremely high accretion rates which is indicated by their preferentially higher values of the C IV || Distance parameter. Similarly, we find several quasars in our sample that possess high Eddington ratios, and correspondingly large values of the C IV || Distance, that do not have extremely weak C IV lines; some of these sources display Eddington ratios that are larger than those of a subset of our WLQs.

In the context of the C IV parameter space, it will be interesting to investigate whether the extreme X-ray properties of WLQs are the result of extremely large C IV || Dis-

tance values rather than resulting only from extremely weak C IV lines. Such a test would require X-ray coverage of a large sample of sources with Hβ+Fe II data across the widest possible C IV parameter space such as the GNIRS-DQS sample of M22. It would also be useful to determine whether the weakness of the broad Lyα+N V emission line complex (from which the first high-redshift WLQs were identified) also correlates with C IV || Distance, which will require ultraviolet spectroscopy [110]. The results of these investigations will shed new light on the connection between the quasar accretion rate and the physics of the inner accretion disk and BELR.

This work is supported by National Science Foundation (NSF) grants AST-1815281 (B.M.M., O.S., C.D.), AST-1815645 (M.S.B., A.D.M.). G.T.R. was supported in part by NASA through a grant (HST-AR-15048.001-A) from the Space Telescope Science Institute, which is operated by the Association of Universities for Research in Astronomy, Incorporated, under NASA contract NAS5-26555. W.N.B. acknowledges support from NSF grant AST-2106990. B.L. acknowledges financial support from the National Natural Science Foundation of China grant 11991053. B.T. acknowledges support from the European Research Council (ERC) under the European Union's Horizon 2020 research and innovation program (grant agreement 950533) and from the Israel Science Foundation (grant 1849/19). This research has made use of the NASA/IPAC Extragalactic Database (NED), which is operated by the Jet Propulsion Laboratory, California Institute of Technology, under contract with the National Aeronautics and Space Administration.

Table 5.1. Basic Properties of the WLQ Sample

Quasar	z_{sys}	$\log \nu L_\nu$(5100 Å) (erg s^{-1})	FWHM(Hβ) (km s^{-1})	$R_{\rm Fe\,II}$	$log\ M_{\rm BH}$ ($M_\odot$)	$\log M_{\rm BH,\,corr}$ ($M_\odot$)	$L/L_{\rm Edd}$	$L/L_{\rm Edd,\,corr}$	EW(C IV) (Å)	Blueshift(C IV) (km s^{-1})	Optical Ref.[a]	C IV Ref.[a]
(1)	(2)	(3)	(4)	(5)	(6)	(7)	(8)	(9)	(10)	(11)	(12)	(13)
SDSS J010643.23−031536.4	2.248	46.51	6782	0.58	9.99	9.71	0.20	0.39	$7.6^{+0.6}_{-0.9}$	1451^{+119}_{-60}	1	2
SDSS J013136.44+130331.0	1.599	46.45	2294	0.78	9.02	8.67	1.63	3.67	$2.8^{+1.4}_{-2.0}$	2320^{+819}_{-521}	1	2
SDSS J013417.81−005036.2	2.270	46.45	5211	0.98	9.73	9.31	0.32	0.84	$7.3^{+0.7}_{-1.0}$	2233^{+651}_{-414}	1	2
SDSS J075115.43+505439.1	2.311	46.59	3077	3.05	9.35	8.19	1.05	15.04	$6.6^{+0.6}_{-1.0}$	5953^{+234}_{-117}	1	2
SDSS J083650.86+142539.0	1.749	45.93	2880	2.48	8.94	8.04	0.62	4.95	$4.2^{+0.3}_{-0.5}$	2266 ± 191	3	3
SDSS J085337.36+121800.3	2.197	46.56	4502	0.28	9.66	9.48	0.47	0.73	$7.7^{+1.1}_{-1.7}$	1166^{+363}_{-242}	1	2
SDSS J085344.17+354104.5	2.183	46.40	4168	0.72	9.51	9.18	0.47	1.00	$4.3^{+0.8}_{-1.2}$	2053^{+1580}_{-1094}	1	2
SDSS J094533.98+100950.1	1.683	46.17	4278	2.00	9.41	8.66	0.35	2.03	$2.9^{+0.3}_{-0.6}$	5485 ± 380	3	3
SDSS J094602.31+274407.0	2.488	46.75	3833	1.65	9.63	8.94	0.79	3.82	$5.9^{+0.4}_{-0.6}$	9062^{+16}_{-11}	1	2
SDSS J113747.64+391941.5	2.428	45.81	2518	3.31	8.76	7.57	0.72	10.99	8^{+6}_{-9}	3089^{+2050}_{-1236}	4	4
SDSS J114153.33+021924.4	3.550	46.55	5900	3.25	9.89	8.67	0.27	4.60	0.4^{+2}_{-4}	-577^{+2461}_{-1484}	5	6,4
SDSS J123743.07+630144.7	3.490	46.35	5200	2.86	9.68	8.61	0.29	3.39	1 ± 2	-970^{+1349}_{-845}	5	4
SDSS J141141.96+140233.9	1.754	45.64	3966	1.41	9.06	8.56	0.24	0.78	$3.8^{+0.8}_{-0.2}$	3142^{+370}_{-208}	1	2
SDSS J141730.92+073320.7	1.716	45.91	2784	1.65	8.90	8.29	0.65	2.64	$2.5^{+2.1}_{-0.7}$	5321^{+4178}_{-872}	1	2
SDSS J144741.76˜020339.1	1.430	45.56	1923	1.60	8.39	7.83	0.96	3.52	$7.7^{+0.2}_{-1.3}$	1319^{+759}_{-381}	1	2
SDSS J152156.48+520238.5	2.190	47.14	5750	1.64	10.19	9.48	0.52	2.69	9.1 ± 0.6	4900 ± 300 [b]	7	7
SDSS J213742.25−003912.7	2.294	45.75	2630	2.45	8.77	7.89	0.62	4.68	3^{+1}_{-2}	4986^{+867}_{-535}	4	4
PHL 1811	0.192	45.56	1943	1.29 [c]	8.40	7.94	0.94	2.70	6.6	1400 ± 250	8	8

[a]Source of rest-frame optical–UV data, Column (12): z_{sys}, νL_ν(5100 Å), FWHM(Hβ), $R_{\rm Fe\,II}$; Column (13): EW(C IV), and Blueshift(C IV). (1) M22; (2) D22; (3) [116]; (4) this work; (5) [136]; (6) [144]; (7) [168];(8) [78].

[b][168] also reported Hβ-based Blueshift(C IV) = 9400 km s^{-1}. Here, we have opted to use a Mg II-based value of Blueshift(C IV).

[c][78] reported the $R_{\rm Fe\,II}$ value as being in the range 1.22−1.35. We have adopted a mean value of 1.29 for this work.

Table 5.2. Basic Properties of the Ordinary Quasar Sample

Quasar	z_{sys}	$\log \nu L_\nu$(5100 Å) (erg s^{-1})	FWHM(Hβ) (km s^{-1})	$R_{\rm Fe\,II}$	$log\ M_{\rm BH}$ ($M_\odot$)	$\log M_{\rm BH,\,corr}$ ($M_\odot$)	$L/L_{\rm Edd}$	$L/L_{\rm Edd,\,corr}$	EW(C IV) (Å)	Blueshift(C IV) (km s^{-1})	Optical Ref.[a]	C IV Ref.
(1)	(2)	(3)	(4)	(5)	(6)	(7)	(8)	(9)	(10)	(11)	(12)	(13)
PG 0003+199	0.026	44.07	1640	0.62	7.46	7.36	0.33	0.41	60.1[b]	−102	3	4
SDSS J001018.88+280932.5	1.613	46.27	3189	0.06	9.21	9.13	0.70	0.86	$61.0^{+0.5}_{-0.8}$	203^{+22}_{-15}	1	2
SDSS J001453.20+091217.6	2.335	46.36	6428	0.72	9.87	9.54	0.19	0.40	$39.0^{+3.3}_{-5.0}$	825^{+397}_{-266}	1	2
SDSS J001813.30+361058.6	2.324	46.46	4896	0.55	9.68	9.41	0.36	0.68	$25.8^{+1.1}_{-1.6}$	1885^{+203}_{-136}	1	2
SDSS J001914.46+155555.9	2.267	46.34	4033	0.17	9.45	9.32	0.47	0.64	$44.5^{+0.9}_{-1.3}$	372^{+110}_{-74}	1	2
PG 0026+129	0.145	45.13	1860	0.51	8.13	7.98	0.68	0.95	19.3	−120	3	4
SDSS J002634.46+274015.5	2.247	46.38	4420	0.00	9.55	9.48	0.41	0.49	$134.6^{+10.1}_{-15.0}$	400^{+416}_{-279}	1	2
SDSS J003001.11-015743.5	1.590	46.10	4028	0.26	9.32	9.18	0.37	0.52	$52.7^{+1.9}_{-2.8}$	1279^{+139}_{-93}	1	2
SDSS J003416.61+002241.1	1.630	46.24	5527	0.44	9.67	9.46	0.23	0.38	$28.5^{+0.3}_{-0.5}$	483^{+86}_{-58}	1	2
SDSS J003853.15+333044.3	2.361	46.39	4297	0.50	9.53	9.28	0.44	0.78	$13.8^{+1.0}_{-1.5}$	-398^{+950}_{-637}	1	2

[a]Source of rest-frame optical–UV data, Column (12): z_{sys}, νL_ν(5100 Å), FWHM(Hβ), $R_{\rm Fe\,II}$; Column (13): EW(C IV), and Blueshift(C IV). (1) M22; (2) D22; (3) [19]; (4) [9].

[b]There are no errors reported for EW(C IV) and Blueshift(C IV) values for PG quasars in [9].

Note. — Only the first ten lines are shown; the entire table will be available in the electronic version.

Table 5.3. Spearman-Rank Correlation Coefficients

Correlation	Sample	N	r_S	p
EW(C IV)-L/L_{Edd}	Ordinary	230	−0.36	1.39×10^{-8}
EW(C IV)-L/L_{Edd}	All	248	−0.35	1.10×10^{-8}
EW(C IV)-$L/L_{Edd,\,corr}$	Ordinary	230	−0.48	6.82×10^{-15}
EW(C IV)-$L/L_{Edd,\,corr}$	All	248	−0.54	4.02×10^{-20}
C IV ‖ Distance-L/L_{Edd}	Ordinary	230	0.37	6.66×10^{-9}
C IV ‖ Distance-L/L_{Edd}	All	248	0.36	4.66×10^{-9}
C IV ‖ Distance-$L/L_{Edd,\,corr}$	Ordinary	230	0.51	8.40×10^{-17}
C IV ‖ Distance-$L/L_{Edd,\,corr}$	All	248	0.56	8.96×10^{-22}

Note. — The last three columns represent the number of sources in each correlation, the Spearman-rank correlation coefficient, and the chance probability, respectively.

Table 5.4. *Gemini-North* GNIRS *H*-Band Observation Log

Quasar (SDSS J)	z[a]	z_{sys}[b]	$\log \nu L_\nu$ (5100 Å) (erg s^{-1})	Observation Dates	Exp. Time (s)
113747.64+391941.5	2.420	2.428	45.8	2014 Mar 14, 20	7140
213742.25−003912.7	2.281	2.294	45.8	2014 Jun 29, Aug 04	7040

[a]Obtained from visually-inspected redshifts (zvis) reported in SDSS Data Release 16 [82]

[b]Systemic redshifts (see § 5.5 for details).

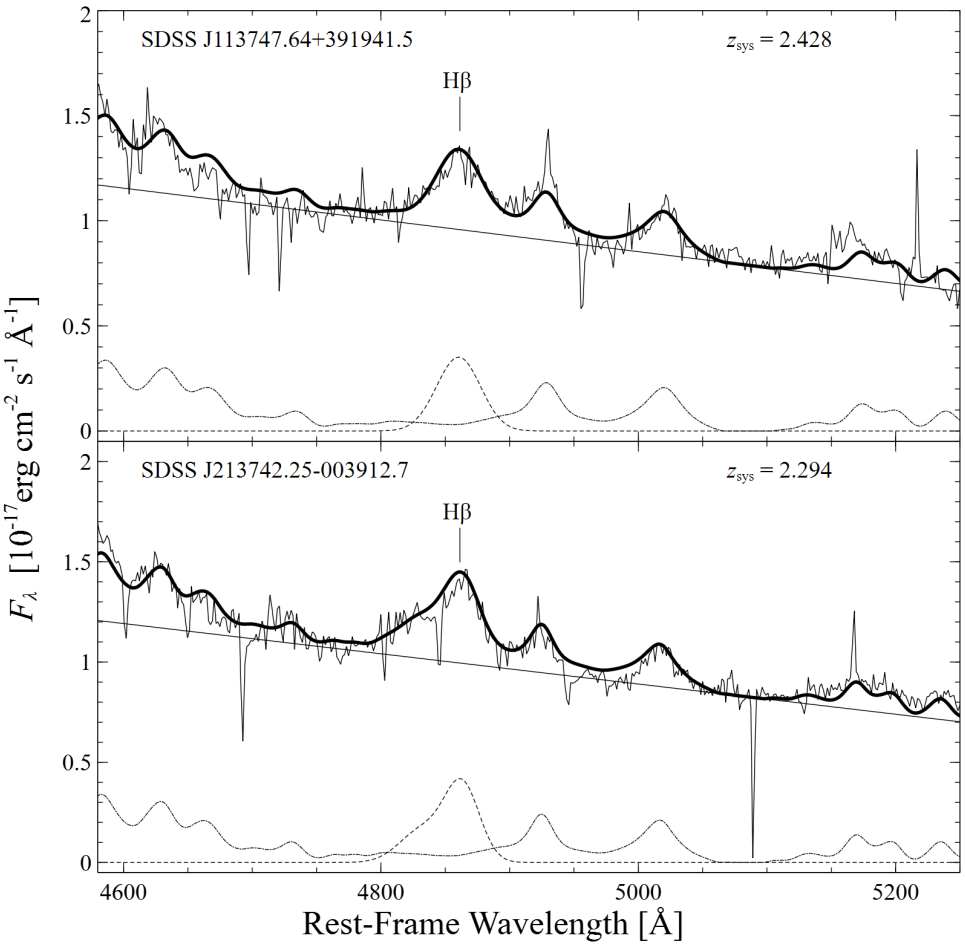

Figure 5.5 The NIR spectra of SDSS J1137+3919 (top) and SDSS J2137−0039 (bottom). In each panel, the continuous line is the observed spectrum of each quasar. The continuous straight line below the spectrum is the linear continuum fit. The dashed line is the Hβ λ4861 profile modelled with two Gaussians. The dotted-dashed line is the Fe II template from [19], which was broadened by 1500 km s^{-1} for SDSS J1137+3919, and 1400 km s^{-1} for J2137−0039. The bold solid line is the entire fitted spectrum.

5.5. Appendix: NIR Spectroscopy of SDSS J1137+3919 and SDSS J2137−0039

SDSS J113747.64+391941.5 and SDSS J213742.25−003912.7 (hereafter, SDSS J1137+3919 and SDSS J2137−0039, respectively) are two WLQs with redshifts suitable for observing the Hβ line in the *H*-Band. Observations of these quasars were carried out by the *Gemini-North* Observatory using GNIRS throughout four observing runs between 2014 March

14 and 2014 August 4, under program GN-2014A-Q-47. The observation log appears in Table 5.4. For both targets, we used the Short Blue Camera, with spatial resolution 0.″15 pix^{-1}, and a 1.0″ slit to achieve a spectral resolution of $R \sim 600$. An H-filter was applied, producing a spectral range of 1.5 - 1.8 μm, corresponding to rest-frame $\sim 4500-5300$ Å. Exposure times for each subintegration were 238 s and 220 s, and the total integration times were 7140 s and 7040 s for SDSS J1137+3919 and SDSS J2137−0039, respectively. These observations were performed using the standard "ABBA" nodding pattern of the targets along the slit in order to obtain primary background subtraction.

The spectra were processed using the standard procedure of the IRAF *Gemini* package based on the PyRAF Python-based interface. Exposures from the same nodding position were added to boost the signal-to-noise ratio, then the sum of exposures from two different nodding positions were subtracted to remove background noise. Wavelength calibration was done against an Argon lamp in order to assign wavelength values to the observed pixels.

Spectra of telluric standard stars with $T_{eff} \sim 9700$ K were taken immediately before or after the science exposures to remove telluric absorption features in the quasars' observed spectra. These spectra were processed in a similar fashion, followed by a removal of the stars' intrinsic hydrogen absorption lines by fitting a Lorentzian profile to each hydrogen absorption line, and interpolating across this feature to connect the continuum on each side of the line. The quasars' spectra were divided by the corrected stellar spectra. The corrected quasar spectra were then multiplied by an artificial blackbody curve with a temperature corresponding to the telluric standard star, which yielded a cleaned, observed-frame quasar spectrum.

Flux calibrations were obtained by taking the Wide-field Infrared Survey Explorer [WISE; 166] $W1$-band (at 3.4 μm) apparent magnitudes, reported by SDSS Data Release 16 [82], and the $W1$ isophotal flux density F_λ(iso) given in Table 1 of [65]. Flux densities at 3.4 μm were derived according to:

$$F_\lambda(3.4\ \mu m) = F_\lambda(\text{iso}) \cdot 10^{-\text{mag}/2.5}. \tag{5.6}$$

The flux densities at 3.4 μm were extrapolated to flux densities at 1.63 μm, roughly corresponding to λ_{rest} = 5100 Å, assuming an optical continuum of the form $F_\nu \propto \nu^{-0.5}$ [e.g., 156].

We modeled the spectra following the methods of [131] and [136]. Our model consists of a linear continuum through the average flux densities of two narrow (~20 Å) rest-frame bands centered on 4750 Å and 4975 Å, a broadened Fe II emission template [19], and two Gaussian profiles for the Hβ λ4861 emission-line. No [[O III]] emission-lines are detectable in either spectrum, and we placed upper limits on their EWs by fitting a Gaussian feature where the [[O III]] emission-lines should be such that they are indistinguishable from the noise. The final, calibrated near infrared spectra of the two WLQs appear in Figure 5.5.

In both sources we detected weak and relatively narrow Hβ lines as well as strong Fe II features compared to quasars at similar luminosities and redshifts [e.g., see 98, 138]. We also determined the systemic redshifts (z_{sys}) values from the observed-frame wavelength of the peak (λ_{peak}) of the Hβ emission-line, a similar treatment as in [90] for sources that lack [[O III]] emission. The z_{sys} values are larger than the redshifts reported by [82] by Δz = 0.008 in SDSS J1137+3919 and by Δz = 0.013 in SDSS J2137−0039, corresponding to velocity offsets (blueshifts) of 700 km s^{-1} and 1184 km s^{-1}, respectively, which is consistent with typical velocity offsets between SDSS Pipeline redshifts and z_{sys} values observed in luminous, high-redshift quasars [36, M22]. The rest-frame spectra in Figure 5.5 have henceforth been corrected by z_{sys}.

CHAPTER 6

SUMMARY AND CONCLUSIONS

Quasars are the most interesting and powerful lab in the observable universe. Their brightness and compactness drive interesting physical questions as to how black holes accrete mass and evolve with their host galaxy. With 260 of the most detailed, homogeneous NIR spectra of high-redshift quasars, I have improved how we study these objects at high redshifts. In particular, this work uses regression analyses of UV emission line properties in order to improve the measurements and estimates of a quasars' redshift, SMBH mass, and accretion rate at high redshifts.

The improvements made, in Chapters 2 and 3, from mapping UV emission lines onto more reliable optical emission lines may seem trivial at first, however these improvements hold serious implications to our understanding of the universe. For example, the corrections this work makes to the accuracy and precision of redshift estimates from the C IV emission line correspond to $\sim$ 10 Mpc and $\sim$ 2 Mpc improvement, respectively. For context, this correction improves the accuracy of our redshift measurement by over 4 times this size of the local group ($\sim$ 2.5 Mpc). Moreover, this correction provides the scientific community with a simple and easy way of obtaining reliable redshift estimates from rest-frame UV emission lines.

The work pertaining to $M_{\rm BH}$ estimates, detailed in Chapter 4, provides the most up-to-date prescriptions for obtaining single epoch, UV-based $M_{\rm BH}$ estimates. This work is crucial for understanding many of the interactions at play between a SMBH and its host galaxy, such as the $M_{\rm BH} - L_{bulge}$ and $M_{\rm BH} - \sigma_*$ relations. Additionally, these prescriptions are going to become necessary to study SMBHs as multi-epoch observations of these objects will become increasingly difficult and expensive at high redshifts. The corrections I make to rest-frame UV-based $M_{\rm BH}$ estimates completely corrects on overestimation of a factor of 2 and improves the precision of these estimates, slightly, when compared to the more accurate Hβ-based $M_{\rm BH}$ estimates.

The investigation of accretion rate indicators presented in Chapter 5 provides an intriguing avenue to explore as we observe and understand quasars. From this investigation, I find that weak line quasars do not necessarily deviate as much as we may have previously expected. Namely, by studying these objects throughout their C IV parameter space, we find that the C IV || Distance actually allows us to reliably evaluate the accretion rate of these weak line objects. Additionally, this accretion rate estimate we obtain from the C IV || Distance is a general improvement when compared to the traditional Modified Baldwin Effect, which utilizes only the C IV EW.

The works compiled here illustrate the importance of accuracy and precision as we venture into the era of big data in astronomy. Around 15 to 20 years ago, a study like this was only dreamed of and broad estimates of these parameters was sufficient. However, now we are on the cusp of having millions of more high redshift quasar observations and now is the time to make sure that the measurements that we obtain from these objects will be as reliable as possible. The work completed in this dissertation is merely a stepping stone for future science as we still push to observe quasars at higher and higher redshifts. As we look into the future of quasar observations, we, as a community, will require more high redshift multi-wavelength analyses similar to the ones presented in this work.

REFERENCES

[1] C. Alcock and B. Paczynski, *An evolution free test for non-zero cosmological constant*, Nature281 (1979), 358.

[2] Scott F. Anderson, Xiaohui Fan, Gordon T. Richards, Donald P. Schneider, Michael A. Strauss, Daniel E. Vanden Berk, James E. Gunn, Gillian R. Knapp, David Schlegel, Wolfgang Voges, Brian Yanny, Neta A. Bahcall, Mariangela Bernardi, J. Brinkmann, Robert Brunner, Istvan Csabái, Mamoru Doi, Masataka Fukugita, G. S. Hennessy, Željko Ivezić, Peter Z. Kunszt, Donald Q. Lamb, Jon Loveday, Robert H. Lupton, Timothy A. McKay, Jeffrey A. Munn, R. C. Nichol, G. P. Szokoly, and Donald G. York, *High-Redshift Quasars Found in Sloan Digital Sky Survey Commissioning Data. VI. Sloan Digital Sky Survey Spectrograph Observations*, AJ122 (2001), no. 2, 503–517.

[3] R. J. Assef, K. D. Denney, C. S. Kochanek, B. M. Peterson, S. Kozłowski, N. Ageorges, R. S. Barrows, P. Buschkamp, M. Dietrich, E. Falco, C. Feiz, H. Gemperlein, A. Germeroth, C. J. Grier, R. Hofmann, M. Juette, R. Khan, M. Kilic, V. Knierim, W. Laun, R. Lederer, M. Lehmitz, R. Lenzen, U. Mall, K. K. Madsen, H. Mandel, P. Martini, S. Mathur, K. Mogren, P. Mueller, V. Naranjo, A. Pasquali, K. Polsterer, R. W. Pogge, A. Quirrenbach, W. Seifert, D. Stern, B. Shappee, C. Storz, J. Van Saders, P. Weiser, and D. Zhang, *Black Hole Mass Estimates Based on C IV are Consistent with Those Based on the Balmer Lines*, ApJ742 (2011), no. 2, 93.

[4] E. Bañados, B. P. Venemans, R. Decarli, E. P. Farina, C. Mazzucchelli, F. Walter, X. Fan, D. Stern, E. Schlafly, K. C. Chambers, H. W. Rix, L. Jiang, I. McGreer, R. Simcoe, F. Wang, J. Yang, E. Morganson, G. De Rosa, J. Greiner, M. Baloković, W. S. Burgett, T. Cooper, P. W. Draper, H. Flewelling, K. W. Hodapp, H. D. Jun, N. Kaiser, R. P. Kudritzki, E. A. Magnier, N. Metcalfe, D. Miller, J. T. Schindler, J. L. Tonry, R. J. Wainscoat, C. Waters, and Q. Yang, *The Pan-STARRS1 Distant z > 5.6 Quasar Survey: More than 100 Quasars within the First Gyr of the Universe*, ApJS227 (2016), no. 1, 11.

[5] Jack A. Baldwin, *Luminosity Indicators in the Spectra of Quasi-Stellar Objects*, ApJ214 (1977), 679–684.

[6] Dong-Wei Bao, Michael S. Brotherton, Pu Du, Jacob N. McLane, T. E. Zastrocky, Kianna A. Olson, Feng-Na Fang, Shuo Zhai, Zheng-Peng Huang, Kai Wang, Bi-Xuan Zhao, Sha-Sha Li, Sen Yang, Yong-Jie Chen, Jun-Rong Liu, Zhu-Heng Yao, Yue-Chang Peng, Wei-Jian Guo, Yu-Yang Songsheng, Yan-Rong Li, Bo-Wei Jiang, David H. Kasper, William T. Chick, My L. Nguyen, Jaya Maithil, H. A. Kobulnicky, D. A. Dale, Derek Hand, C. Adelman, Z. Carter, A. M. Murphree, M. Oeur, S. Schonsberg, T. Roth, Hartmut Winkler, Paola Marziani, Mauro D'Onofrio, Chen Hu, Ming Xiao, Suijian Xue, Bożena Czerny, Jesús Aceituno, Luis C. Ho, Jin-Ming Bai, Jian-Min Wang, and MAHA Collaboration, *Monitoring AGNs with Hβ Asymmetry. III. Long-term Reverberation Mapping Results of 15 Palomar-Green Quasars*, ApJS262 (2022), no. 1, 14.

[7] Aaron J. Barth, Vardha N. Bennert, Gabriela Canalizo, Alexei V. Filippenko, Elinor L. Gates, Jenny E. Greene, Weidong Li, Matthew A. Malkan, Anna Pancoast, David J. Sand, Daniel Stern, Tommaso Treu, Jong-Hak Woo, Roberto J. Assef, Hyun-Jin Bae, Brendon J. Brewer, S. Bradley Cenko, Kelsey I. Clubb, Michael C. Cooper, Aleksandar M. Diamond-Stanic, Kyle D. Hiner, Sebastian F. Hönig, Eric Hsiao, Michael T. Kandrashoff, Mariana S. Lazarova, A. M. Nierenberg, Jacob Rex, Jeffrey M. Silverman, Erik J. Tollerud, and Jonelle L. Walsh, *The Lick AGN Monitoring Project 2011: Spectroscopic Campaign and Emission-line Light Curves*, ApJS217 (2015), no. 2, 26.

[8] Alexei Baskin and Ari Laor, *On the origin of the C IV Baldwin effect in active galactic nuclei*, MNRAS350 (2004), no. 2, L31–L35.

[9] ———, *What controls the CIV line profile in active galactic nuclei?*, MNRAS356 (2005), no. 3, 1029–1044.

[10] Mitchell Begelman, Martijn de Kool, and Marek Sikora, *Outflows Driven by Cosmic-Ray Pressure in Broad Absorption Line QSOs*, ApJ382 (1991), 416.

[11] A. S. Bennett, *The revised 3C catalogue of radio sources.*, MmRAS68 (1962), 163.

[12] Misty C. Bentz, Kelly D. Denney, Catherine J. Grier, Aaron J. Barth, Bradley M.

Peterson, Marianne Vestergaard, Vardha N. Bennert, Gabriela Canalizo, Gisella De Rosa, Alexei V. Filippenko, Elinor L. Gates, Jenny E. Greene, Weidong Li, Matthew A. Malkan, Richard W. Pogge, Daniel Stern, Tommaso Treu, and Jong-Hak Woo, *The Low-luminosity End of the Radius-Luminosity Relationship for Active Galactic Nuclei*, ApJ767 (2013), no. 2, 149.

[13] Misty C. Bentz and Sarah Katz, *The AGN Black Hole Mass Database*, PASP127 (2015), no. 947, 67.

[14] Misty C. Bentz, Bradley M. Peterson, Hagai Netzer, Richard W. Pogge, and Marianne Vestergaard, *The Radius-Luminosity Relationship for Active Galactic Nuclei: The Effect of Host-Galaxy Starlight on Luminosity Measurements. II. The Full Sample of Reverberation-Mapped AGNs*, ApJ697 (2009), no. 1, 160–181.

[15] M. S. Bessell, F. Castelli, and B. Plez, *Model atmospheres broad-band colors, bolometric corrections and temperature calibrations for O - M stars*, A&A333 (1998), 231–250.

[16] R. D. Blandford and C. F. McKee, *Reverberation mapping of the emission line regions of Seyfert galaxies and quasars.*, ApJ255 (1982), 419–439.

[17] Adam S. Bolton, David J. Schlegel, Éric Aubourg, Stephen Bailey, Vaishali Bhardwaj, Joel R. Brownstein, Scott Burles, Yan-Mei Chen, Kyle Dawson, Daniel J. Eisenstein, James E. Gunn, G. R. Knapp, Craig P. Loomis, Robert H. Lupton, Claudia Maraston, Demitri Muna, Adam D. Myers, Matthew D. Olmstead, Nikhil Padmanabhan, Isabelle Pâris, Will J. Percival, Patrick Petitjean, Constance M. Rockosi, Nicholas P. Ross, Donald P. Schneider, Yiping Shu, Michael A. Strauss, Daniel Thomas, Christy A. Tremonti, David A. Wake, Benjamin A. Weaver, and W. Michael Wood-Vasey, *Spectral Classification and Redshift Measurement for the SDSS-III Baryon Oscillation Spectroscopic Survey*, AJ144 (2012), no. 5, 144.

[18] Todd Boroson, *Blueshifted [O III] Emission: Indications of a Dynamic Narrow-Line Region*, AJ130 (2005), no. 2, 381–386.

[19] Todd A. Boroson and Richard F. Green, *The Emission-Line Properties of Low-Redshift Quasi-stellar Objects*, ApJS80 (1992), 109.

[20] Volker Bromm and Naoki Yoshida, *The First Galaxies*, ARA&A49 (2011), no. 1, 373–407.

[21] Michael S. Brotherton, J. C. Runnoe, Zhaohui Shang, and M. A. DiPompeo, *Bias in C IV-based quasar black hole mass scaling relationships from reverberation mapped samples*, MNRAS451 (2015), no. 2, 1290–1298.

[22] E. M. Cackett, K. Gültekin, M. C. Bentz, M. M. Fausnaugh, B. M. Peterson, J. Troyer, and M. Vestergaard, *Swift/UVOT Grism Monitoring of NGC 5548 in 2013: An Attempt at MgII Reverberation Mapping*, ApJ810 (2015), no. 2, 86.

[23] Gabriela Canalizo, Margrethe Wold, Kyle D. Hiner, Mariana Lazarova, Mark Lacy, and Kevin Aylor, *Probing the M_BH-σ_* Relation in the Non-local Universe Using Red QSOs*, ApJ760 (2012), no. 1, 38.

[24] Stefano Carniani, R. Maiolino, A. Marconi, G. Venturi, G. Cresci, M. Brusa, A. Fluetsch, A. Ferrara, S. Gallerani, F. Fiore, C. Cicone, S. Ohad, H. Netzer, R. Schneider, B. Balmaverde, T. Nagao, F. La Franca, A. Comastri, F. Mannucci, G. Risaliti, E. Piconcelli, C. Feruglio, M. Cano-Diaz, V. Mainieri, L. Testi, and E. Sani, *AGN-driven outflows in the early Universe*, AGN13: Beauty and the Beast, vol. 13, October 2018, p. 68.

[25] Zhi-Fu Chen, Yi-Ping Qin, Ming Qin, Cai-Juan Pan, and Da-Sheng Pan, *Catalog of Narrow C IV Absorption Lines in BOSS. II. For Quasars with $Z_{em} > 2.4$*, ApJS215 (2014), no. 1, 12.

[26] Zhu Chen, S. M. Faber, David C. Koo, Rachel S. Somerville, Joel R. Primack, Avishai Dekel, Aldo Rodríguez-Puebla, Yicheng Guo, Guillermo Barro, Dale D. Kocevski, A. van der Wel, Joanna Woo, Eric F. Bell, Jerome J. Fang, Henry C. Ferguson, Mauro Giavalisco, Marc Huertas-Company, Fangzhou Jiang, Susan Kassin, Lin Lin, F. S. Liu, Yifei Luo, Zhijian Luo, Camilla Pacifici, Viraj Pandya, Samir Salim, Chenggang Shu, Sandro Tacchella, Bryan A. Terrazas, and Hassen M. Yesuf, *Quenching as a Contest between Galaxy Halos and Their Central Black Holes*, ApJ897 (2020), no. 1, 102.

[27] Liam Coatman, Paul C. Hewett, Manda Banerji, Gordon T. Richards, Joseph F.

Hennawi, and J. Xavier Prochaska, *Correcting C IV-based virial black hole masses*, MNRAS465 (2017), no. 2, 2120–2142.

[28] Matthew J. Collinge, Michael A. Strauss, Patrick B. Hall, Željko Ivezić, Jeffrey A. Munn, David J. Schlegel, Nadia L. Zakamska, Scott F. Anderson, Hugh C. Harris, Gordon T. Richards, Donald P. Schneider, Wolfgang Voges, Donald G. York, Bruce Margon, and J. Brinkmann, *Optically Identified BL Lacertae Objects from the Sloan Digital Sky Survey*, AJ129 (2005), no. 6, 2542–2561.

[29] Elena Dalla Bontà, Bradley M. Peterson, Misty C. Bentz, W. N. Brandt, S. Ciroi, Gisella De Rosa, Gloria Fonseca Alvarez, Catherine J. Grier, P. B. Hall, Juan V. Hernández Santisteban, Luis C. Ho, Y. Homayouni, Keith Horne, C. S. Kochanek, Jennifer I. Hsiu Li, L. Morelli, A. Pizzella, R. W. Pogge, D. P. Schneider, Yue Shen, J. R. Trump, and Marianne Vestergaard, *The Sloan Digital Sky Survey Reverberation Mapping Project: Estimating Masses of Black Holes in Quasars with Single-epoch Spectroscopy*, ApJ903 (2020), no. 2, 112.

[30] Kyle S. Dawson, David J. Schlegel, Christopher P. Ahn, Scott F. Anderson, Éric Aubourg, Stephen Bailey, Robert H. Barkhouser, Julian E. Bautista, Alessandra Beifiori, Andreas A. Berlind, Vaishali Bhardwaj, Dmitry Bizyaev, Cullen H. Blake, Michael R. Blanton, Michael Blomqvist, Adam S. Bolton, Arnaud Borde, Jo Bovy, W. N. Brandt, Howard Brewington, Jon Brinkmann, Peter J. Brown, Joel R. Brownstein, Kevin Bundy, N. G. Busca, William Carithers, Aurelio R. Carnero, Michael A. Carr, Yanmei Chen, Johan Comparat, Natalia Connolly, Frances Cope, Rupert A. C. Croft, Antonio J. Cuesta, Luiz N. da Costa, James R. A. Davenport, Timothée Delubac, Roland de Putter, Saurav Dhital, Anne Ealet, Garrett L. Ebelke, Daniel J. Eisenstein, S. Escoffier, Xiaohui Fan, N. Filiz Ak, Hayley Finley, Andreu Font-Ribera, R. Génova-Santos, James E. Gunn, Hong Guo, Daryl Haggard, Patrick B. Hall, Jean-Christophe Hamilton, Ben Harris, David W. Harris, Shirley Ho, David W. Hogg, Diana Holder, Klaus Honscheid, Joe Huehnerhoff, Beatrice Jordan, Wendell P. Jordan, Guinevere Kauffmann, Eyal A. Kazin, David Kirkby, Mark A.

Klaene, Jean-Paul Kneib, Jean-Marc Le Goff, Khee-Gan Lee, Daniel C. Long, Craig P. Loomis, Britt Lundgren, Robert H. Lupton, Marcio A. G. Maia, Martin Makler, Elena Malanushenko, Viktor Malanushenko, Rachel Mandelbaum, Marc Manera, Claudia Maraston, Daniel Margala, Karen L. Masters, Cameron K. McBride, Patrick McDonald, Ian D. McGreer, Richard G. McMahon, Olga Mena, Jordi Miralda-Escudé, Antonio D. Montero-Dorta, Francesco Montesano, Demitri Muna, Adam D. Myers, Tracy Naugle, Robert C. Nichol, Pasquier Noterdaeme, Sebastián E. Nuza, Matthew D. Olmstead, Audrey Oravetz, Daniel J. Oravetz, Russell Owen, Nikhil Padmanabhan, Nathalie Palanque-Delabrouille, Kaike Pan, John K. Parejko, Isabelle Pâris, Will J. Percival, Ismael Pérez-Fournon, Ignasi Pérez-Ràfols, Patrick Petitjean, Robert Pfaffenberger, Janine Pforr, Matthew M. Pieri, Francisco Prada, Adrian M. Price-Whelan, M. Jordan Raddick, Rafael Rebolo, James Rich, Gordon T. Richards, Constance M. Rockosi, Natalie A. Roe, Ashley J. Ross, Nicholas P. Ross, Graziano Rossi, J. A. Rubiño-Martin, Lado Samushia, Ariel G. Sánchez, Conor Sayres, Sarah J. Schmidt, Donald P. Schneider, C. G. Scóccola, Hee-Jong Seo, Alaina Shelden, Erin Sheldon, Yue Shen, Yiping Shu, Anže Slosar, Stephen A. Smee, Stephanie A. Snedden, Fritz Stauffer, Oliver Steele, Michael A. Strauss, Alina Streblyanska, Nao Suzuki, Molly E. C. Swanson, Tomer Tal, Masayuki Tanaka, Daniel Thomas, Jeremy L. Tinker, Rita Tojeiro, Christy A. Tremonti, M. Vargas Magaña, Licia Verde, Matteo Viel, David A. Wake, Mike Watson, Benjamin A. Weaver, David H. Weinberg, Benjamin J. Weiner, Andrew A. West, Martin White, W. M. Wood-Vasey, Christophe Yeche, Idit Zehavi, Gong-Bo Zhao, and Zheng Zheng, *The Baryon Oscillation Spectroscopic Survey of SDSS-III*, AJ145 (2013), no. 1, 10.

[31] Roelof S. de Jong, Olga Bellido-Tirado, Cristina Chiappini, Éric Depagne, Roger Haynes, Diana Johl, Olivier Schnurr, Axel Schwope, Jakob Walcher, Frank Dionies, Dionne Haynes, Andreas Kelz, Francisco S. Kitaura, Georg Lamer, Ivan Minchev, Volker Müller, Sebastián. E. Nuza, Jean-Christophe Olaya, Tilmann Piffl, Emil Popow, Matthias Steinmetz, Ugur Ural, Mary Williams, Roland Winkler, Lutz

Wisotzki, Wolfgang R. Ansorge, Manda Banerji, Eduardo Gonzalez Solares, Mike Irwin, Robert C. Kennicutt, Dave King, Richard G. McMahon, Sergey Koposov, Ian R. Parry, David Sun, Nicholas A. Walton, Gert Finger, Olaf Iwert, Mirko Krumpe, Jean-Louis Lizon, Mainieri Vincenzo, Jean-Philippe Amans, Piercarlo Bonifacio, Mathieu Cohen, Patrick Francois, Pascal Jagourel, Shan B. Mignot, Frédéric Royer, Paola Sartoretti, Ralf Bender, Frank Grupp, Hans-Joachim Hess, Florian Lang-Bardl, Bernard Muschielok, Hans Böhringer, Thomas Boller, Angela Bongiorno, Marcella Brusa, Tom Dwelly, Andrea Merloni, Kirpal Nandra, Mara Salvato, Johannes H. Pragt, Ramón Navarro, Gerrit Gerlofsma, Ronald Roelfsema, Gavin B. Dalton, Kevin F. Middleton, Ian A. Tosh, Corrado Boeche, Elisabetta Caffau, Norbert Christlieb, Eva K. Grebel, Camilla Hansen, Andreas Koch, Hans-G. Ludwig, Andreas Quirrenbach, Luca Sbordone, Walter Seifert, Guido Thimm, Trifon Trifonov, Amina Helmi, Scott C. Trager, Sofia Feltzing, Andreas Korn, and Wilfried Boland, *4MOST: 4-metre multi-object spectroscopic telescope*, Ground-based and Airborne Instrumentation for Astronomy IV (Ian S. McLean, Suzanne K. Ramsay, and Hideki Takami, eds.), Society of Photo-Optical Instrumentation Engineers (SPIE) Conference Series, vol. 8446, September 2012, p. 84460T.

[32] K. D. Denney, Keith Horne, Yue Shen, W. N. Brandt, Luis C. Ho, B. M. Peterson, Gordon T. Richards, J. R. Trump, and J. Ge, *The Sloan Digital Sky Survey Reverberation Mapping Project: An Investigation of Biases in C IV Emission Line Properties*, ApJS224 (2016), no. 2, 14.

[33] DESI Collaboration, Amir Aghamousa, Jessica Aguilar, Steve Ahlen, Shadab Alam, Lori E. Allen, Carlos Allende Prieto, James Annis, Stephen Bailey, Christophe Balland, Otger Ballester, Charles Baltay, Lucas Beaufore, Chris Bebek, Timothy C. Beers, Eric F. Bell, José Luis Bernal, Robert Besuner, Florian Beutler, Chris Blake, Hannes Bleuler, Michael Blomqvist, Robert Blum, Adam S. Bolton, Cesar Briceno, David Brooks, Joel R. Brownstein, Elizabeth Buckley-Geer, Angela Burden, Etienne Burtin, Nicolas G. Busca, Robert N. Cahn, Yan-Chuan Cai, Laia Cardiel-Sas,

Raymond G. Carlberg, Pierre-Henri Carton, Ricard Casas, Francisco J. Castander, Jorge L. Cervantes-Cota, Todd M. Claybaugh, Madeline Close, Carl T. Coker, Shaun Cole, Johan Comparat, Andrew P. Cooper, M. C. Cousinou, Martin Crocce, Jean-Gabriel Cuby, Daniel P. Cunningham, Tamara M. Davis, Kyle S. Dawson, Axel de la Macorra, Juan De Vicente, Timothée Delubac, Mark Derwent, Arjun Dey, Govinda Dhungana, Zhejie Ding, Peter Doel, Yutong T. Duan, Anne Ealet, Jerry Edelstein, Sarah Eftekharzadeh, Daniel J. Eisenstein, Ann Elliott, Stéphanie Escoffier, Matthew Evatt, Parker Fagrelius, Xiaohui Fan, Kevin Fanning, Arya Farahi, Jay Farihi, Ginevra Favole, Yu Feng, Enrique Fernandez, Joseph R. Findlay, Douglas P. Finkbeiner, Michael J. Fitzpatrick, Brenna Flaugher, Samuel Flender, Andreu Font-Ribera, Jaime E. Forero-Romero, Pablo Fosalba, Carlos S. Frenk, Michele Fumagalli, Boris T. Gaensicke, Giuseppe Gallo, Juan Garcia-Bellido, Enrique Gaztanaga, Nicola Pietro Gentile Fusillo, Terry Gerard, Irena Gershkovich, Tommaso Giannantonio, Denis Gillet, Guillermo Gonzalez-de-Rivera, Violeta Gonzalez-Perez, Shelby Gott, Or Graur, Gaston Gutierrez, Julien Guy, Salman Habib, Henry Heetderks, Ian Heetderks, Katrin Heitmann, Wojciech A. Hellwing, David A. Herrera, Shirley Ho, Stephen Holland, Klaus Honscheid, Eric Huff, Timothy A. Hutchinson, Dragan Huterer, Ho Seong Hwang, Joseph Maria Illa Laguna, Yuzo Ishikawa, Dianna Jacobs, Niall Jeffrey, Patrick Jelinsky, Elise Jennings, Linhua Jiang, Jorge Jimenez, Jennifer Johnson, Richard Joyce, Eric Jullo, Stéphanie Juneau, Sami Kama, Armin Karcher, Sonia Karkar, Robert Kehoe, Noble Kennamer, Stephen Kent, Martin Kilbinger, Alex G. Kim, David Kirkby, Theodore Kisner, Ellie Kitanidis, Jean-Paul Kneib, Sergey Koposov, Eve Kovacs, Kazuya Koyama, Anthony Kremin, Richard Kron, Luzius Kronig, Andrea Kueter-Young, Cedric G. Lacey, Robin Lafever, Ofer Lahav, Andrew Lambert, Michael Lampton, Martin Landriau, Dustin Lang, Tod R. Lauer, Jean-Marc Le Goff, Laurent Le Guillou, Auguste Le Van Suu, Jae Hyeon Lee, Su-Jeong Lee, Daniela Leitner, Michael Lesser, Michael E. Levi, Benjamin L'Huillier, Baojiu Li, Ming Liang, Huan Lin, Eric Linder, Sarah R. Loebman, Zarija Lukić,

Jun Ma, Niall MacCrann, Christophe Magneville, Laleh Makarem, Marc Manera, Christopher J. Manser, Robert Marshall, Paul Martini, Richard Massey, Thomas Matheson, Jeremy McCauley, Patrick McDonald, Ian D. McGreer, Aaron Meisner, Nigel Metcalfe, Timothy N. Miller, Ramon Miquel, John Moustakas, Adam Myers, Milind Naik, Jeffrey A. Newman, Robert C. Nichol, Andrina Nicola, Luiz Nicolati da Costa, Jundan Nie, Gustavo Niz, Peder Norberg, Brian Nord, Dara Norman, Peter Nugent, Thomas O'Brien, Minji Oh, Knut A. G. Olsen, Cristobal Padilla, Hamsa Padmanabhan, Nikhil Padmanabhan, Nathalie Palanque-Delabrouille, Antonella Palmese, Daniel Pappalardo, Isabelle Pâris, Changbom Park, Anna Patej, John A. Peacock, Hiranya V. Peiris, Xiyan Peng, Will J. Percival, Sandrine Perruchot, Matthew M. Pieri, Richard Pogge, Jennifer E. Pollack, Claire Poppett, Francisco Prada, Abhishek Prakash, Ronald G. Probst, David Rabinowitz, Anand Raichoor, Chang Hee Ree, Alexandre Refregier, Xavier Regal, Beth Reid, Kevin Reil, Mehdi Rezaie, Constance M. Rockosi, Natalie Roe, Samuel Ronayette, Aaron Roodman, Ashley J. Ross, Nicholas P. Ross, Graziano Rossi, Eduardo Rozo, Vanina Ruhlmann-Kleider, Eli S. Rykoff, Cristiano Sabiu, Lado Samushia, Eusebio Sanchez, Javier Sanchez, David J. Schlegel, Michael Schneider, Michael Schubnell, Aurélia Secroun, Uros Seljak, Hee-Jong Seo, Santiago Serrano, Arman Shafieloo, Huanyuan Shan, Ray Sharples, Michael J. Sholl, William V. Shourt, Joseph H. Silber, David R. Silva, Martin M. Sirk, Anze Slosar, Alex Smith, George F. Smoot, Debopam Som, Yong-Seon Song, David Sprayberry, Ryan Staten, Andy Stefanik, Gregory Tarle, Suk Sien Tie, Jeremy L. Tinker, Rita Tojeiro, Francisco Valdes, Octavio Valenzuela, Monica Valluri, Mariana Vargas-Magana, Licia Verde, Alistair R. Walker, Jiali Wang, Yuting Wang, Benjamin A. Weaver, Curtis Weaverdyck, Risa H. Wechsler, David H. Weinberg, Martin White, Qian Yang, Christophe Yeche, Tianmeng Zhang, Gong-Bo Zhao, Yi Zheng, Xu Zhou, Zhimin Zhou, Yaling Zhu, Hu Zou, and Ying Zu, *The DESI Experiment Part I: Science,Targeting, and Survey Design*, arXiv e-prints (2016), arXiv:1611.00036.

[34] Tiziana Di Matteo, Jörg Colberg, Volker Springel, Lars Hernquist, and Debora Sijacki, *Direct Cosmological Simulations of the Growth of Black Holes and Galaxies*, ApJ676 (2008), no. 1, 33–53.

[35] Aleksandar M. Diamond-Stanic, Xiaohui Fan, W. N. Brandt, Ohad Shemmer, Michael A. Strauss, Scott F. Anderson, Christopher L. Carilli, Robert R. Gibson, Linhua Jiang, J. Serena Kim, Gordon T. Richards, Gary D. Schmidt, Donald P. Schneider, Yue Shen, Paul S. Smith, Marianne Vestergaard, and Jason E. Young, *High-redshift SDSS Quasars with Weak Emission Lines*, ApJ699 (2009), no. 1, 782–799.

[36] Cooper Dix, Ohad Shemmer, Michael S. Brotherton, Richard F. Green, Michelle Mason, and Adam D. Myers, *Prescriptions for Correcting Ultraviolet-based Redshifts for Luminous Quasars at High Redshift*, ApJ893 (2020), no. 1, 14.

[37] Xiao-Bo Dong, Ting-Gui Wang, Jian-Guo Wang, Xiaohui Fan, Huiyuan Wang, Hongyan Zhou, and Weimin Yuan, *Eddington Ratio Governs the Equivalent Width of Mg II Emission Line in Active Galactic Nuclei*, ApJ703 (2009), no. 1, L1–L5.

[38] Pu Du, Chen Hu, Kai-Xing Lu, Fang Wang, Jie Qiu, Yan-Rong Li, Jin-Ming Bai, Shai Kaspi, Hagai Netzer, Jian-Min Wang, and SEAMBH Collaboration, *Supermassive Black Holes with High Accretion Rates in Active Galactic Nuclei. I. First Results from a New Reverberation Mapping Campaign*, ApJ782 (2014), no. 1, 45.

[39] Pu Du and Jian-Min Wang, *The Radius-Luminosity Relationship Depends on Optical Spectra in Active Galactic Nuclei*, ApJ886 (2019), no. 1, 42.

[40] Pu Du, Jian-Min Wang, Chen Hu, Luis C. Ho, Yan-Rong Li, and Jin-Ming Bai, *The Fundamental Plane of the Broad-line Region in Active Galactic Nuclei*, ApJ818 (2016), no. 1, L14.

[41] Pu Du, Zhi-Xiang Zhang, Kai Wang, Ying-Ke Huang, Yue Zhang, Kai-Xing Lu, Chen Hu, Yan-Rong Li, Jin-Ming Bai, Wei-Hao Bian, Ye-Fei Yuan, Luis C. Ho, Jian-Min Wang, and SEAMBH Collaboration, *Supermassive Black Holes with High Accretion Rates in Active Galactic Nuclei. IX. 10 New Observations of Reverberation Mapping and Shortened Hβ Lags*, ApJ856 (2018), no. 1, 6.

[42] Xiaohui Fan, Michael A. Strauss, James E. Gunn, Robert H. Lupton, C. L. Carilli, M. P. Rupen, Gary D. Schmidt, Leonidas A. Moustakas, Marc Davis, James Annis, Neta A. Bahcall, J. Brinkmann, Robert J. Brunner, István Csabai, Mamoru Doi, Masataka Fukugita, Timothy M. Heckman, G. S. Hennessy, Robert B. Hindsley, Željko Ivezić , G. R. Knapp, D. Q. Lamb, Jeffrey A. Munn, A. George Pauls, Jeffrey R. Pier, Constance M. Rockosi, Donald P. Schneider, Alexander S. Szalay, Douglas L. Tucker, and Donald G. York, *The Discovery of a High-Redshift Quasar without Emission Lines from Sloan Digital Sky Survey Commissioning Data*, ApJ526 (1999), no. 2, L57–L60.

[43] Laura Ferrarese and David Merritt, *A Fundamental Relation between Supermassive Black Holes and Their Host Galaxies*, ApJ539 (2000), no. 1, L9–L12.

[44] Gloria Fonseca Alvarez, Jonathan R. Trump, Y. Homayouni, C. J. Grier, Yue Shen, Keith Horne, Jennifer I. Hsiu Li, W. N. Brandt, Luis C. Ho, B. M. Peterson, and D. P. Schneider, *The Sloan Digital Sky Survey Reverberation Mapping Project: The Hβ Radius-Luminosity Relation*, ApJ899 (2020), no. 1, 73.

[45] Andreu Font-Ribera, Eduard Arnau, Jordi Miralda-Escudé, Emmanuel Rollinde, J. Brinkmann, Joel R. Brownstein, Khee-Gan Lee, Adam D. Myers, Nathalie Palanque-Delabrouille, Isabelle Pâris, Patrick Petitjean, James Rich, Nicholas P. Ross, Donald P. Schneider, and Martin White, *The large-scale quasar-Lyman α forest cross-correlation from BOSS*, J. Cosmology Astropart. Phys.2013 (2013), no. 5, 018.

[46] Shuqi Fu, W. N. Brandt, Fan Zou, Ari Laor, Gordon P. Garmire, Qingling Ni, III Timlin, John D., and Yongquan Xue, *The Nature of Luminous Quasars with Very Large C IV Equivalent Widths*, ApJ934 (2022), no. 2, 97.

[47] Jonathan P. Gardner, John C. Mather, Mark Clampin, Rene Doyon, Matthew A. Greenhouse, Heidi B. Hammel, John B. Hutchings, Peter Jakobsen, Simon J. Lilly, Knox S. Long, Jonathan I. Lunine, Mark J. McCaughrean, Matt Mountain, John Nella, George H. Rieke, Marcia J. Rieke, Hans-Walter Rix, Eric P. Smith, George Sonneborn, Massimo Stiavelli, H. S. Stockman, Rogier A. Windhorst, and Gillian S. Wright, *The James Webb Space Telescope*, Space Sci. Rev.123 (2006), no. 4, 485–606.

[48] C. M. Gaskell, *A redshift difference between high and low ionization emission-line regions in QSO's-evidence for radial motions.*, ApJ263 (1982), 79–86.

[49] Karl Gebhardt, Ralf Bender, Gary Bower, Alan Dressler, S. M. Faber, Alexei V. Filippenko, Richard Green, Carl Grillmair, Luis C. Ho, John Kormendy, Tod R. Lauer, John Magorrian, Jason Pinkney, Douglas Richstone, and Scott Tremaine, *A Relationship between Nuclear Black Hole Mass and Galaxy Velocity Dispersion*, ApJ539 (2000), no. 1, L13–L16.

[50] Robert R. Gibson, Linhua Jiang, W. N. Brandt, Patrick B. Hall, Yue Shen, Jianfeng Wu, Scott F. Anderson, Donald P. Schneider, Daniel Vanden Berk, S. C. Gallagher, Xiaohui Fan, and Donald G. York, *A Catalog of Broad Absorption Line Quasars in Sloan Digital Sky Survey Data Release 5*, ApJ692 (2009), no. 1, 758–777.

[51] Margherita Giustini and Daniel Proga, *A global view of the inner accretion and ejection flow around super massive black holes. Radiation-driven accretion disk winds in a physical context*, A&A630 (2019), A94.

[52] GRAVITY Collaboration, R. Abuter, N. Aimar, A. Amorim, J. Ball, M. Bauböck, J. P. Berger, H. Bonnet, G. Bourdarot, W. Brandner, V. Cardoso, Y. Clénet, Y. Dallilar, R. Davies, P. T. de Zeeuw, J. Dexter, A. Drescher, F. Eisenhauer, N. M. Förster Schreiber, A. Foschi, P. Garcia, F. Gao, E. Gendron, R. Genzel, S. Gillessen, M. Habibi, X. Haubois, G. Heißel, T. Henning, S. Hippler, M. Horrobin, L. Jochum, L. Jocou, A. Kaufer, P. Kervella, S. Lacour, V. Lapeyrère, J. B. Le Bouquin, P. Léna, D. Lutz, T. Ott, T. Paumard, K. Perraut, G. Perrin, O. Pfuhl, S. Rabien, J. Shangguan, T. Shimizu, S. Scheithauer, J. Stadler, A. W. Stephens, O. Straub, C. Straubmeier, E. Sturm, L. J. Tacconi, K. R. W. Tristram, F. Vincent, S. von Fellenberg, F. Widmann, E. Wieprecht, E. Wiezorrek, J. Woillez, S. Yazici, and A. Young, *Mass distribution in the Galactic Center based on interferometric astrometry of multiple stellar orbits*, A&A657 (2022), L12.

[53] Jenny E. Greene and Luis C. Ho, *Estimating Black Hole Masses in Active Galaxies Using the Hα Emission Line*, ApJ630 (2005), no. 1, 122–129.

[54] Jenny E. Greene, Chien Y. Peng, Minjin Kim, Cheng-Yu Kuo, James A. Braatz, C. M. V. Impellizzeri, James J. Condon, K. Y. Lo, Christian Henkel, and Mark J. Reid, *Precise Black Hole Masses from Megamaser Disks: Black Hole-Bulge Relations at Low Mass*, ApJ721 (2010), no. 1, 26–45.

[55] C. J. Grier, Yue Shen, Keith Horne, W. N. Brandt, J. R. Trump, P. B. Hall, K. Kinemuchi, David Starkey, D. P. Schneider, Luis C. Ho, Y. Homayouni, Jennifer I-Hsiu Li, Ian D. McGreer, B. M. Peterson, Dmitry Bizyaev, Yuguang Chen, K. S. Dawson, Sarah Eftekharzadeh, Yucheng Guo, Siyao Jia, Linhua Jiang, Jean-Paul Kneib, Feng Li, Zefeng Li, Jundan Nie, Audrey Oravetz, Daniel Oravetz, Kaike Pan, Patrick Petitjean, Kara A. Ponder, Jesse Rogerson, M. Vivek, Tianmeng Zhang, and Hu Zou, *The Sloan Digital Sky Survey Reverberation Mapping Project: Initial C IV Lag Results from Four Years of Data*, ApJ887 (2019), no. 1, 38.

[56] C. J. Grier, J. R. Trump, Yue Shen, Keith Horne, Karen Kinemuchi, Ian D. McGreer, D. A. Starkey, W. N. Brandt, P. B. Hall, C. S. Kochanek, Yuguang Chen, K. D. Denney, Jenny E. Greene, L. C. Ho, Y. Homayouni, Jennifer I-Hsiu Li, Liuyi Pei, B. M. Peterson, P. Petitjean, D. P. Schneider, Mouyuan Sun, Yusura AlSayyad, Dmitry Bizyaev, Jonathan Brinkmann, Joel R. Brownstein, Kevin Bundy, K. S. Dawson, Sarah Eftekharzadeh, J. G. Fernandez-Trincado, Yang Gao, Timothy A. Hutchinson, Siyao Jia, Linhua Jiang, Daniel Oravetz, Kaike Pan, Isabelle Paris, Kara A. Ponder, Christina Peters, Jesse Rogerson, Audrey Simmons, Robyn Smith, and Ran Wang, *The Sloan Digital Sky Survey Reverberation Mapping Project: Hα and Hβ Reverberation Measurements from First-year Spectroscopy and Photometry*, ApJ851 (2017), no. 1, 21.

[57] Paul C. Hewett and Vivienne Wild, *Improved redshifts for SDSS quasar spectra*, MNRAS405 (2010), no. 4, 2302–2316.

[58] Luis C. Ho and Minjin Kim, *The Black Hole Mass Scale of Classical and Pseudo Bulges in Active Galaxies*, ApJ789 (2014), no. 1, 17.

[59] David W. Hogg, *Distance measures in cosmology*, arXiv e-prints (1999), astro–ph/9905116.

[60] Y. Homayouni, Jonathan R. Trump, C. J. Grier, Keith Horne, Yue Shen, W. N. Brandt, Kyle S. Dawson, Gloria Fonseca Alvarez, Paul J. Green, P. B. Hall, Juan V. Hernández Santisteban, Luis C. Ho, Karen Kinemuchi, C. S. Kochanek, Jennifer I. Hsiu Li, B. M. Peterson, D. P. Schneider, D. A. Starkey, Dmitry Bizyaev, Kaike Pan, Daniel Oravetz, and Audrey Simmons, *The Sloan Digital Sky Survey Reverberation Mapping Project: Mg II Lag Results from Four Years of Monitoring*, ApJ901 (2020), no. 1, 55.

[61] Philip F. Hopkins and Martin Elvis, *Quasar feedback: more bang for your buck*, MNRAS401 (2010), no. 1, 7–14.

[62] Philip F. Hopkins, Brant Robertson, Elisabeth Krause, Lars Hernquist, and Thomas J. Cox, *An Upper Limit to the Degree of Evolution between Supermassive Black Holes and Their Host Galaxies*, ApJ652 (2006), no. 1, 107–111.

[63] K. Hryniewicz, B. Czerny, M. Nikołajuk, and J. Kuraszkiewicz, *SDSS J094533.99+100950.1 - the remarkable weak emission line quasar*, MNRAS404 (2010), no. 4, 2028–2036.

[64] J. B. Hutchings, A. Cherniawsky, R. M. Cutri, and B. O. Nelson, *Host Galaxies of Two Micron All Sky Survey-selected QSOs at Redshift over 0.3*, AJ131 (2006), no. 2, 680–685.

[65] T. H. Jarrett, M. Cohen, F. Masci, E. Wright, D. Stern, D. Benford, A. Blain, S. Carey, R. M. Cutri, P. Eisenhardt, C. Lonsdale, A. Mainzer, K. Marsh, D. Padgett, S. Petty, M. Ressler, M. Skrutskie, S. Stanford, J. Surace, C. W. Tsai, S. Wheelock, and D. L. Yan, *The Spitzer-WISE Survey of the Ecliptic Poles*, ApJ735 (2011), no. 2, 112.

[66] D. W. Just, W. N. Brandt, O. Shemmer, A. T. Steffen, D. P. Schneider, G. Chartas, and G. P. Garmire, *The X-Ray Properties of the Most Luminous Quasars from the Sloan Digital Sky Survey*, ApJ665 (2007), no. 2, 1004–1022.

[67] Shai Kaspi, W. N. Brandt, Dan Maoz, Hagai Netzer, Donald P. Schneider, and Ohad Shemmer, *Reverberation Mapping of High-Luminosity Quasars: First Results*, ApJ659 (2007), no. 2, 997–1007.

[68] Shai Kaspi, W. N. Brandt, Dan Maoz, Hagai Netzer, Donald P. Schneider, Ohad Shemmer, and C. J. Grier, *Taking a Long Look: A Two-decade Reverberation Mapping*

Study of High-luminosity Quasars, ApJ915 (2021), no. 2, 129.

[69] Shai Kaspi, Dan Maoz, Hagai Netzer, Bradley M. Peterson, Marianne Vestergaard, and Buell T. Jannuzi, *The Relationship between Luminosity and Broad-Line Region Size in Active Galactic Nuclei*, ApJ629 (2005), no. 1, 61–71.

[70] Shai Kaspi, Paul S. Smith, Hagai Netzer, Dan Maoz, Buell T. Jannuzi, and Uriel Giveon, *Reverberation Measurements for 17 Quasars and the Size-Mass-Luminosity Relations in Active Galactic Nuclei*, ApJ533 (2000), no. 2, 631–649.

[71] K. I. Kellermann, R. Sramek, M. Schmidt, D. B. Shaffer, and R. Green, *VLA Observations of Objects in the Palomar Bright Quasar Survey*, AJ98 (1989), 1195.

[72] Brandon C. Kelly, *Some Aspects of Measurement Error in Linear Regression of Astronomical Data*, ApJ665 (2007), no. 2, 1489–1506.

[73] Brandon C. Kelly and Andrea Merloni, *Mass Functions of Supermassive Black Holes across Cosmic Time*, Advances in Astronomy 2012 (2012), 970858.

[74] K. T. Korista, D. Alloin, P. Barr, J. Clavel, R. D. Cohen, D. M. Crenshaw, I. N. Evans, K. Horne, A. P. Koratkar, G. A. Kriss, J. H. Krolik, M. A. Malkan, S. L. Morris, H. Netzer, P. T. O'Brien, B. M. Peterson, G. A. Reichert, P. M. Rodriguez-Pascual, W. Wamsteker, K. S. J. Anderson, D. J. Axon, E. Benitez, P. Berlind, R. Bertram, Jr. Blackwell, J. H., N. G. Bochkarev, C. Boisson, M. Carini, R. Carrillo, T. E. Carone, F. Z. Cheng, J. A. Christensen, K. K. Chuvaev, M. Dietrich, J. J. Dokter, V. Doroshenko, D. Dultzin-Hacyan, M. N. England, B. R. Espey, A. V. Filippenko, C. M. Gaskell, M. R. Goad, L. C. Ho, J. P. Huchra, X. J. Jiang, S. Kaspi, W. Kollatschny, A. Laor, J. P. Luminet, G. M. MacAlpine, J. W. MacKenty, Yu. F. Malkov, D. Maoz, P. G. Martin, T. Matheson, B. McCollum, N. Merkulova, L. Metik, M. Mignoli, H. R. Miller, M. G. Pastoriza, D. Pelat, J. Penfold, M. Perez, G. C. Perola, J. L. Persaud, J. Peters, R. Pitts, R. W. Pogge, I. Pronik, V. I. Pronik, R. L. Ptak, L. Rawley, M. C. Recondo-Gonzalez, J. M. Rodriguez-Espinosa, W. Romanishin, A. C. Sadun, I. Salamanca, M. Santos-Lleo, K. Sekiguchi, S. G. Sergeev, A. I. Shapovalova, J. C. Shields, C. Shrader, J. M. Shull, N. A. Silbermann, M. L. Sitko, D. R. Skillman, H. A. Smith, S. M. Smith, M. A. J.

Snijders, L. S. Sparke, G. M. Stirpe, R. E. Stoner, W. H. Sun, U. Thiele, S. Tokarz, Z. I. Tsvetanov, D. A. Turnshek, S. Veilleux, R. M. Wagner, S. J. Wagner, I. Wanders, T. Wang, W. F. Welsh, R. J. Weymann, R. J. White, B. J. Wilkes, B. J. Wills, C. Winge, H. Wu, and Z. L. Zou, *Steps toward Determination of the Size and Structure of the Broad-Line Region in Active Galactic Nuclei. VIII. an Intensive HST, IUE, and Ground-based Study of NGC 5548*, ApJS97 (1995), 285.

[75] Ryan A. Lane, Ohad Shemmer, Aleksandar M. Diamond-Stanic, Xiaohui Fan, Scott F. Anderson, W. N. Brandt, Richard M. Plotkin, Gordon T. Richards, Donald P. Schneider, and Michael A. Strauss, *The Ultraviolet-to-mid-infrared Spectral Energy Distribution of Weak Emission Line Quasars*, ApJ743 (2011), no. 2, 163.

[76] Ari Laor, *On Quasar Masses and Quasar Host Galaxies*, ApJ505 (1998), no. 2, L83–L86.

[77] Huynh Anh N. Le, Jong-Hak Woo, and Yongquan Xue, *Calibrating Mg II-based Black Hole Mass Estimators Using Low-to-high-luminosity Active Galactic Nuclei*, ApJ901 (2020), no. 1, 35.

[78] Karen M. Leighly, Jules P. Halpern, Edward B. Jenkins, and Darrin Casebeer, *The Intrinsically X-Ray-weak Quasar PHL 1811. II. Optical and UV Spectra and Analysis*, ApJS173 (2007), no. 1, 1–36.

[79] Michael Levi, Chris Bebek, Timothy Beers, Robert Blum, Robert Cahn, Daniel Eisenstein, Brenna Flaugher, Klaus Honscheid, Richard Kron, Ofer Lahav, Patrick McDonald, Natalie Roe, David Schlegel, and representing the DESI collaboration, *The DESI Experiment, a whitepaper for Snowmass 2013*, arXiv e-prints (2013), arXiv:1308.0847.

[80] Paulina Lira, Shai Kaspi, Hagai Netzer, Ismael Botti, Nidia Morrell, Julián Mejía-Restrepo, Paula Sánchez-Sáez, Jorge Martínez-Palomera, and Paula López, *Reverberation Mapping of Luminous Quasars at High z*, ApJ865 (2018), no. 1, 56.

[81] B. Luo, W. N. Brandt, P. B. Hall, Jianfeng Wu, S. F. Anderson, G. P. Garmire, R. R. Gibson, R. M. Plotkin, G. T. Richards, D. P. Schneider, O. Shemmer, and Yue Shen, *X-ray Insights into the Nature of PHL 1811 Analogs and Weak Emission-line Quasars: Unification with a Geometrically Thick Accretion Disk?*, ApJ805 (2015), no. 2, 122.

[82] Brad W. Lyke, Alexandra N. Higley, J. N. McLane, Danielle P. Schurhammer, Adam D. Myers, Ashley J. Ross, Kyle Dawson, Solène Chabanier, Paul Martini, Nicolás G. Busca, Hélion du Mas des Bourboux, Mara Salvato, Alina Streblyanska, Pauline Zarrouk, Etienne Burtin, Scott F. Anderson, Julian Bautista, Dmitry Bizyaev, W. N. Brandt, Jonathan Brinkmann, Joel R. Brownstein, Johan Comparat, Paul Green, Axel de la Macorra, Andrea Muñoz Gutiérrez, Jiamin Hou, Jeffrey A. Newman, Nathalie Palanque-Delabrouille, Isabelle Pâris, Will J. Percival, Patrick Petitjean, James Rich, Graziano Rossi, Donald P. Schneider, Alexander Smith, M. Vivek, and Benjamin Alan Weaver, *The Sloan Digital Sky Survey Quasar Catalog: Sixteenth Data Release*, ApJS250 (2020), no. 1, 8.

[83] R. Maiolino, S. Gallerani, R. Neri, C. Cicone, A. Ferrara, R. Genzel, D. Lutz, E. Sturm, L. J. Tacconi, F. Walter, C. Feruglio, F. Fiore, and E. Piconcelli, *Evidence of strong quasar feedback in the early Universe*, MNRAS425 (2012), no. 1, L66–L70.

[84] Jaya Maithil, Michael S. Brotherton, Ohad Shemmer, Pu Du, Jian-Min Wang, Adam D. Myers, Jacob N. McLane, Cooper Dix, and Brandon M. Matthews, *Systematically smaller single-epoch quasar black hole masses using a radius-luminosity relationship corrected for spectral bias*, MNRAS515 (2022), no. 1, 491–506.

[85] A. Marconi, G. Risaliti, R. Gilli, L. K. Hunt, R. Maiolino, and M. Salvati, *Local supermassive black holes, relics of active galactic nuclei and the X-ray background*, MNRAS351 (2004), no. 1, 169–185.

[86] Andrea Marlar, Ohad Shemmer, S. F. Anderson, W. N. Brandt, A. M. Diamond-Stanic, X. Fan, B. Luo, R. M. Plotkin, Gordon T. Richards, D. P. Schneider, and Jianfeng Wu, *Steep Hard-X-Ray Spectra Indicate Extremely High Accretion Rates in Weak Emission-line Quasars*, ApJ865 (2018), no. 2, 92.

[87] M. L. Martínez-Aldama, A. del Olmo, P. Marziani, J. W. Sulentic, C. A. Negrete, D. Dultzin, M. D'Onofrio, and J. Perea, *Extreme quasars at high redshift*, A&A618 (2018), A179.

[88] Michelle Mason, Michael S. Brotherton, and Adam Myers, *Evaluating and improving*

the redshifts of z > 2.2 quasars, MNRAS469 (2017), no. 4, 4675–4682.

[89] F. Massaro, E. J. Marchesini, R. D'Abrusco, N. Masetti, I. Andruchow, and Howard A. Smith, *Radio-weak BL Lac Objects in the Fermi Era*, ApJ834 (2017), no. 2, 113.

[90] Brandon M. Matthews, Ohad Shemmer, Cooper Dix, Michael S. Brotherton, Adam D. Myers, I. Andruchow, W. N. Brandt, Gabriel A. Ferrero, S. C. Gallagher, Richard Green, Paulina Lira, Richard M. Plotkin, Gordon T. Richards, Jessie C. Runnoe, Donald P. Schneider, Yue Shen, Michael A. Strauss, and Beverley J. Wills, *Placing High-redshift Quasars in Perspective: A Catalog of Spectroscopic Properties from the Gemini Near Infrared Spectrograph-Distant Quasar Survey*, ApJS252 (2021), no. 2, 15.

[91] Ian D. McGreer, Sarah Eftekharzadeh, Adam D. Myers, and Xiaohui Fan, *A Constraint on Quasar Clustering at z = 5 from a Binary Quasar*, AJ151 (2016), no. 3, 61.

[92] J. E. Mejía-Restrepo, P. Lira, H. Netzer, B. Trakhtenbrot, and D. M. Capellupo, *The effect of nuclear gas distribution on the mass determination of supermassive black holes*, Nature Astronomy 2 (2018), 63–68.

[93] H. Meusinger and N. Balafkan, *A large sample of Kohonen-selected SDSS quasars with weak emission lines: selection effects and statistical properties*, A&A568 (2014), A114.

[94] B. P. Miller, W. N. Brandt, D. P. Schneider, R. R. Gibson, A. T. Steffen, and Jianfeng Wu, *X-ray Emission from Optically Selected Radio-intermediate and Radio-loud Quasars*, ApJ726 (2011), no. 1, 20.

[95] N. Murray, J. Chiang, S. A. Grossman, and G. M. Voit, *Accretion Disk Winds from Active Galactic Nuclei*, ApJ451 (1995), 498.

[96] Rodrigo S. Nemmen and Michael S. Brotherton, *Quasar bolometric corrections: theoretical considerations*, MNRAS408 (2010), no. 3, 1598–1605.

[97] Hagai Netzer, *Bolometric correction factors for active galactic nuclei*, MNRAS488 (2019), no. 4, 5185–5191.

[98] Hagai Netzer, Paulina Lira, Benny Trakhtenbrot, Ohad Shemmer, and Iara Cury, *Black Hole Mass and Growth Rate at High Redshift*, ApJ671 (2007), no. 2, 1256–1263.

[99] Nathen H. Nguyen, Paulina Lira, Benny Trakhtenbrot, Hagai Netzer, Claudia Ci-

cone, Roberto Maiolino, and Ohad Shemmer, *ALMA Observations of Quasar Host Galaxies at z = 4.8*, ApJ895 (2020), no. 1, 74.

[100] Q. Ni, W. N. Brandt, B. Luo, G. P. Garmire, P. B. Hall, R. M. Plotkin, O. Shemmer, J. D. Timlin, F. Vito, J. Wu, and W. Yi, *Sensitive Chandra coverage of a representative sample of weak-line quasars: revealing the full range of X-ray properties*, MNRAS511 (2022), no. 4, 5251–5264.

[101] Q. Ni, W. N. Brandt, B. Luo, P. B. Hall, Yue Shen, S. F. Anderson, R. M. Plotkin, Gordon T. Richards, D. P. Schneider, O. Shemmer, and Jianfeng Wu, *Connecting the X-ray properties of weak-line and typical quasars: testing for a geometrically thick accretion disk*, MNRAS480 (2018), no. 4, 5184–5202.

[102] Eran O. Ofek, Dan Maoz, Hans-Walter Rix, Christopher S. Kochanek, and Emilio E. Falco, *Spectroscopic Redshifts for Seven Lens Galaxies*, ApJ641 (2006), no. 1, 70–77.

[103] Christopher A. Onken, Laura Ferrarese, David Merritt, Bradley M. Peterson, Richard W. Pogge, Marianne Vestergaard, and Amri Wandel, *Supermassive Black Holes in Active Galactic Nuclei. II. Calibration of the Black Hole Mass-Velocity Dispersion Relationship for Active Galactic Nuclei*, ApJ615 (2004), no. 2, 645–651.

[104] M. J. Page, J. A. Stevens, R. J. Ivison, and F. J. Carrera, *The Evolutionary Sequence of Active Galactic Nuclei and Galaxy Formation Revealed*, ApJ611 (2004), no. 2, L85–L88.

[105] Anna Pancoast, Brendon J. Brewer, Tommaso Treu, Daeseong Park, Aaron J. Barth, Misty C. Bentz, and Jong-Hak Woo, *Modelling reverberation mapping data - II. Dynamical modelling of the Lick AGN Monitoring Project 2008 data set*, MNRAS445 (2014), no. 3, 3073–3091.

[106] Isabelle Pâris, Patrick Petitjean, Éric Aubourg, Adam D. Myers, Alina Streblyanska, Brad W. Lyke, Scott F. Anderson, Éric Armengaud, Julian Bautista, Michael R. Blanton, Michael Blomqvist, Jonathan Brinkmann, Joel R. Brownstein, William Nielsen Brandt, Étienne Burtin, Kyle Dawson, Sylvain de la Torre, Antonis Georgakakis, Héctor Gil-Marín, Paul J. Green, Patrick B. Hall, Jean-Paul Kneib, Stephanie M. LaMassa, Jean-Marc Le Goff, Chelsea MacLeod, Vivek Mariappan, Ian D. McGreer, Andrea

Merloni, Pasquier Noterdaeme, Nathalie Palanque-Delabrouille, Will J. Percival, Ashley J. Ross, Graziano Rossi, Donald P. Schneider, Hee-Jong Seo, Rita Tojeiro, Benjamin A. Weaver, Anne-Marie Weijmans, Christophe Yèche, Pauline Zarrouk, and Gong-Bo Zhao, *The Sloan Digital Sky Survey Quasar Catalog: Fourteenth data release*, A&A613 (2018), A51.

[107] Isabelle Pâris, Patrick Petitjean, Éric Aubourg, Nicholas P. Ross, Adam D. Myers, Alina Streblyanska, Stephen Bailey, Patrick B. Hall, Michael A. Strauss, Scott F. Anderson, Dmitry Bizyaev, Arnaud Borde, J. Brinkmann, Jo Bovy, William N. Brandt, Howard Brewington, Joel R. Brownstein, Benjamin A. Cook, Garrett Ebelke, Xiaohui Fan, Nurten Filiz Ak, Hayley Finley, Andreu Font-Ribera, Jian Ge, Fred Hamann, Shirley Ho, Linhua Jiang, Karen Kinemuchi, Elena Malanushenko, Viktor Malanushenko, Moses Marchante, Ian D. McGreer, Richard G. McMahon, Jordi Miralda-Escudé, Demitri Muna, Pasquier Noterdaeme, Daniel Oravetz, Nathalie Palanque-Delabrouille, Kaike Pan, Ismaël Perez-Fournon, Matthew Pieri, Rogério Riffel, David J. Schlegel, Donald P. Schneider, Audrey Simmons, Matteo Viel, Benjamin A. Weaver, W. Michael Wood-Vasey, Christophe Yèche, and Donald G. York, *The Sloan Digital Sky Survey quasar catalog: tenth data release*, A&A563 (2014), A54.

[108] Isabelle Pâris, Patrick Petitjean, Nicholas P. Ross, Adam D. Myers, Éric Aubourg, Alina Streblyanska, Stephen Bailey, Éric Armengaud, Nathalie Palanque-Delabrouille, Christophe Yèche, Fred Hamann, Michael A. Strauss, Franco D. Albareti, Jo Bovy, Dmitry Bizyaev, W. Niel Brandt, Marcella Brusa, Johannes Buchner, Johan Comparat, Rupert A. C. Croft, Tom Dwelly, Xiaohui Fan, Andreu Font-Ribera, Jian Ge, Antonis Georgakakis, Patrick B. Hall, Linhua Jiang, Karen Kinemuchi, Elena Malanushenko, Viktor Malanushenko, Richard G. McMahon, Marie-Luise Menzel, Andrea Merloni, Kirpal Nandra, Pasquier Noterdaeme, Daniel Oravetz, Kaike Pan, Matthew M. Pieri, Francisco Prada, Mara Salvato, David J. Schlegel, Donald P. Schneider, Audrey Simmons, Matteo Viel, David H. Weinberg, and Liu Zhu, *The Sloan Digital Sky Survey Quasar Catalog: Twelfth data release*, A&A597 (2017), A79.

[109] Daeseong Park, Aaron J. Barth, Jong-Hak Woo, Matthew A. Malkan, Tommaso Treu, Vardha N. Bennert, Roberto J. Assef, and Anna Pancoast, *Extending the Calibration of C IV-based Single-epoch Black Hole Mass Estimators for Active Galactic Nuclei*, ApJ839 (2017), no. 2, 93.

[110] Jeremiah D. Paul, Richard M. Plotkin, Ohad Shemmer, Scott F. Anderson, W. N. Brandt, Xiaohui Fan, Elena Gallo, Bin Luo, Qingling Ni, Gordon T. Richards, Donald P. Schneider, Jianfeng Wu, and Weimin Yi, *Connecting Low- and High-redshift Weak Emission-line Quasars via Hubble Space Telescope Spectroscopy of Lyα Emission*, ApJ929 (2022), no. 1, 78.

[111] Bradley M. Peterson, *Reverberation Mapping of Active Galactic Nuclei*, PASP105 (1993), 247.

[112] ———, *An Introduction to Active Galactic Nuclei*, 1997.

[113] ———, *Toward Precision Measurement of Central Black Hole Masses*, Co-Evolution of Central Black Holes and Galaxies (Bradley M. Peterson, Rachel S. Somerville, and Thaisa Storchi-Bergmann, eds.), vol. 267, May 2010, pp. 151–160.

[114] Bradley M. Peterson and Amri Wandel, *Keplerian Motion of Broad-Line Region Gas as Evidence for Supermassive Black Holes in Active Galactic Nuclei*, ApJ521 (1999), no. 2, L95–L98.

[115] Richard M. Plotkin, Scott F. Anderson, W. N. Brandt, Aleksandar M. Diamond-Stanic, Xiaohui Fan, Patrick B. Hall, Amy E. Kimball, Michael W. Richmond, Donald P. Schneider, Ohad Shemmer, Wolfgang Voges, Donald G. York, Neta A. Bahcall, Stephanie Snedden, Dmitry Bizyaev, Howard Brewington, Viktor Malanushenko, Elena Malanushenko, Dan Oravetz, Kaike Pan, and Audrey Simmons, *Optically Selected BL Lacertae Candidates from the Sloan Digital Sky Survey Data Release Seven*, AJ139 (2010), no. 2, 390–414.

[116] Richard M. Plotkin, Ohad Shemmer, Benny Trakhtenbrot, Scott F. Anderson, W. N. Brandt, Xiaohui Fan, Elena Gallo, Paulina Lira, Bin Luo, Gordon T. Richards, Donald P. Schneider, Michael A. Strauss, and Jianfeng Wu, *Detection of Rest-frame Optical*

Lines from X-shooter Spectroscopy of Weak Emission Line Quasars, ApJ805 (2015), no. 2, 123.

[117] J. Xavier Prochaska, Joseph F. Hennawi, Khee-Gan Lee, Sebastiano Cantalupo, Jo Bovy, S. G. Djorgovski, Sara L. Ellison, Marie Wingyee Lau, Crystal L. Martin, Adam Myers, Kate H. R. Rubin, and Robert A. Simcoe, *Quasars Probing Quasars. VI. Excess H I Absorption within One Proper Mpc of z ∼2 Quasars*, ApJ776 (2013), no. 2, 136.

[118] Suvendu Rakshit, C. S. Stalin, and Jari Kotilainen, *Spectral Properties of Quasars from Sloan Digital Sky Survey Data Release 14: The Catalog*, ApJS249 (2020), no. 1, 17.

[119] Amy L. Rankine, Paul C. Hewett, Manda Banerji, and Gordon T. Richards, *BAL and non-BAL quasars: continuum, emission, and absorption properties establish a common parent sample*, MNRAS492 (2020), no. 3, 4553–4575.

[120] Gordon T. Richards, Nicholas E. Kruczek, S. C. Gallagher, Patrick B. Hall, Paul C. Hewett, Karen M. Leighly, Rajesh P. Deo, Rachael M. Kratzer, and Yue Shen, *Unification of Luminous Type 1 Quasars through C IV Emission*, AJ141 (2011), no. 5, 167.

[121] Gordon T. Richards, Mark Lacy, Lisa J. Storrie-Lombardi, Patrick B. Hall, S. C. Gallagher, Dean C. Hines, Xiaohui Fan, Casey Papovich, Daniel E. Vanden Berk, George B. Trammell, Donald P. Schneider, Marianne Vestergaard, Donald G. York, Sebastian Jester, Scott F. Anderson, Tamás Budavári, and Alexander S. Szalay, *Spectral Energy Distributions and Multiwavelength Selection of Type 1 Quasars*, ApJS166 (2006), no. 2, 470–497.

[122] Gordon T. Richards, Trevor V. McCaffrey, Amy Kimball, Amy L. Rankine, James H. Matthews, Paul C. Hewett, and Angelica B. Rivera, *Probing the Wind Component of Radio Emission in Luminous High-redshift Quasars*, AJ162 (2021), no. 6, 270.

[123] Gordon T. Richards, Adam D. Myers, Alexander G. Gray, Ryan N. Riegel, Robert C. Nichol, Robert J. Brunner, Alexander S. Szalay, Donald P. Schneider, and Scott F. Anderson, *Efficient Photometric Selection of Quasars from the Sloan Digital Sky Survey. II. ∼1,000,000 Quasars from Data Release 6*, ApJS180 (2009), no. 1, 67–83.

[124] Angelica B. Rivera, Gordon T. Richards, Sarah C. Gallagher, Trevor V. McCaffrey, Amy L. Rankine, Paul C. Hewett, and Ohad Shemmer, *Exploring Changes in Quasar Spectral Energy Distributions across C IV Parameter Space*, ApJ931 (2022), no. 2, 154.

[125] Angelica B. Rivera, Gordon T. Richards, Paul C. Hewett, and Amy L. Rankine, *Characterizing Quasar C IV Emission-line Measurements from Time-resolved Spectroscopy*, ApJ899 (2020), no. 2, 96.

[126] Massimo Robberto, Peter W. A. Roming, Alexander J. van der Horst, María. Luisa García-Vargas, Stephen A. Smee, Stephen Goodsell, Jeffrey Radwick, Thomas Hayward, Morten Andersen, Susan Pope, Ethan E. Chaffee, Todd J. Veach, Antonina G. Brody, Kelly D. Smith, Ronnie L. Killough, Kristian B. Persson, Jason L. Stange, Amanda J. Bayless, Rebecca R. Thibodeaux, Andrew L. Peterson, Alexa K. Mathias, Carl L. Schwendeman, Adam W. Thornton, Guy A. Grubbs, Ernesto R. Verastegui, Thomas Lechner, Manuel Maldonado-Medina, Ana Pérez-Calpena, Ernesto Sánchez-Blanco, Gerardo Veredas, Ruben Diaz, Manuel Lazo, Scot Kleinman, Landon Gelman, Robert H. Barkhouser, and Stephen C. Hope, *SCORPIO: Final design and performance estimates for time-domain astronomy*, Society of Photo-Optical Instrumentation Engineers (SPIE) Conference Series, Society of Photo-Optical Instrumentation Engineers (SPIE) Conference Series, vol. 11447, December 2020, p. 1144774.

[127] A. Robinson, *The LAG Spectroscopic Monitoring Campaign: an Overview*, Reverberation Mapping of the Broad-Line Region in Active Galactic Nuclei (P. M. Gondhalekar, K. Horne, and B. M. Peterson, eds.), Astronomical Society of the Pacific Conference Series, vol. 69, January 1994, p. 147.

[128] Jessie C. Runnoe, Michael S. Brotherton, and Zhaohui Shang, *Updating quasar bolometric luminosity corrections*, MNRAS422 (2012), no. 1, 478–493.

[129] M. Schmidt, *3C 273 : A Star-Like Object with Large Red-Shift*, Nature197 (1963), no. 4872, 1040.

[130] Donald P. Schneider, Gordon T. Richards, Patrick B. Hall, Michael A. Strauss, Scott F.

Anderson, Todd A. Boroson, Nicholas P. Ross, Yue Shen, W. N. Brandt, Xiaohui Fan, Naohisa Inada, Sebastian Jester, G. R. Knapp, Coleman M. Krawczyk, Anirudda R. Thakar, Daniel E. Vanden Berk, Wolfgang Voges, Brian Yanny, Donald G. York, Neta A. Bahcall, Dmitry Bizyaev, Michael R. Blanton, Howard Brewington, J. Brinkmann, Daniel Eisenstein, Joshua A. Frieman, Masataka Fukugita, Jim Gray, James E. Gunn, Pascale Hibon, Željko Ivezić, Stephen M. Kent, Richard G. Kron, Myung Gyoon Lee, Robert H. Lupton, Elena Malanushenko, Viktor Malanushenko, Dan Oravetz, K. Pan, Jeffrey R. Pier, III Price, Ted N., David H. Saxe, David J. Schlegel, Audry Simmons, Stephanie A. Snedden, Mark U. SubbaRao, Alexander S. Szalay, and David H. Weinberg, *The Sloan Digital Sky Survey Quasar Catalog. V. Seventh Data Release*, AJ139 (2010), no. 6, 2360.

[131] O. Shemmer, H. Netzer, R. Maiolino, E. Oliva, S. Croom, E. Corbett, and L. di Fabrizio, *Near-Infrared Spectroscopy of High-Redshift Active Galactic Nuclei. I. A Metallicity-Accretion Rate Relationship*, ApJ614 (2004), no. 2, 547–557.

[132] Ohad Shemmer, W. N. Brandt, Scott F. Anderson, Aleksandar M. Diamond-Stanic, Xiaohui Fan, Gordon T. Richards, Donald P. Schneider, and Michael A. Strauss, *X-Ray Insights into the Nature of Weak Emission-Line Quasars at High Redshift*, ApJ696 (2009), no. 1, 580–590.

[133] Ohad Shemmer, W. N. Brandt, Hagai Netzer, Roberto Maiolino, and Shai Kaspi, *The Hard X-Ray Spectrum as a Probe for Black Hole Growth in Radio-Quiet Active Galactic Nuclei*, ApJ682 (2008), no. 1, 81–93.

[134] Ohad Shemmer, W. N. Brandt, Donald P. Schneider, Xiaohui Fan, Michael A. Strauss, Aleksandar M. Diamond-Stanic, Gordon T. Richards, Scott F. Anderson, James E. Gunn, and Jon Brinkmann, *Chandra Observations of the Highest Redshift Quasars from the Sloan Digital Sky Survey*, ApJ644 (2006), no. 1, 86–99.

[135] Ohad Shemmer and Sara Lieber, *Weak Emission-line Quasars in the Context of a Modified Baldwin Effect*, ApJ805 (2015), no. 2, 124.

[136] Ohad Shemmer, Benny Trakhtenbrot, Scott F. Anderson, W. N. Brandt, Aleksan-

dar M. Diamond-Stanic, Xiaohui Fan, Paulina Lira, Hagai Netzer, Richard M. Plotkin, Gordon T. Richards, Donald P. Schneider, and Michael A. Strauss, *Weak Line Quasars at High Redshift: Extremely High Accretion Rates or Anemic Broad-line Regions?*, ApJ722 (2010), no. 2, L152–L156.

[137] Yue Shen, *The mass of quasars*, Bulletin of the Astronomical Society of India 41 (2013), no. 1, 61–115.

[138] ———, *Rest-frame Optical Properties of Luminous 1.5 < Z < 3.5 Quasars: The Hβ-[O III] Region*, ApJ817 (2016), no. 1, 55.

[139] Yue Shen, W. N. Brandt, Kyle S. Dawson, Patrick B. Hall, Ian D. McGreer, Scott F. Anderson, Yuguang Chen, Kelly D. Denney, Sarah Eftekharzadeh, Xiaohui Fan, Yang Gao, Paul J. Green, Jenny E. Greene, Luis C. Ho, Keith Horne, Linhua Jiang, Brandon C. Kelly, Karen Kinemuchi, Christopher S. Kochanek, Isabelle Pâris, Christina M. Peters, Bradley M. Peterson, Patrick Petitjean, Kara Ponder, Gordon T. Richards, Donald P. Schneider, Anil Seth, Robyn N. Smith, Michael A. Strauss, Charling Tao, Jonathan R. Trump, W. M. Wood-Vasey, Ying Zu, Daniel J. Eisenstein, Kaike Pan, Dmitry Bizyaev, Viktor Malanushenko, Elena Malanushenko, and Daniel Oravetz, *The Sloan Digital Sky Survey Reverberation Mapping Project: Technical Overview*, ApJS216 (2015), no. 1, 4.

[140] Yue Shen, W. N. Brandt, Gordon T. Richards, Kelly D. Denney, Jenny E. Greene, C. J. Grier, Luis C. Ho, Bradley M. Peterson, Patrick Petitjean, Donald P. Schneider, Charling Tao, and Jonathan R. Trump, *The Sloan Digital Sky Survey Reverberation Mapping Project: Velocity Shifts of Quasar Emission Lines*, ApJ831 (2016), no. 1, 7.

[141] Yue Shen, Jenny E. Greene, Michael A. Strauss, Gordon T. Richards, and Donald P. Schneider, *Biases in Virial Black Hole Masses: An SDSS Perspective*, ApJ680 (2008), no. 1, 169–190.

[142] Yue Shen and Luis C. Ho, *The diversity of quasars unified by accretion and orientation*, Nature513 (2014), no. 7517, 210–213.

[143] Yue Shen and Brandon C. Kelly, *The Demographics of Broad-line Quasars in the Mass-*

Luminosity Plane. I. Testing FWHM-based Virial Black Hole Masses, ApJ746 (2012), no. 2, 169.

[144] Yue Shen, Gordon T. Richards, Michael A. Strauss, Patrick B. Hall, Donald P. Schneider, Stephanie Snedden, Dmitry Bizyaev, Howard Brewington, Viktor Malanushenko, Elena Malanushenko, Dan Oravetz, Kaike Pan, and Audrey Simmons, *A Catalog of Quasar Properties from Sloan Digital Sky Survey Data Release 7*, ApJS194 (2011), no. 2, 45.

[145] Yue Shen, Michael A. Strauss, Masamune Oguri, Joseph F. Hennawi, Xiaohui Fan, Gordon T. Richards, Patrick B. Hall, James E. Gunn, Donald P. Schneider, Alexander S. Szalay, Anirudda R. Thakar, Daniel E. Vanden Berk, Scott F. Anderson, Neta A. Bahcall, Andrew J. Connolly, and Gillian R. Knapp, *Clustering of High-Redshift ($z >= 2.9$) Quasars from the Sloan Digital Sky Survey*, AJ133 (2007), no. 5, 2222–2241.

[146] Yue Shen, Jin Wu, Linhua Jiang, Eduardo Bañados, Xiaohui Fan, Luis C. Ho, Dominik A. Riechers, Michael A. Strauss, Bram Venemans, Marianne Vestergaard, Fabian Walter, Feige Wang, Chris Willott, Xue-Bing Wu, and Jinyi Yang, *Gemini GNIRS Near-infrared Spectroscopy of 50 Quasars at $z \gtrsim 5.7$*, ApJ873 (2019), no. 1, 35.

[147] M. F. Skrutskie, R. M. Cutri, R. Stiening, M. D. Weinberg, S. Schneider, J. M. Carpenter, C. Beichman, R. Capps, T. Chester, J. Elias, J. Huchra, J. Liebert, C. Lonsdale, D. G. Monet, S. Price, P. Seitzer, T. Jarrett, J. D. Kirkpatrick, J. E. Gizis, E. Howard, T. Evans, J. Fowler, L. Fullmer, R. Hurt, R. Light, E. L. Kopan, K. A. Marsh, H. L. McCallon, R. Tam, S. Van Dyk, and S. Wheelock, *The Two Micron All Sky Survey (2MASS)*, AJ131 (2006), no. 2, 1163–1183.

[148] D. N. Spergel, R. Bean, O. Doré, M. R. Nolta, C. L. Bennett, J. Dunkley, G. Hinshaw, N. Jarosik, E. Komatsu, L. Page, H. V. Peiris, L. Verde, M. Halpern, R. S. Hill, A. Kogut, M. Limon, S. S. Meyer, N. Odegard, G. S. Tucker, J. L. Weiland, E. Wollack, and E. L. Wright, *Three-Year Wilkinson Microwave Anisotropy Probe (WMAP) Observations: Implications for Cosmology*, ApJS170 (2007), no. 2, 377–408.

[149] Hyewon Suh, Francesca Civano, Benny Trakhtenbrot, Francesco Shankar, Günther

Hasinger, David B. Sanders, and Viola Allevato, *No Significant Evolution of Relations between Black Hole Mass and Galaxy Total Stellar Mass Up to $z \sim 2.5$*, ApJ889 (2020), no. 1, 32.

[150] Jack W. Sulentic, Rumen Bachev, Paola Marziani, C. Alenka Negrete, and Deborah Dultzin, *C IV λ1549 as an Eigenvector 1 Parameter for Active Galactic Nuclei*, ApJ666 (2007), no. 2, 757–777.

[151] Naoyuki Tamura, Naruhisa Takato, Atsushi Shimono, Yuki Moritani, Kiyoto Yabe, Yuki Ishizuka, Akitoshi Ueda, Yukiko Kamata, Hrand Aghazarian, Stéphane Arnouts, Gabriel Barban, Robert H. Barkhouser, Renato C. Borges, David F. Braun, Michael A. Carr, Pierre-Yves Chabaud, Yin-Chang Chang, Hsin-Yo Chen, Masashi Chiba, Richard C. Y. Chou, You-Hua Chu, Judith Cohen, Rodrigo P. de Almeida, Antonio C. de Oliveira, Ligia S. de Oliveira, Richard G. Dekany, Kjetil Dohlen, Jesulino B. dos Santos, Leandro H. dos Santos, Richard Ellis, Maximilian Fabricius, Didier Ferrand, Décio Ferreira, Mirek Golebiowski, Jenny E. Greene, Johannes Gross, James E. Gunn, Randolph Hammond, Albert Harding, Murdock Hart, Timothy M. Heckman, Christopher M. Hirata, Paul Ho, Stephen C. Hope, Larry Hovland, Shu-Fu Hsu, Yen-Shan Hu, Ping-Jie Huang, Marc Jaquet, Yipeng Jing, Jennifer Karr, Masahiko Kimura, Matthew E. King, Eiichiro Komatsu, Vincent Le Brun, Olivier Le Fèvre, Arnaud Le Fur, David Le Mignant, Hung-Hsu Ling, Craig P. Loomis, Robert H. Lupton, Fabrice Madec, Peter Mao, Lucas S. Marrara, Claudia Mendes de Oliveira, Yosuke Minowa, Chaz Morantz, Hitoshi Murayama, Graham J. Murray, Youichi Ohyama, Joseph Orndorff, Sandrine Pascal, Jefferson M. Pereira, Daniel Reiley, Martin Reinecke, Andreas Ritter, Mitsuko Roberts, Mark A. Schwochert, Michael D. Seiffert, Stephen A. Smee, Laerte Sodre, David N. Spergel, Aaron J. Steinkraus, Michael A. Strauss, Christian Surace, Yasushi Suto, Nao Suzuki, John Swinbank, Philip J. Tait, Masahiro Takada, Tomonori Tamura, Yoko Tanaka, Laurence Tresse, Orlando Verducci, Didier Vibert, Clement Vidal, Shiang-Yu Wang, Chih-Yi Wen, Chi-Hung Yan, and Naoki Yasuda, *Prime Focus Spectrograph (PFS) for*

the Subaru telescope: overview, recent progress, and future perspectives, Ground-based and Airborne Instrumentation for Astronomy VI (Christopher J. Evans, Luc Simard, and Hideki Takami, eds.), Society of Photo-Optical Instrumentation Engineers (SPIE) Conference Series, vol. 9908, August 2016, p. 99081M.

[152] John D. Timlin, W. N. Brandt, Q. Ni, B. Luo, Xingting Pu, D. P. Schneider, M. Vivek, and W. Yi, *The correlations between optical/UV broad lines and X-ray emission for a large sample of quasars*, MNRAS492 (2020), no. 1, 719–741.

[153] Benny Trakhtenbrot and Hagai Netzer, *Black hole growth to z = 2 - I. Improved virial methods for measuring M_{BH} and L/L_{Edd}*, MNRAS427 (2012), no. 4, 3081–3102.

[154] David Tytler and Xiao-Ming Fan, *Systematic QSO Emission-Line Velocity Shifts and New Unbiased Redshifts*, ApJS79 (1992), 1.

[155] Vivian U, Aaron J. Barth, H. Alexander Vogler, Hengxiao Guo, Tommaso Treu, Vardha N. Bennert, Gabriela Canalizo, Alexei V. Filippenko, Elinor Gates, Frederick Hamann, Michael D. Joner, Matthew A. Malkan, Anna Pancoast, Peter R. Williams, Jong-Hak Woo, Bela Abolfathi, L. E. Abramson, Stephen F. Armen, Hyun-Jin Bae, Thomas Bohn, Benjamin D. Boizelle, Azalee Bostroem, Andrew Brandel, Thomas G. Brink, Sanyum Channa, M. C. Cooper, Maren Cosens, Edward Donohue, Sean P. Fillingham, Diego González-Buitrago, Goni Halevi, Andrew Halle, Carol E. Hood, Keith Horne, J. Chuck Horst, Maxime de Kouchkovsky, Benjamin Kuhn, Sahana Kumar, Douglas C. Leonard, Donald Loveland, Christina Manzano-King, Ian McHardy, Raúl Michel, Melanie Kae B. Olaes, Daeseong Park, Songyoun Park, Liuyi Pei, Timothy W. Ross, Jordan N. Runco, Jenna Samuel, Javier Sánchez, Bryan Scott, Remington O. Sexton, Jaejin Shin, Isaac Shivvers, Chance L. Spencer, Benjamin E. Stahl, Samantha Stegman, Isak Stomberg, Stefano Valenti, L. Villafaña, Jonelle L. Walsh, Heechan Yuk, and WeiKang Zheng, *The Lick AGN Monitoring Project 2016: Velocity-resolved Hβ Lags in Luminous Seyfert Galaxies*, ApJ925 (2022), no. 1, 52.

[156] Daniel E. Vanden Berk, Gordon T. Richards, Amanda Bauer, Michael A. Strauss, Donald P. Schneider, Timothy M. Heckman, Donald G. York, Patrick B. Hall, Xiaohui Fan,

G. R. Knapp, Scott F. Anderson, James Annis, Neta A. Bahcall, Mariangela Bernardi, John W. Briggs, J. Brinkmann, Robert Brunner, Scott Burles, Larry Carey, Francisco J. Castander, A. J. Connolly, J. H. Crocker, István Csabai, Mamoru Doi, Douglas Finkbeiner, Scott Friedman, Joshua A. Frieman, Masataka Fukugita, James E. Gunn, G. S. Hennessy, Željko Ivezić, Stephen Kent, Peter Z. Kunszt, D. Q. Lamb, R. French Leger, Daniel C. Long, Jon Loveday, Robert H. Lupton, Avery Meiksin, Aronne Merelli, Jeffrey A. Munn, Heidi Jo Newberg, Matt Newcomb, R. C. Nichol, Russell Owen, Jeffrey R. Pier, Adrian Pope, Constance M. Rockosi, David J. Schlegel, Walter A. Siegmund, Stephen Smee, Yehuda Snir, Chris Stoughton, Christopher Stubbs, Mark SubbaRao, Alexander S. Szalay, Gyula P. Szokoly, Christy Tremonti, Alan Uomoto, Patrick Waddell, Brian Yanny, and Wei Zheng, *Composite Quasar Spectra from the Sloan Digital Sky Survey*, AJ122 (2001), no. 2, 549–564.

[157] M. Vestergaard, K. Denney, X. Fan, J. J. Jensen, B. C. Kelly, P. S. Osmer, B. M. Peterson, and C. A. Tremonti, *Black hole mass estimations: limitations and uncertainties*, Narrow-Line Seyfert 1 Galaxies and their Place in the Universe (L. Foschini, M. Colpi, L. Gallo, D. Grupe, S. Komossa, K. Leighly, and S. Mathur, eds.), January 2011, p. 38.

[158] M. Vestergaard and Patrick S. Osmer, *Mass Functions of the Active Black Holes in Distant Quasars from the Large Bright Quasar Survey, the Bright Quasar Survey, and the Color-selected Sample of the SDSS Fall Equatorial Stripe*, ApJ699 (2009), no. 1, 800–816.

[159] M. Vestergaard and B. J. Wilkes, *An Empirical Ultraviolet Template for Iron Emission in Quasars as Derived from I Zwicky 1*, ApJS134 (2001), no. 1, 1–33.

[160] Marianne Vestergaard and Bradley M. Peterson, *Determining Central Black Hole Masses in Distant Active Galaxies and Quasars. II. Improved Optical and UV Scaling Relationships*, ApJ641 (2006), no. 2, 689–709.

[161] G. Vietri, E. Piconcelli, M. Bischetti, F. Duras, S. Martocchia, A. Bongiorno, A. Marconi, L. Zappacosta, S. Bisogni, G. Bruni, M. Brusa, A. Comastri, G. Cresci, C. Feruglio, E. Giallongo, F. La Franca, V. Mainieri, F. Mannucci, F. Ricci, E. Sani, V. Testa, F. Tombesi, C. Vignali, and F. Fiore, *The WISSH quasars project. IV. Broad line region*

versus kiloparsec-scale winds, A&A617 (2018), A81.

[162] A. Wandel, B. M. Peterson, and M. A. Malkan, *Central Masses and Broad-Line Region Sizes of Active Galactic Nuclei. I. Comparing the Photoionization and Reverberation Techniques*, ApJ526 (1999), no. 2, 579–591.

[163] Yongjiang Wang, Wanqing Liu, Zhaohui Shang, and Michael S. Brotherton, *Comparison of the active galactic nuclei Baldwin effect with the modified Baldwin effect of the ultraviolet-optical emission lines in a single sample*, MNRAS515 (2022), no. 4, 5836–5846.

[164] Jong-Hak Woo, Huynh Anh N. Le, Marios Karouzos, Dawoo Park, Daeseong Park, Matthew A. Malkan, Tommaso Treu, and Vardha N. Bennert, *Calibration and Limitations of the Mg II Line-based Black Hole Masses*, ApJ859 (2018), no. 2, 138.

[165] Jong-Hak Woo, Yosep Yoon, Songyoun Park, Daeseong Park, and Sang Chul Kim, *The Black Hole Mass-Stellar Velocity Dispersion Relation of Narrow-line Seyfert 1 Galaxies*, ApJ801 (2015), no. 1, 38.

[166] Edward L. Wright, Peter R. M. Eisenhardt, Amy K. Mainzer, Michael E. Ressler, Roc M. Cutri, Thomas Jarrett, J. Davy Kirkpatrick, Deborah Padgett, Robert S. McMillan, Michael Skrutskie, S. A. Stanford, Martin Cohen, Russell G. Walker, John C. Mather, David Leisawitz, III Gautier, Thomas N., Ian McLean, Dominic Benford, Carol J. Lonsdale, Andrew Blain, Bryan Mendez, William R. Irace, Valerie Duval, Fengchuan Liu, Don Royer, Ingolf Heinrichsen, Joan Howard, Mark Shannon, Martha Kendall, Amy L. Walsh, Mark Larsen, Joel G. Cardon, Scott Schick, Mark Schwalm, Mohamed Abid, Beth Fabinsky, Larry Naes, and Chao-Wei Tsai, *The Wide-field Infrared Survey Explorer (WISE): Mission Description and Initial On-orbit Performance*, AJ140 (2010), no. 6, 1868–1881.

[167] Jianfeng Wu, W. N. Brandt, Scott F. Anderson, Aleksandar M. Diamond-Stanic, Patrick B. Hall, Richard M. Plotkin, Donald P. Schneider, and Ohad Shemmer, *X-Ray and Multiwavelength Insights into the Nature of Weak Emission-line Quasars at Low Redshift*, ApJ747 (2012), no. 1, 10.

[168] Jianfeng Wu, W. N. Brandt, Patrick B. Hall, Robert R. Gibson, Gordon T. Richards,

Donald P. Schneider, Ohad Shemmer, Dennis W. Just, and Sarah J. Schmidt, *A Population of X-Ray Weak Quasars: PHL 1811 Analogs at High Redshift*, ApJ736 (2011), no. 1, 28.

[169] Donald G. York, J. Adelman, Jr. Anderson, John E., Scott F. Anderson, James Annis, Neta A. Bahcall, J. A. Bakken, Robert Barkhouser, Steven Bastian, Eileen Berman, William N. Boroski, Steve Bracker, Charlie Briegel, John W. Briggs, J. Brinkmann, Robert Brunner, Scott Burles, Larry Carey, Michael A. Carr, Francisco J. Castander, Bing Chen, Patrick L. Colestock, A. J. Connolly, J. H. Crocker, István Csabai, Paul C. Czarapata, John Eric Davis, Mamoru Doi, Tom Dombeck, Daniel Eisenstein, Nancy Ellman, Brian R. Elms, Michael L. Evans, Xiaohui Fan, Glenn R. Federwitz, Larry Fiscelli, Scott Friedman, Joshua A. Frieman, Masataka Fukugita, Bruce Gillespie, James E. Gunn, Vijay K. Gurbani, Ernst de Haas, Merle Haldeman, Frederick H. Harris, J. Hayes, Timothy M. Heckman, G. S. Hennessy, Robert B. Hindsley, Scott Holm, Donald J. Holmgren, Chi-hao Huang, Charles Hull, Don Husby, Shin-Ichi Ichikawa, Takashi Ichikawa, Željko Ivezić, Stephen Kent, Rita S. J. Kim, E. Kinney, Mark Klaene, A. N. Kleinman, S. Kleinman, G. R. Knapp, John Korienek, Richard G. Kron, Peter Z. Kunszt, D. Q. Lamb, B. Lee, R. French Leger, Siriluk Limmongkol, Carl Lindenmeyer, Daniel C. Long, Craig Loomis, Jon Loveday, Rich Lucinio, Robert H. Lupton, Bryan MacKinnon, Edward J. Mannery, P. M. Mantsch, Bruce Margon, Peregrine McGehee, Timothy A. McKay, Avery Meiksin, Aronne Merelli, David G. Monet, Jeffrey A. Munn, Vijay K. Narayanan, Thomas Nash, Eric Neilsen, Rich Neswold, Heidi Jo Newberg, R. C. Nichol, Tom Nicinski, Mario Nonino, Norio Okada, Sadanori Okamura, Jeremiah P. Ostriker, Russell Owen, A. George Pauls, John Peoples, R. L. Peterson, Donald Petravick, Jeffrey R. Pier, Adrian Pope, Ruth Pordes, Angela Prosapio, Ron Rechenmacher, Thomas R. Quinn, Gordon T. Richards, Michael W. Richmond, Claudio H. Rivetta, Constance M. Rockosi, Kurt Ruthmansdorfer, Dale Sandford, David J. Schlegel, Donald P. Schneider, Maki Sekiguchi, Gary Sergey, Kazuhiro Shimasaku, Walter A. Siegmund, Stephen Smee, J. Allyn Smith,

S. Snedden, R. Stone, Chris Stoughton, Michael A. Strauss, Christopher Stubbs, Mark SubbaRao, Alexander S. Szalay, Istvan Szapudi, Gyula P. Szokoly, Anirudda R. Thakar, Christy Tremonti, Douglas L. Tucker, Alan Uomoto, Dan Vanden Berk, Michael S. Vogeley, Patrick Waddell, Shu-i. Wang, Masaru Watanabe, David H. Weinberg, Brian Yanny, Naoki Yasuda, and SDSS Collaboration, *The Sloan Digital Sky Survey: Technical Summary*, AJ120 (2000), no. 3, 1579–1587.

[170] Li-Ming Yu, Wei-Hao Bian, Chan Wang, Bi-Xuan Zhao, and Xue Ge, *Calibration of the virial factor f in supermassive black hole masses of reverberation-mapped AGNs*, MNRAS488 (2019), no. 2, 1519–1534.

[171] Li-Ming Yu, Wei-Hao Bian, Xue-Guang Zhang, Bi-Xuan Zhao, Chan Wang, Xue Ge, Bing-Qian Zhu, and Yu-Qin Chen, *The Supermassive Black Hole Masses of Reverberation-mapped Active Galactic Nuclei*, ApJ901 (2020), no. 2, 133.

[172] Li-Ming Yu, Bi-Xuan Zhao, Wei-Hao Bian, Chan Wang, and Xue Ge, *An extended size-luminosity relation for the reverberation-mapped AGNs: the role of the accretion rate*, MNRAS491 (2020), no. 4, 5881–5896.

[173] Gong-Bo Zhao, Yuting Wang, Shun Saito, Héctor Gil-Marín, Will J. Percival, Dandan Wang, Chia-Hsun Chuang, Rossana Ruggeri, Eva-Maria Mueller, Fangzhou Zhu, Ashley J. Ross, Rita Tojeiro, Isabelle Pâris, Adam D. Myers, Jeremy L. Tinker, Jian Li, Etienne Burtin, Pauline Zarrouk, Florian Beutler, Falk Baumgarten, Julian E. Bautista, Joel R. Brownstein, Kyle S. Dawson, Jiamin Hou, Axel de la Macorra, Graziano Rossi, John A. Peacock, Ariel G. Sánchez, Arman Shafieloo, Donald P. Schneider, and Cheng Zhao, *The clustering of the SDSS-IV extended Baryon Oscillation Spectroscopic Survey DR14 quasar sample: a tomographic measurement of cosmic structure growth and expansion rate based on optimal redshift weights*, MNRAS482 (2019), no. 3, 3497–3513.

[174] Wenwen Zuo, Xue-Bing Wu, Xiaohui Fan, Richard Green, Ran Wang, and Fuyan Bian, *Black Hole Mass Estimates and Rapid Growth of Supermassive Black Holes in Luminous z ∼3.5 Quasars*, ApJ799 (2015), no. 2, 189.